The impact of heterogeneity on geothermal production: simulation benchmarks and applications

Wang, Y.

DOI
10.4233/uuid:a5bdb2ef-c02c-45e9-bb92-07961d3ef28b

Publication date
2021

Document Version
Final published version

Citation (APA)
Wang, Y. (2021). *The impact of heterogeneity on geothermal production: simulation benchmarks and applications*. [Dissertation (TU Delft), Delft University of Technology]. https://doi.org/10.4233/uuid:a5bdb2ef-c02c-45e9-bb92-07961d3ef28b

THE IMPACT OF HETEROGENEITY ON GEOTHERMAL PRODUCTION: SIMULATION BENCHMARKS AND APPLICATIONS

THE IMPACT OF HETEROGENEITY ON GEOTHERMAL PRODUCTION: SIMULATION BENCHMARKS AND APPLICATIONS

Dissertation

for the purpose of obtaining the degree of doctor
at Delft University of Technology,
by the authority of the Rector Magnificus Prof.dr.ir. T.H.J.J. van der Hagen,
chair of the Board for Doctorates,
to be defended publicly on
Tuesday 23 February 2021 at 15:00 o'clock

by

Yang WANG

Master in Petroleum Engineering,
China University of Petroleum, Beijing, China,
born in Shandong, China.

This dissertation has been approved by the promotors.

Composition of the doctoral committee:

Rector Magnificus	Chairman
Dr. D. V. Voskov	Delft University of Technology, promotor
Prof. dr. D. F. Bruhn	Delft University of Technology, promotor
Independent members:	
Prof. dr. ir. P. L. J. Zitha	Delft University of Technology
Prof. dr. I. Berre	University of Bergen, Norway
Dr. M. Brehme	Delft University of Technology
Dr. P. J. Vardon	Delft University of Technology
Dr. J. P. O'Sullivan	University of Auckland, New Zealand
Reserve member:	
Prof. dr. W. R. Rossen	Delft University of Technology

Keywords: heterogeneous reservoir, geothermal benchmark, sensitivity analysis, uncertainty quantification, fractured reservoir

Printed by: Gildeprint

Cover design: Yang Wang

ISBN 978-94-6384-197-9

Science is a wonderful thing
if one does not have to earn one's living at it.

Albert Einstein

to my parents

CONTENTS

SUMMARY

Numerical simulation plays an important role for the efficient development of geothermal resources, considering all the uncertain and sensitive parameters that exist within the subsurface and during the operations. This thesis describes the numerical modeling of geothermal developments of various types and in various situations using the newly developed open-source numerical simulator, called Delft Advanced Research Terra Simulator, shortly DARTS. The main objective of this thesis is to investigate the influence of heterogeneity to geothermal developments.

The generic geothermal capability is first constructed in the existing DARTS framework. Chapter 2 describes the geothermal module (including formulations) implemented within DARTS, which consists of an efficient computational core programmed in C++ and a flexible custom interface designed in Python. The main architecture of DARTS facilitates both model constructions and linking external (open-source) packages. After the implementation of a new simulation code, the primary task before performing numerical modelling is to validate it, for main aspects of accuracy and efficiency. In Chapter 3, the geothermal module of DARTS has been benchmarked with state-of-the-art numerical simulators specialized in geothermal simulations, through systematic comparisons under both low- and high-enthalpy conditions. DARTS achieves more efficient simulations owing to the Operator-Based Linearization (OBL) approach, which linearizes the physical domain in operator forms and performs interpolations along simulations. After validation, DARTS has been shown to be trustworthy for simulating geothermal applications.

Heat conduction, as one of the key mechanisms in heat transfer, determines the importance of impermeable shale facies to geothermal development. However, introducing shale facies into the numerical model increases the computing workload with no doubt. If the small cells of shale facies can be upscaled while the results keep accurate, significant computing time will be saved. In Chapter 4, local and flow-based upscaling methods are examined to agglomerate the shale cells to a coarser level. The results show that these two approaches are not generally suitable to upscale shale facies in geothermal applications because of the mixed conduction-convection behavior of heat transport. Therefore, until an better method is developed, keeping the representation of shale facies at fine-resolution will be our default strategy.

In Chapter 5, a high-resolution geological model at the geological scale is utilized to investigate the influence of potential sensitivity parameters on the geothermal development. Based on seismic measurements and log curves, the real static geological parameters are interpreted with detailed characterizations. Several parameters sensitive to the development of the real field are studied. One key finding is that a pronounced delay of thermal breakthrough is observed when modeling with the shale facies compared to excluding them, which proves the importance of thermal conductive recharge of shale to heat propagation. The heat production also displays large sensitivity to reservoir het-

erogeneity, as the thermal breakthrough time varies a lot with even minor shifts in well placement. Simulating with the real geological model, instead of conceptual or synthetic models, provides convincing results for the geothermal development in reality.

In Chapter 6, a systematic uncertainty quantification is performed within the same geological model considering the geological, physical, operational and economic uncertainties. The uncertain parameters are either randomly generated from a base-case realization (e.g., the spatial distribution of permeability and porosity) or follow the normal distribution around their typical mean values (e.g., the salinity of groundwater, heat price, etc.). The conventional Monte Carlo method is utilized to sample the uncertain parameters. Large uncertainties of the output parameters, mainly energy production and Net Present Value, are identified. The full set of uncertainty quantification is performed on a GPU version of DARTS. The high-performance of DARTS on GPU enables large ensembles of forward simulations to be conducted in affordable time.

High-enthalpy geothermal resources, presenting a large energy potential, can be associated with complex reservoir geometry, like fractured sediments. In Chapter 7, the multiphase flow and dynamics of heat transport in fractured high-enthalpy geothermal reservoirs are investigated. A synthetic fracture network is firstly generated to study the convergence of numerical results under different resolutions of mesh discretization. The optimal mesh discretization is selected under comprehensive consideration of computing accuracy and efficiency. A thermal Peclet number is then defined to characterize the dynamic heat transfer processes, which are divided into different regimes of the Peclet curve. Afterwards, a fracture network generated from measurement of a real outcrop is utilized to study the variations in heat production with the change of several parameters under optimized grid discretization. This chapter provides a general framework for studying the dynamics of mass and heat transfer in fractured geothermal reservoirs.

Chapter 8 discusses a numerical phenomenon causing convergence issues called ‘negative compressibility’. It is usually relevant to the tightly coupled solutions of mass and energy conservation equations in multiphase flow. Constructed within the OBL framework, a nonlinear strategy is proposed to solve the problem at different levels of physical resolutions sequentially. The nonlinear convergence of high-enthalpy geothermal simulation is improved with this approach in several studied situations.

NOMENCLATURE

Physical Symbols

M	accumulation term for mass and energy
F	flux term for mass and energy
q	source/sink term for mass and energy
ρ_p	phase density
n_p	number of fluid phases
n_c	number of components
x_p^k	molar fraction of component k in phase p
s_p	phase saturation
U_p	phase internal energy
U_r	rock internal energy
ϕ	effective rock porosity
ϕ_0	initial rock porosity
c_r	rock compressibility
p_{ref}	reference pressure
$\boldsymbol{u_p}$	phase velocity
$\mathbf{K}$	full permeability tensor
k_{rp}	phase relative permeability
μ_p	phase viscosity
p_p	phase pressure
$\boldsymbol{\gamma}_p$	phase specific weight
D	depth
h_p	phase enthalpy
T	temperature
κ	effective thermal conductivity
κ_p	phase thermal conductivity
κ_r	rock thermal conductivity
ρ_t	total fluid density

ρ_s	brine density
S	salinity
μ_s	brine viscosity

Linearization Operators

$\alpha(\omega)$	mass accumulation operator
$\beta(\omega)$	mass flux operator
$\alpha_{ef}(\omega)$	phase energy accumulation operator
$\alpha_{er}(\omega)$	rock energy accumulation operator
$\beta_e(\omega)$	energy flux operator
γ_{ef}	phase thermal conduction operator
$\zeta_p^{vol}(\omega)$	volumetric well rate operator
$\zeta_p^{vol}(\omega)$	mass well rate operator
$\delta_p(\omega)$	phase density operator

Other Symbols

Γ^l	fluid transmissibility
Γ_T	rock thermal transmissibility
$\Phi_{p,ij}$	potential difference of phase p between block i and j
P_{pump}	pump energy
P_{prod}	produced energy
P_{inj}	injected energy
η	pump efficiency
C_{well}	drilling cost
r	yearly discount rate
r_w	wellbore radius
r_o	equivalent radius of a well block

1

INTRODUCTION

In the context of global warming, great efforts are made to control greenhouse gas (GHG) emissions. One source for a large amount of GHG emissions is the burning of fossil fuels for the generation of heat and power. Geothermal energy, long overlooked in many parts of the world, has started to attract increased attention [1, 2]. Besides a low carbon footprint, compared with other renewable energy (e.g., wind energy, solar energy), geothermal energy provides stable energy supply. It is hardly impacted by the weather and seasonal changes. Therefore, geothermal energy is considered a promising alternative for fossil fuels. The worldwide distribution and astonishing reserves [3–8] make it potentially competitive. This high theoretical potential is illustrated in Fig. 1.1, which displays the global temperature gradient distribution calculated based on heat flow. Higher temperature gradients, in general, indicate higher geothermal potential and easily become the focus of attention.

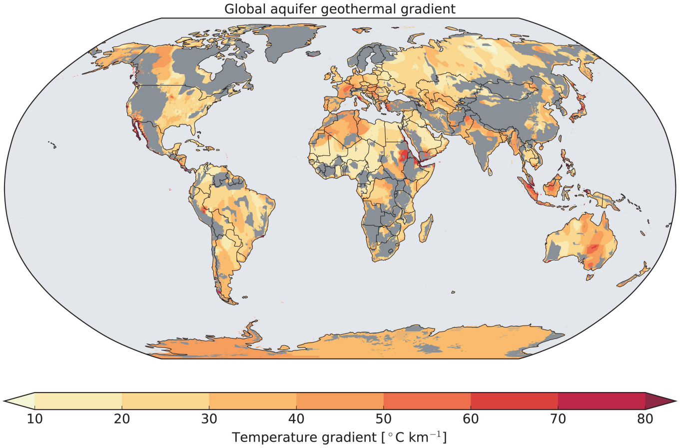

Figure 1.1: Geothermal gradients in aquifers around the world [7].

The development of geothermal energy can also take advantage of depleted oil-gas fields [9–11] to reduce early-stage investment or synergy potential with oil exploitation [12] to maximize the Net Present Value (NPV). Generally, its flexibility makes geothermal heat an attractive resource. For low-enthalpy reservoirs, the produced hot fluids can be used for direct heating (e.g., popular uses in the horticulture of the Netherlands), while the high-enthalpy resources can be converted to electricity, which is convenient for storage and transport with the existing technology. Fig. 1.2 displays the installed capacity for geothermal electricity around the world by the year 2019.

Among geothermal resources [7, 13], high-enthalpy geothermal fields [14] have received special attention owing to their substantial energy potential [15, 16]. For a high-enthalpy geothermal system, either single-phase (vapor) or a two-phase mixture (vapor and liquid) can be present at the reservoir conditions. The Geysers field [17], an epitome of high-enthalpy geothermal systems, is currently the world's largest exploited geothermal complex. It produces hot steam from more than 350 wells to generate electricity in 22 power plants. The installed capacity reaches 1517 MW and the active producing capacity was 900 MW by the year 2020, which demonstrates the high potential of geother-

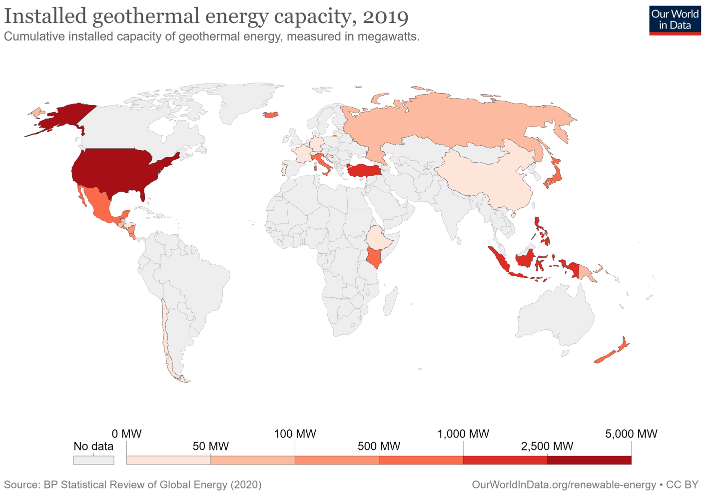

Figure 1.2: Installed geothermal energy capacity.

mal resources, considering the more than 50 years of continuous power generation at The Geysers.

However, the development and usage of geothermal energy is still in the preliminary stage in most places of the world. In order to achieve efficient development of the geothermal resources, understanding the governing mechanisms for heat and mass transport plays an essential role. The heat propagation and thermal breakthrough can be very different for different geothermal fields. In the subsurface, convective and diffusive (or conductive) flow are common and can greatly influence the mass and heat transport processes. In general, the development of a geothermal reservoir requires circulating fluid to extract heat from underground, which involves non-isothermal processes because of heat exchange. The synergy of thermal convection and conduction plays a critical role in the development of geothermal reservoirs, where the heat is extracted with continuous production and circulation of the heat carrier (e.g., water or CO_2 [18]) in manifold ways (e.g., well doublet [19], borehole heat exchanger [20], etc.). Following the cold water injection, thermal convection and conduction jointly govern the heat propagation in geothermal reservoirs.

In addition to the mechanisms controlling heat transfer, a lot of uncertainties can impact the heat transport and production, including factors both residing inside the reservoir, like heterogeneity and geological structures, and in the layout and design of operations [21], like doublet placement [22]. The concerning parameters (e.g., generated energy and NPV) can vary to a large extent because of these uncertainties. Systematic sensitivity analysis and uncertainty quantification of these uncertain factors are necessary and helpful. They allow a more accurate prediction of heat production, which helps to better constrain project economics and benefit operators by adjusting the development scheme in time.

The development of geothermal systems can be assisted by inherent or induced fracture networks, especially for reservoirs with a low permeable matrix. Most high-enthalpy geothermal systems either contain naturally developed fractures or require induced fractures for fluid flow. Due to the high conductivity of open fractures, they behave as preferential flow channels for the injected cold water. In comparison with a reservoir geometry exploiting primary porosity, the complex geological structure of fractures increases the difficulty of prediction. In cases with low permeable matrix, heat conduction plays a vital role during the process of heat extraction. The dominating convective flow within the fractures carries the cold fluids towards the production well. Heat exchange happens between matrix and fracture behind the cold front via heat conduction such that the injected fluid is heated up again, while the surrounding rock is cooled. The quantitative analysis of the interplay between convection and conduction in the presence of fractures is thus not only of theoretical interest but also of practical significance. Geothermal development schemes can be optimized with the recognition of interactions between these mechanisms.

This complex interaction between subsurface properties and processes can best be captured and analysed with the help of numerical simulations. Numerical simulation, as a powerful and predictive tool, has been widely employed in uncertainty analysis, optimization, and production evaluation. High-performance reservoir simulation can improve decision making and optimize production strategy with very limited cost. Geothermal reservoir simulation entails the solution of mass and energy governing equations [23, 24]. The mass and energy governing equations are generally tightly coupled because of the fluid thermodynamic properties. A fully coupled, fully implicit scheme is widely adopted in geothermal simulation because of its unconditional stability. During a numerical simulation, the governing equations need to be discretized in both space and time to get approximate solutions. Usually, the formulation in discretized form is nonlinear and should be linearized to facilitate iterative solving. A Newton-Raphson based process is generally adopted to linearize the discretized formulations, which require the values of fluid properties and their derivatives. Complicated reservoir structures (e.g., in the presence of fractures and faults) usually present difficulties for the Cartesian grids to depict the geological structures accurately and require unstructured grids [25] to characterize the complexities.

Several simulators have been used in geothermal applications [26], such as TOUGH2 [27, 28], which is the state-of-the-art simulator for general-purpose numerical simulation of multi-phase fluid and heat transport in porous media. It has been widely used for geothermal projects [29–32]. In TOUGH2, the natural formulation is implemented with pressure and temperature (or saturation) as primary variables. The IAPWS-IF97 of the International Association for the Properties of Water and Steam [33] is used to calculate water thermodynamic properties. AD-GPRS (Automatic Differentiation General Purpose Research Simulator) [34, 35] is a powerful research simulation framework that also provides geothermal capabilities [36]. In AD-GPRS, both natural and molar formulations are implemented within the unified simulation framework, while the formulations used to calculate water and steam properties are the same as Faust and Mercer [37].

The complexity of physics and a large number of grid blocks within high-resolution geothermal models often challenge conventional simulation techniques. The complex physical processes (i.e., multi-phase flow, multi-component reactive transport) encountered in geothermal applications require robust, flexible, and efficient solutions. The physical space can become highly nonlinear due to the nonlinear behavior of fluid thermodynamic properties with respect to changes of pressure and temperature, especially when several phases exist in the system [38]. To accurately delineate the physical process happening underground, an advanced simulation strategy is necessary to improve the convergence of the nonlinear solutions. In addition, large-scale reservoir simulation with multi-million control volumes is often needed to characterize and predict the behavior of a geothermal reservoir slowing down the simulation process. Furthermore, to quantify uncertainties and optimize development strategies, a large ensemble of models are necessary to cover the wide range of parameter settings, which requires high-performance and reliability of forward simulations.

Delft Advanced Research Terra Simulator (DARTS) [39, 40] is a new modeling framework developed at TU Delft. It includes capabilities for the solution of forward and inverse problems for subsurface fluid and heat transport. For temporal and spatial discretization, a finite volume fully implicit method in combination with two-point flux approximation on unstructured grids is implemented in DARTS. In addition to conventional discretization in time and space, DARTS also utilizes discretization in physics with the Operator-Based Linearization (OBL) approach for the solution of highly nonlinear problems. The OBL approach was proposed recently for generalized complex multiphase flow and transport applications and aims to improve the simulation performance [41, 42].

In the OBL approach, the nonlinear terms (i.e., accumulation, flux) in governing partial differential equations are discretized and written in the operator form depending on the physical state. The corresponding operators are called state-dependent operators, which are tabulated into multi-dimensional tables in the parameter space. During the simulation process, state-dependent operators are evaluated at the required supporting points of the parameter space. Multi-linear interpolation is then applied to create a continuous description. This representation simplifies the construction of the Jacobian matrix and residuals since the complex physics calculations are translated into generic interpolation between supporting points, which are calculated adaptively [43]. As a result, the programming implementation is significantly improved and generalized, preserving high flexibility and performance of the code. Furthermore, the design of the simulation framework supports a further extension to the advanced parallel architectures, e.g. GPU [40, 44, 45].

1.1. THESIS OBJECTIVES

DARTS is constructed around the OBL framework. An important aspect is to add geothermal capability in DARTS and validate the accuracy and efficiency of geothermal simulations. In addition, the heat transfer processes are worth investigating in both low- and high-enthalpy reservoirs under the influence of physical and operational parameters for realistic highly heterogeneous property distribution. The research objectives addressed in this work are:

- Construct geothermal capability within the DARTS framework, including the implementation of a C++ kernel and a Python interface.

- Benchmark DARTS with state-of-the-art numerical simulators in geothermal simulations.
- Simulate realistic geothermal operations, including parameter sensitivity analysis and uncertainty quantification of models at the geological scale in the presence of heterogeneity.
- Study the interaction between thermal convection and conduction in complex heterogeneous fractured high-enthalpy geothermal systems; check the sensitivity of heat production to various parameters.
- Investigate the so-called 'negative compressibility' phenomenon when solving mass and energy equations of high-enthalpy geothermal systems in a fully-coupled way; improve its nonlinear convergence within the OBL framework.

1.2. THESIS OUTLINE

This dissertation starts with this introductory Chapter 1. Chapter 2 describes the development of the geothermal module in DARTS. It displays the conservation equations used for geothermal simulations and their operator forms within the OBL framework. With the flexibility of a Python interface, an open-source package is incorporated in DARTS for the calculation of water properties. In Chapter 3, comprehensive geothermal benchmark tests are performed between DARTS and other state-of-the-art simulators, published in *Applied Energy* [46]. The accuracy and efficiency of geothermal simulations in DARTS are validated with the one-, two- and three-dimensional models under low- and high-enthalpy conditions.

Chapter 4 studies different ways of upscaling the non-reservoir lithology (shale) to reduce the number of grid blocks in the model. Local and flow-based upscaling strategies are examined. They provide insights for further studies on upscaling thermal related parameters, though both of them are not suitable for general cases.

Following the benchmark tests, several geothermal applications are simulated using DARTS. Chapter 5, submitted to a journal, shows a sensitivity analysis of parameters in a real low-enthalpy geothermal reservoir with detailed geological characterizations. The concerning parameters for geothermal development are investigated. In addition, the capability and efficiency of DARTS simulating realistic models have been tested. In Chapter 6, systematic uncertainty quantification of the realistic model is performed on GPU version of DARTS. The concerned uncertainties of energy production and NPV have been recognized which are associated with different uncertainties in input parameters.

Chapter 7, submitted to ajournal, investigates the multi-phase flow in fractured high-enthalpy geothermal reservoirs. It provides a research workflow to study heat transfer in fractured systems, including mesh optimization, dynamic heat transfer analysis and parameter sensitivity study.

In Chapter 8, the so-called 'negative compressibility' issue is discussed. A new strategy is presented to improve the nonlinear convergence of a fully coupled solution of the mass and energy equations under high-enthalpy conditions.

2

GEOTHERMAL MODULE IN DARTS

Summary

The governing equations used to characterize the geothermal system are described. Following the idea of the OBL approach, the operator forms of the mass and energy conversation equations are presented. In addition, various well controls supported in geothermal simulations are illustrated. Finally, an external package for property calculation of water and steam is integrated into DARTS via the Python interface.

2.1. INTRODUCTION

DARTS is constructed within the Operator-based Linearization (OBL) framework for general purpose reservoir simulations. To introduce geothermal simulations into DARTS, the governing equations characterizing the geothermal system should be first expressed in form of operators, which are the functions of primary variables. These operators are then utilized to construct the interpolators, which are responsible for the linear interpolation of operators. The values and derivatives of these operators at the supporting points will be evaluated adaptively during the simulation or pre-calculated in form of tables through the physics implemented in either C++ or Python.

An important part of numerical simulations is the assembly of Jacobian matrix, which contains the values and derivatives of the concerning terms in the governing equations. In favor of the OBL approach, the assembly of Jacobian matrix in C++ is generalized and improved, which greatly facilitates the code development. The constructed linear system will then be passed to the dedicated linear solver for a solution. More details about the DARTS architecture are described in Khait [47].

To enable the convenient usage of DARTS, the functionalities in C++ are exposed to users via a Python interface. Therefore, users can control the simulations easily in Python. At the same time, the Python interface provides the possibility to integrate different external modules (e.g., packages for physical property calculation) into DARTS. For example, in the geothermal simulation, the IAPWS-IF97 package for the standard property calculation of water and steam is included. The details will be illustrated in the following sections of this chapter.

2.2. CONSERVATION EQUATIONS

Mass and heat transfer involves a thermal multiphase flow system, which requires a set of equations to depict the flow dynamics. In this section, the governing equations and detailed spatial and temporal discretization and linearization procedures are introduced.

2.2.1. GOVERNING EQUATIONS

For the investigated domain with volume Ω, bounded by surface Γ, the mass and energy conservation can be expressed in a uniformly integral way, as

$$\frac{\partial}{\partial t}\int_{\Omega} M^k d\Omega + \int_{\Gamma} \boldsymbol{F}^k \cdot \boldsymbol{n} d\Gamma = \int_{\Omega} q^k d\Omega. \tag{2.1}$$

Here, M^k denotes the accumulation term for the k^{th} component ($k = 1,\ldots,n_c$, indexing for the mass components, [e.g., water, CO_2] and $k = n_c + 1$ for the energy quantity); $\boldsymbol{F}^k$ refers to the flux term of the k^{th} component; $\boldsymbol{n}$ refers to the unit normal pointing outward to the domain boundary; q^k denotes the source/sink term of the k^{th} component.

The mass accumulation term collects each component distribution over n_p fluid phases in a summation form,

$$M^k = \phi \sum_{p=1}^{n_p} x_p^k \rho_p s_p, \quad k = 1,\ldots,n_c, \tag{2.2}$$

where ϕ is porosity, s_p is phase saturation, ρ_p is phase density [kg/m^3] and x_p^k is molar fraction of k component in p phase.

The energy accumulation term contains the internal energy of fluid and rock,

$$M^{n_c+1} = \phi \sum_{p=1}^{n_p} s_p U_p + (1-\phi) U_r, \tag{2.3}$$

where U_p is phase internal energy [kJ] and U_r is rock internal energy [kJ].

The rock is assumed compressible and represented by the change of porosity through:

$$\phi = \phi_0 \big(1 + c_r (p - p_{\text{ref}})\big), \tag{2.4}$$

where ϕ_0 is the initial porosity, c_r is the rock compressibility [1/bar] and p_{ref} is the reference pressure [bars].

The mass flux of each component is represented by the summation over n_p fluid phases,

$$\boldsymbol{F}^k = \sum_{p=1}^{n_p} x_p^k \rho_p \boldsymbol{u_p}, \quad k = 1, \dots, n_c. \tag{2.5}$$

Here the velocity $\boldsymbol{u_p}$ follows the extension of Darcy's law to multiphase flow,

$$\boldsymbol{u_p} = \mathbf{K} \frac{k_{rp}}{\mu_p} (\nabla p_p - \boldsymbol{\gamma_p} \nabla D), \tag{2.6}$$

where $\mathbf{K}$ is the full permeability tensor (generally zero non-diagonal elements are taken) [mD], k_{rp} is the relative permeability of phase p, μ_p is the viscosity of phase p [mPa·s], p_p is the pressure of phase p [bars], $\boldsymbol{\gamma_p} = \rho_p \boldsymbol{g}$ is the specific weight [N/m^3] and D is the depth [m]. The energy flux includes the thermal convection and conduction terms,

$$\boldsymbol{F}^{n_c+1} = \sum_{p=1}^{n_p} h_p \rho_p \boldsymbol{u_p} + \kappa \nabla T, \tag{2.7}$$

where h_p is phase enthalpy [kJ/kg] and κ is effective thermal conductivity [kJ/m/day/K].

The nonlinear equations are discretized with the finite volume method using the two-point flux approximation on general unstructured mesh in space and with the backward Euler approximation in time. For the i^{th} reservoir block, the governing equation in discretized residual form reads:

$$R_i^k = V_i \Big(M_i^k(\omega_i) - M_i^{k,n}(\omega_i^n) \Big) - \Delta t \Big(\sum_l a_l F_l^k(\omega) + Q_i^k(\omega) \Big) = 0. \tag{2.8}$$

Here V_i is the volume of the i^{th} grid block, ω_i refers to state variables at the current time step, ω_i^n refers to state variables at previous time step, a_l is the contact area between neighboring grids, and Q_i^k is the source or sink term of the k^{th} component. In the following description, only one (water) component is assumed existing in subsurface therefore $x_p^k \equiv 1$.

2.3. OPERATOR FORM OF GOVERNING EQUATIONS

DARTS includes capabilities for the solution of forward and inverse problems for subsurface fluid and heat transport. The OBL approach is employed in DARTS for the solution of highly nonlinear problems. It was proposed recently for generalized complex multiphase flow and transport applications and aims to improve the simulation performance [41, 42]. For spatial discretization, a finite volume fully implicit method in combination with two-point flux approximation on unstructured grids is implemented in DARTS. Besides conventional discretization in temporal and spatial space, DARTS also utilizes discretization in physical space using the OBL approach.

With the OBL approach, the governing equations are written in form of state-dependent operators. The state-dependent operators can be parameterized (Fig. 2.1) with respect to nonlinear unknowns in multi-dimension tables under different resolutions. The values and derivatives of the operators in the parameter space can be interpolated and evaluated based on supporting points. For the adaptive parameterization technique [43], the supporting points are calculated 'on the fly' and stored for later re-usage, which can largely save time for parameterization in high-dimension parameter space (i.e. in multi-component compositional simulations). At the same time, the Jacobian assembly becomes flexible with the OBL, even for very complex physical problems.

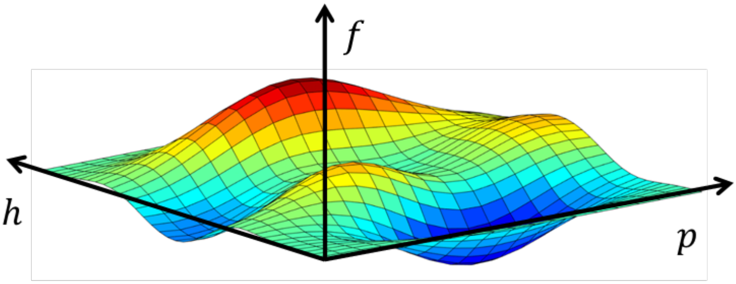

Figure 2.1: Parameterization of the geothermal operators in 2D (pressure & enthalpy) space with a predefined OBL resolution (adapted from [48]). Here, the size of the quadrilateral represents the resolution for operator interpolations.

Pressure and enthalpy are taken as the unified state variables of a given control volume in geothermal simulations. Upstream weighting of the physical state is used to determine the flux-related fluid properties determined at the interface l. The discretized mass conservation equation in operator form for girdblock i reads:

$$\phi_0 V\Big(\alpha(\omega) - \alpha(\omega_n)\Big) + \sum_l \Delta t \Gamma^l \Phi_{p,ij} \beta(\omega^u) = 0, \tag{2.9}$$

where V is the control volume, ω_n is the physical state of block i at the previous timestep, ω is the physical state of block i at the new timestep, ω^u is the physical state of upstream block and Γ^l is the fluid transmissibility. The state-dependent operators (the mass accumulation operator $\alpha(\omega)$ and the mass flux operator $\beta(\omega)$) are

$$\alpha(\omega) = \Big(1 + c_r(p - p_{ref})\Big) \sum_{p=1}^{n_p} \rho_p s_p, \tag{2.10}$$

$$\beta(\omega) = \sum_{p=1}^{n_p} \rho_p^l \frac{k_{rp}^l}{\mu_p^l}. \tag{2.11}$$

Here, the phase-potential-upwinding (PPU) strategy [43] is applied in DARTS to model the gravity effect. The potential difference of phase p between block i and j can be written as:

$$\Phi_{p,ij} = p_j - p_i - \frac{\delta_p(\omega_i) + \delta_p(\omega_j)}{2}(D_j - D_i), \tag{2.12}$$

where: ω_j is the physical state of block j at the new timestep, $\delta_p(\omega)$ is the density operator for phase p.

The discretized energy conservation equation in operator form can be written as:

$$\phi_0 V\Big[\alpha_{ef}(\omega) - \alpha_{ef}(\omega_n)\Big] + (1-\phi_0) V U_r \Big[\alpha_{er}(\omega) - \alpha_{er}(\omega_n)\Big] + \sum_l \Delta t \Gamma^l \Phi_{p,ij} \beta_e(\omega^u) + \\ \Delta t \sum_l \Gamma^l (T^i - T^j)\Big[\phi_0 \gamma_{ef}(\omega) + (1-\phi_0)\kappa_r \alpha_{er}(\omega)\Big] = 0, \tag{2.13}$$

where:

$$\alpha_{ef}(\omega) = \Big(1 + c_r(p - p_{ref})\Big) \sum_{p=1}^{n_p} \rho_p s_p U_p, \tag{2.14}$$

$$\alpha_{er}(\omega) = \frac{1}{1 + c_r(p - p_{ref})}, \tag{2.15}$$

$$\beta_e(\omega) = \sum_{p=1}^{n_p} h_p^l \rho_p^l \frac{k_{rp}^l}{\mu_p^l}, \tag{2.16}$$

$$\gamma_{ef}(\omega) = \Big(1 + c_r(p - p_{ref})\Big) \sum_{p=1}^{n_p} s_p \kappa_p. \tag{2.17}$$

This agglomeration of different physical terms into a single nonlinear operator simplifies the implementation of nonlinear formulations. Instead of performing complex evaluations of each property and its derivatives with respect to nonlinear unknowns, operators can be parameterized in physical space either at the pre-processing stage or adaptively with a limited number of supporting points. The evaluation of operators during the simulation is based on bi-linear interpolation, which improves the performance of the linearization stage. Besides, due to the piece-wise representation of operators, the nonlinearity of the system is reduced, which improves the nonlinear behavior [41, 43]. However, to delineate the nonlinear behavior in the system, especially strong nonlinearity (e.g., at high-enthalpy conditions), it is necessary to select a reasonable OBL resolution to characterize the physical space. Too coarse OBL resolution may lead to large error in the solutions [42].

A connection-based multi-segment well is used to simulate the flow in the wellbore [40]. The communication between well blocks and reservoir blocks is treated in the same way as between reservoir blocks. Besides, the top well block is connected with a ghost control volume, which is selected as a placeholder for the well control equations. The bottom hole pressure (BHP), volumetric and mass rate controls are available in DARTS to model various well conditions.

As for the BHP well control, the injector and/or producer will operate under fixed bottom hole pressure. A pressure constraint is defined at the ghost well block:

$$p - p^{target} = 0. \tag{2.18}$$

The volumetric rate control in DARTS is implemented through the volumetric rate operator $\zeta_p^{vol}(\omega)$:

$$Q_p^{vol} - Q^{target} = 0, \tag{2.19}$$

$$Q_p^{vol} = \Gamma^l \frac{\beta(\omega) s_p(\omega)}{\rho_t(\omega)} \Delta p = \Gamma^l \zeta_p^{vol}(\omega) \Delta p, \tag{2.20}$$

where Q_p^{vol} is the calculated volumetric rate [m^3/day], Q^{target} is the target flow rate [m^3/day], $\beta(\omega)$ is the mass flux operator as shown in Eq. (2.11), $\rho_t(\omega)$ is the total fluid density [kg/m^3].

Similarly, the mass rate control is defined as:

$$Q_p^{mass} - Q^{target} = 0, \tag{2.21}$$

$$Q_p^{mass} = \Gamma^l \frac{\rho_p(\omega)\beta(\omega) s_p(\omega)}{\rho_t(\omega)} \Delta p = \Gamma^l \zeta_p^{mass}(\omega) \Delta p, \tag{2.22}$$

where Q_p^{mass} is the calculated mass rate [kg/day], $\zeta_p^{mass}(\omega)$ is the mass rate operator.

Any of the described well controls can be coupled with energy boundary conditions, defined by temperature or enthalpy of the injected fluid at the injection well. Since temperature is the function of pressure and enthalpy, it is expressed in operator form and the temperature well control reads:

$$T(\omega) - T^{target} = 0, \tag{2.23}$$

where $T(\omega)$ is the temperature operator, T^{target} is the target temperature of injected fluid. Alternatively, enthalpy of the injected fluid can be defined:

$$h - h^{target} = 0, \tag{2.24}$$

where h is the enthalpy of the well control block, h^{target} is the target enthalpy of injected fluid. For the production well control, enthalpy is taken equal to that of the upstream well block.

2.4. INCORPORATION OF IAPWS PROPERTY IN DARTS

To keep the high performance, essential cores (e.g. linear solver, well controls, OBL interpolation, etc.) in DARTS are programmed in C++ on different platforms (e.g. CPU [49] and GPU [44]). Different simulation engines for various physical processes (e.g., geothermal and compositional simulations) are implemented in a unified framework. To make the simulator flexible, C++ classes are exposed via a Python interface, which enables users to manipulate DARTS and easily control the simulation process. In this way, DARTS possesses both the performance of C++ and flexibility of the scripting language.

The Python interface provides DARTS with the capability to embrace physics describing specific physical processes. Besides the set of integrated geothermal properties implemented in C++, users can define property formulation in Python. Taking advantage of OBL, the self-defined physics can be used to calculate supporting points while the derivatives are evaluated automatically during interpolation. Therefore, the flexibility of the Python interface provides DARTS with the extended capability to model various physical processes. At the same time, the main C++ routine guarantees the efficiency of the simulation.

In DARTS, an interface, called ‘*property_evaluator_interface*’, is predefined for property classes in C++. The interface is exposed to Python. This facilitates users to introduce custom properties into the simulation. The rock and fluid property classes, called ‘*property_evaluator*’, are inherited from the interface. To calculate the specific property value, users should define the ‘*evaluate*’ method, which takes, in general, the unknown variables (or state variables) as input parameters (e.g., pressure and enthalpy for geothermal).

Here, I take a geothermal case as an example to demonstrate how the custom properties are defined in practice. The open-source industrial standard IAPWS package supports the calculations of comprehensive water properties. Using the architecture for property definition, I designed a wrapper around the required functionalities for DARTS simulation. Here, I take the ‘*temperature_evaluator*’ as an example; see Algorithm 1. This class is used to calculate the temperature value based on the primary variables, P and h. It is inherited from the based class called ‘*property_evaluator_iface*’, which defines the interface for the functionality of ‘*evaluate*’. In standard IAPWS package, the P-h physical space is divided into different regions based on the physical state of water. The temperature calculation is dependent on the division of these regions. For each region, there is a corresponding function to calculate the temperature value. When defining the ‘*evaluate*’ function in ‘*temperature_evaluator*’, it wraps the logic of how temperature is calculated in IAPWS. Therefore, the temperature will be evaluated just based on the input values of pressure and enthalpy.

In this way, the required properties are introduced into DARTS. Likewise, users can conveniently define their own property formulations in Python. In the initialization of a simulation, the objects of ‘*property_evaluator*’ are created. The property values will then be evaluated during the course of the simulation.

Algorithm 1 Temperature evaluator

```
class temperature_evaluator(property_evaluator_iface):
    def __init__(self):
        super().__init__()
    def evaluate(self, state):
        P, h ⇐ state[0], state[1]
        region ⇐ _Bound_Ph(P, h)
        if (region == 1):
            T ⇐ _Backward1_T_Ph(P, h)
        elif (region == 2):
            T ⇐ _Backward2_T_Ph(P, h)
        else:
            ...
    return T
```

3

GEOTHERMAL BENCHMARKS

Summary

Numerical simulations have been widely used for the evaluation and optimization of energy production from the subsurface including geothermal applications. Accurate prediction of temperature and pressure distribution is essential for geothermal reservoir exploitation with cold water re-injection. In this chapter, DARTS is compared with the state-of-the-art simulation frameworks under comprehensive benchmark tests. We demonstrate that DARTS achieves a good match for both low- and high-enthalpy conditions in comparison with other simulators. At the same time, DARTS provides high performance and flexibility of the code due to the OBL approach, which makes it particularly useful for uncertainty quantification in geothermal processes involving complex physics.

The material presented in this chapter has been published in Applied Energy 2020, 264 [46].

3.1. INTRODUCTION

In general, aqueous brine is used as the fluid for thermal circulation in geothermal development. For some applications, CO_2 [10, 18] has been proposed as a heat carrier. In addition, minerals can be dissolved by the brine with a number of chemical reactions [50], making the fluid chemistry even more complicated, and hydrocarbon components can be mixed with brine and co-produced [41]. Such types of models require a complicated equation-of-state (EoS) to describe realistic phase behavior.

To simplify the benchmark comparison, I start with the basic situation where only the water component exists in the studied system. Although only a single component is involved, both liquid and gaseous phases are present in high-enthalpy systems. The complex EoS of water is required for accurate characterization, as described in [33]. The large contrast in thermodynamic properties between liquid water and saturated steam should also be taken into consideration for efficient simulations in high-enthalpy systems.

In this section, a set of benchmark tests are conducted between DARTS and state-of-the-art reservoir simulators TOUGH2 and AD-GPRS. The comparisons are performed with one-, two- and three-dimensional models. At the beginning of each comparison, the selected model with initial and boundary conditions is described, after which the simulations are performed and the result comparisons are shown. Finally, the performance of different simulators is displayed.

3.2. ONE-DIMENSIONAL CASE

In a geothermal reservoir, fluid is mainly transported convectively from an injection well or influx boundary to a production well. At the same time, heat is transported through convective and conductive flow, where convection usually dominates. However, conduction also plays an important role in the development of a geothermal reservoir as the main mechanism of re-charging cold re-injected fluid. Besides, the properties of reservoir fluid can be significantly affected by phase changes. For example, the difference in densities of liquid water and steam has a great impact on heat transport and fluid distribution. Accurate simulation of these mechanisms is necessary for both forward and inverse modelling.

Here, the solutions (i.e., pressure, temperature, saturation) of DARTS are validated with solutions obtained using the two state-of-the-art simulators, TOUGH2 an AD-GPRS. Horizontal and vertical models are used in one-dimensional benchmarks.

3.2.1. HORIZONTAL CASE

Table 3.1 lists the parameter settings used in the horizontal model. Fig. 3.1 shows the initial and boundary conditions of the horizontal model. This model is initialized with hot steam to mimic high-enthalpy geothermal reservoir conditions. The horizontal boundary in the X direction is set with free-flow condition while a no flow condition is assigned to the rest of the boundaries. By influx of cold water, the reservoir block containing hot steam will be cooled down and the steam condensation will be coupled with the flow. Three simulators are set with identical parameters and run with a similar simulation strategy (e.g., time-step, convergence tolerance, etc.).

Table 3.1: Parameter settings used in 1D horizontal model.

Parameter	**Value**
Grid dimension	$50 \times 1 \times 1$
Grid size, m	$10 \times 10 \times 10$
Volumetric heat capacity, kJ/m^3/K	2200
Heat conductivity, kJ/m/day/K	180
Permeability, mD	10
Porosity	0.2

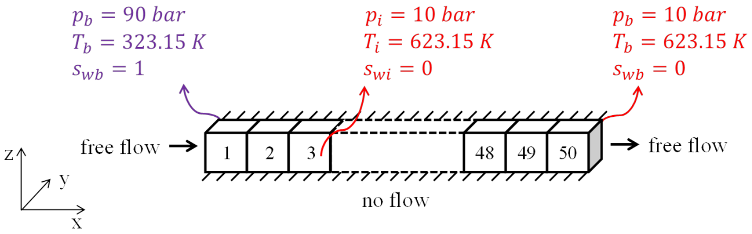

Figure 3.1: Schematic for 1D horizontal model with boundary and initial conditions.

The solutions generated by different simulators are shown in Fig. 3.2. DARTS achieves a perfect match with TOUGH2 in pressure, temperature, and saturation solutions. It accurately captures the thermal propagation with a sharp saturation front, behind which a two-phase transition zone reflecting the interaction between cold water and hot steam is observed. Fig. 3.2b displays the 'staircase' shape, which can be interpreted as the reflection of phase transition on the temperature profile. The first stair represents the two-phase transition zone where pressure and temperature are independent. Although there is a slight difference between the solution of DARTS and TOUGH2 v.s. AD-GPRS, the difference is minor.

3.2.2. OBL CONVERGENCE OF 1D HORIZONTAL MODEL

By performing the interpolation in physical space, OBL significantly reduces the computational resources needed for property calculation. However, reasonable resolution in physical space is necessary to accurately capture the nonlinearity of rock and fluid properties [41, 42]. After a good match shown in the 1D horizontal case, the same model is used for sensitivity analysis of the influence of OBL resolution on the accuracy of the solutions. Since the model is initialized with high-enthalpy conditions and presents a complex phase transition process, it is expected to be more challenging for OBL to match the reference solution with a limited resolution due to the high nonlinearity of governing physics. Here, simulations with different OBL resolutions were performed and the corresponding solutions are compared in Fig. 3.3.

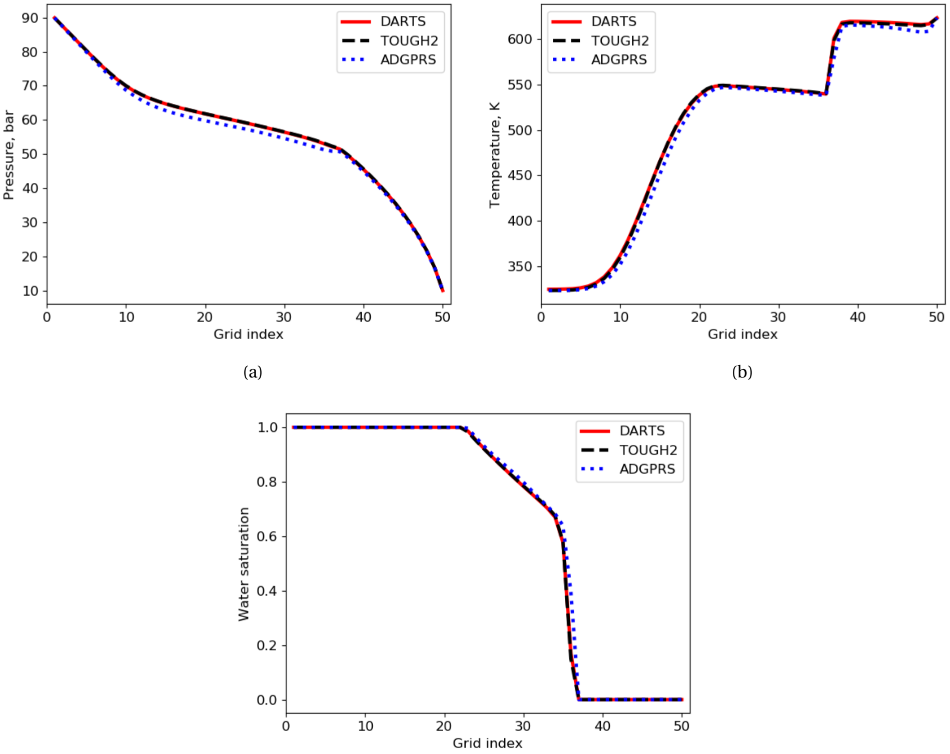

(a) (b) (c)

Figure 3.2: Comparison of pressure (a), temperature (b) and water saturation (c) solutions of three simulators for 1D horizontal model after 500 days.

In Fig. 3.3, the red solid line represents the solution with 512-points of OBL resolution, which is taken as the reference solution. The lowest 8-points resolution introduces the largest error in all of the solution profiles, which is because the coarsest resolution can barely capture the nonlinearity of physics. With the increase of OBL resolution, the solution approaches the reference results gradually.

Already with an OBL resolution of 16 points, DARTS closely matches the reference solution for the pressure profile, as shown in Fig. 3.3a. However, the temperature and saturation profiles in Fig. 3.3b and Fig. 3.3c demonstrate that it is still difficult to obtain accurate results with merely 16 points, and at least 128 points are needed to accurately capture the saturation shock, which indicates that the physical nonlinearity at high-enthalpy conditions heavily relies on the thermodynamic properties, and an accurate thermal solution (i.e., temperature or enthalpy) is essential for the representation of the full physical process in the geothermal reservoir. With an OBL resolution of 256 points, the solution overlaps with the reference line, which demonstrates that sufficient accuracy has been achieved.

Fig. 3.4 shows the nonlinear iteration performed by DARTS at different resolutions

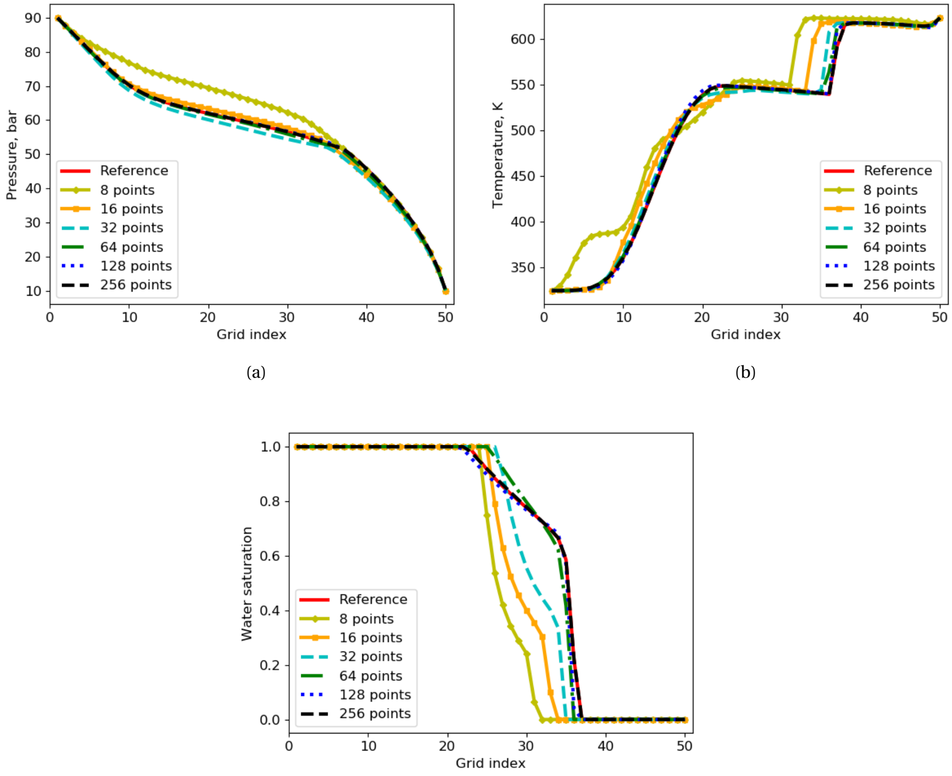

(a) (b)

(c)

Figure 3.3: Pressure (a), temperature (b) and water saturation (c) curves under different OBL resolutions for 1D horizontal model.

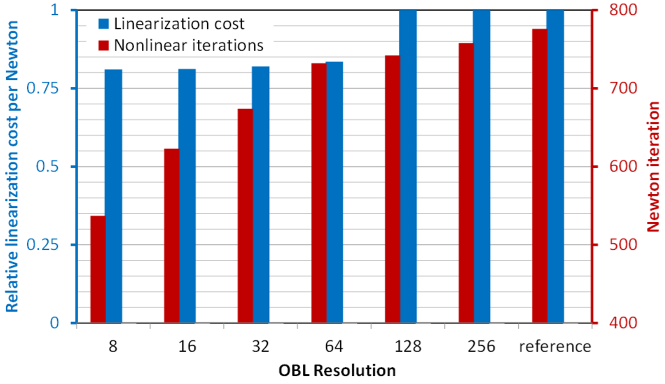

Figure 3.4: Simulation statistics under different OBL resolutions.

and the relative linearization cost per nonlinear iteration in comparison with the reference solution. Here, the relative linearization cost represents the ratio of the CPU time between OBL and reference solution per nonlinear iteration. With the coarsening of OBL resolution, the total number of nonlinear iterations decreases: the coarser the resolution is, the more linear is the physical description and, hence, easier for the simulator to converge. Besides, the linearization cost per Newton step does not decrease much with the coarsening of the resolution. This can be explained by the fact that the time consumption for calculating the supporting points in the physical space only takes a small portion of the linearization process. However, the accuracy of the solution decreases with the resolution as is shown in Fig. 3.3. A reasonable OBL resolution should be selected to keep both accuracy and efficiency when dealing with highly nonlinear physics.

3.2.3. VERTICAL CASE WITH BUOYANCY UNDER DIFFERENT BOUNDARY CONDITIONS

In reality, the payzone of a geothermal reservoir can be charged from the overburden and underburden layers in form of either mass or heat inflow. When the charging effect is strong, the fluids will be boiled and flow upwards. Since liquid water is much heavier than steam, water flows downwards while steam rises up following the effect of buoyancy. During the equilibrium process, heat residing in different phases is exchanged with the transport of fluids. Resulting from this thermal transport, phase transitions take place due to the large variation of enthalpy between liquid water and steam phase. Besides, the pressure will be redistributed under the gravity effect, which influences the counterbalance of water and steam phase as well. Especially, water vaporizes into steam as the pressure decreases while moving upwards. Meanwhile, the upper cooler fluids move downwards due to buoyancy. Consequently, the fluids and heat circulate vertically and reach equilibrium in the end. To simulate this phenomenon, three cases with different boundary conditions are designed and utilized for comparison with TOUGH2 and AD-GPRS. The intention is to cover the possible challenges existing in simulating thermal buoyancy-driven flow. Therefore, the capability of DARTS to simulate highly nonlinear flow can be examined and verified.

Table 3.2: Parameter settings for vertical models with boundary of constant mass and heat source

Parameter	**Value**
Grid dimension	$1 \times 1 \times 11$
Grid size, m	$100 \times 100 \times 20$
Permeability kz, mD	50
Porosity	0.2
Rock volumetric heat capacity, kJ/m^3/K	2500
Rock heat conductivity, kJ/m/day/K	172.8
Initial temperature, K	283.15

First, the cases with bottom boundary of constant mass or heat source are compared. The parameter settings of the model are listed in Table 3.2. The top of the setup connects to the atmosphere, therefore the top pressure is maintained constant as one bar. The initial pressure of the rest of the grid blocks follows the hydrostatic pressure gradient and is proportional to the depth.

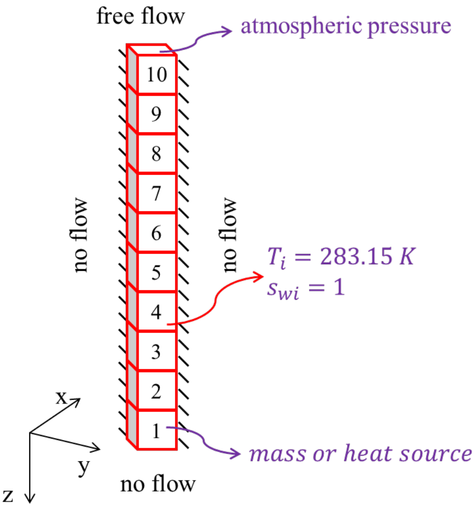

Figure 3.5: Schematic for 1D vertical model with boundary and initial conditions.

- Constant mass source at bottom boundary (DARTS v.s. TOUGH2)

In this case, a mass source is placed at the bottom grid block in the model (Fig. 3.5). As the simulation proceeds, the downward flow from the top and upward flow from the bottom mix somewhere in the middle. The numerical solutions (e.g., temperature at equilibrium) depend on the relative strength of the counterflow, which provides big challenges to the numerical simulators. Here, two different mass rates are selected: (1) mass rate: 0.03 kg/s, enthalpy: 1500 kJ/kg; (2) mass rate: 2 kg/s, enthalpy: 1500 kJ/kg. Fig. 3.6 and Fig. 3.7 display the solutions of pressure, temperature and water saturation of DARTS and TOUGH2 at the final equilibrium state.

With a weak mass source, slight boiling happens in the bottom grid cells (Fig. 3.6c). The hot upward flow can only sustain water vaporization within a limited range. At the same time, the temperature curve is divided into two parts with different slopes. The boiled grid blocks display larger temperature increment due to phase change, while the rest, without water vaporization, display mild temperature increase with a similar gradient.

The solutions of temperature and water saturation behave differently with a stronger mass rate (Fig. 3.7). Water vaporization happens in all grid blocks except the top one connected to the atmosphere. In addition, the temperature is highly elevated because of

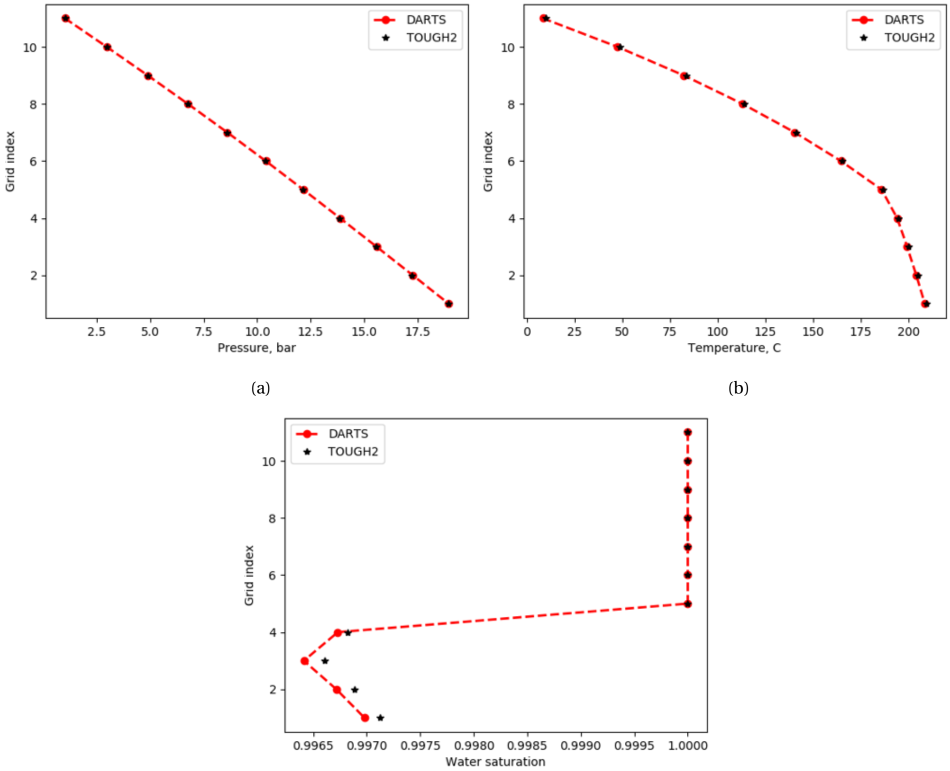

(a)

(b)

(c)

Figure 3.6: Comparison of pressure (a), temperature (b) and water saturation (c) solutions for 1D vertical model at equilibrium, with mass rate of 0.03 kg/s.

the strong upflow of the hot fluids. In both compared cases, good matches are achieved between DARTS and TOUGH2.

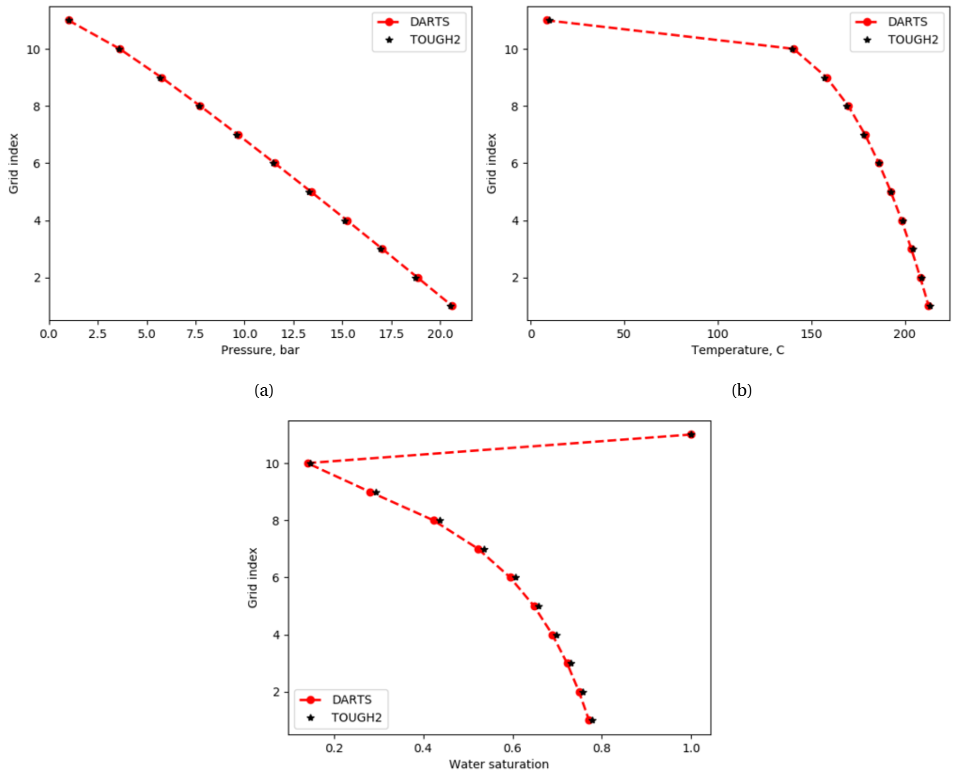

(a) (b)

(c)

Figure 3.7: Comparison of pressure (a), temperature (b) and water saturation (c) solutions for 1D vertical model at equilibrium, with mass rate of 2 kg/s.

- Constant heat source at bottom boundary (DARTS v.s. TOUGH2)

In this case, a heat source is placed at the bottom grid block. By heat source, it refers to no generation of mass, but only heat generation in the model. It simulates the scenario that a system is heated up and boiled by the synergy of buoyancy and heat conduction. To implement the heat source, the target term is added to the right hand side of the energy conservation equation. Here, two different values of heat source are selected: (1) heat rate: 30 kJ/s; (2) heat rate: 900 kJ/s. Fig. 3.8 and Fig. 3.9 display the solutions of pressure, temperature and water saturation of DARTS and TOUGH2 at the final equilibrium state.

With a weak heat source, boiling initiates in the bottom grid cells (Fig. 3.8c). While the heat source becomes strong, boiling occurs in all grid cells except the top one connected to the atmosphere (Fig. 3.9c). Good matches are achieved in the numerical solutions of the compared cases.

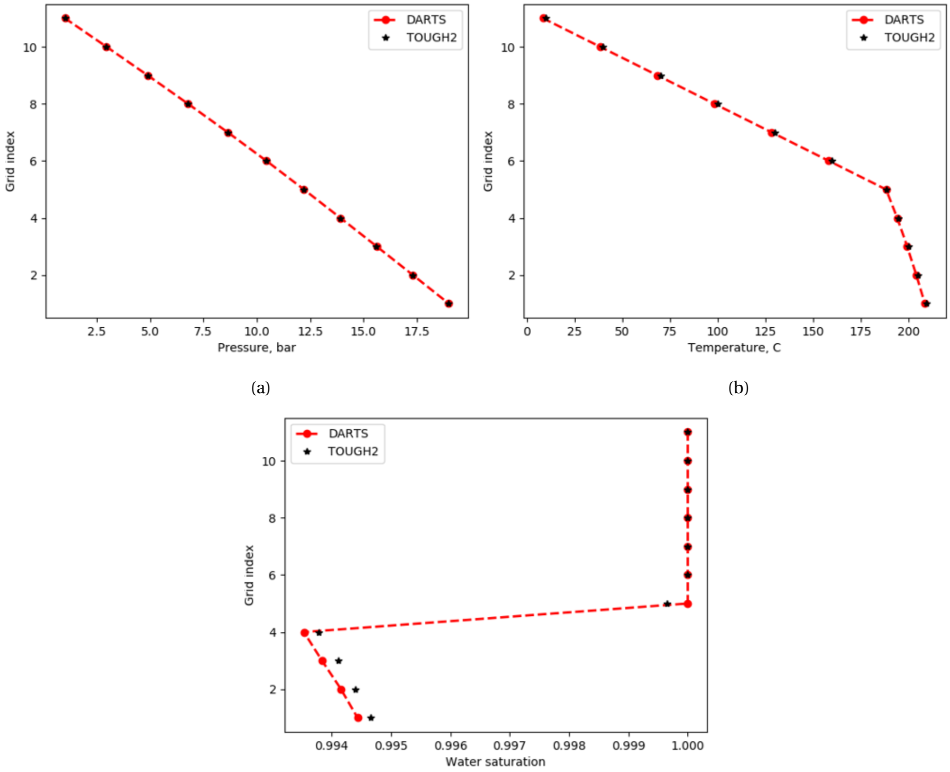

(a)

(b)

(c)

Figure 3.8: Comparison of pressure (a), temperature (b) and water saturation (c) solutions for 1D vertical model at equilibrium, with heat rate of 30 kJ/s.

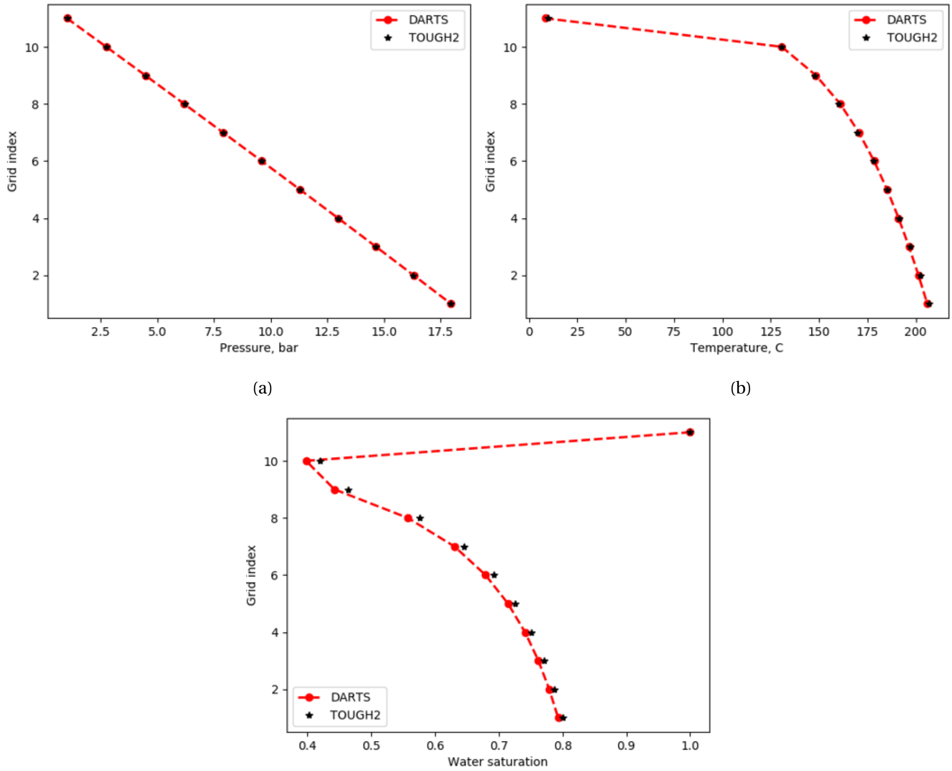

(a)

(b)

(c)

Figure 3.9: Comparison of pressure (a), temperature (b) and water saturation (c) solutions for 1D vertical model at equilibrium, with heat rate of 900 kJ/s.

- Open flow at bottom boundary (DARTS v.s. TOUGH2 and AD-GPRS)

The parameter settings of the model are listed in Table 3.3. Fig. 3.10 shows the initial and boundary conditions of the vertical model. This model is initialized with cold water at the top grid cell while hot steam for the rest cells. The initial pressure is set as uniform throughout all grid cells. The top boundary is set with no-flow condition while the free-flow condition is applied at the bottom. Due to the large contrast of thermodynamic properties between water and steam, the fluids will redistribute and reach equilibrium under the effect of gravity.

During the equilibrium process, heat residing in different phases is exchanged with the transport of fluids. The pressure will be redistributed under the gravity effect, which influences the counterbalance of water and steam phase as well.

Fig. 3.11 and Fig. 3.12 display the evolution of water saturation and enthalpy profiles for different time as the simulation proceeds. Water saturation builds up from bottom to the upper cells while the steam phase is gradually replaced in these cells. After 500 days, the equilibrium is reached and the number of cells occupied by the steam phase is

Table 3.3: Parameter settings for the vertical model with boundary of open flow

Parameter	**Value**
Grid dimension	$1 \times 1 \times 10$
Grid size, m	$20 \times 20 \times 20$
Permeability kz, mD	50
Porosity	0.2
Rock volumetric heat capacity, kJ/m^3/K	2200
Rock heat conductivity, kJ/m/day/K	180

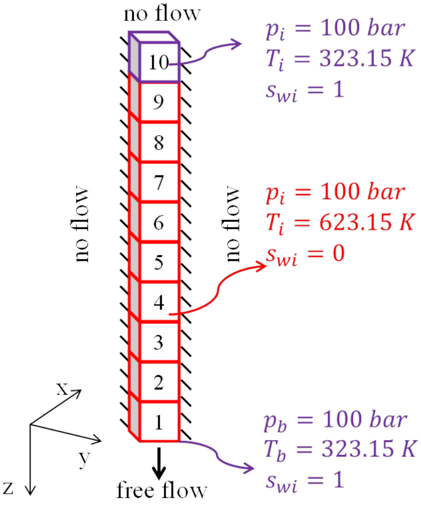

Figure 3.10: Schematic for 1D vertical model with boundary and initial conditions.

reduced due to the heat exchange. The transport and communication of energy between cells can be observed on the enthalpy profile, where enthalpy is mixed with downwards flow of water and up-floating of steam. In the end, reversed enthalpy distribution is obtained with higher enthalpy at the top compared to the initial distribution.

Fig. 3.13 shows the comparison of the result between DARTS, TOUGH2, and AD-GPRS. DARTS achieves a good match with TOUGH2 in all solution profiles. In Fig. 3.13a, the pressure curve consists of two parts with different slopes related to different fluid phase distribution (in Fig. 3.13c) among the grid cells. Again, there is a slight difference in the temperature curve in comparison with AD-GPRS, but the difference is minor and within the acceptable range.

3.2.4. OBL CONVERGENCE OF 1D VERTICAL MODEL

Similar to the 1D horizontal case, convergence analysis of the 1D vertical model at different OBL resolutions is performed. Strong nonlinearity is present in the system due to

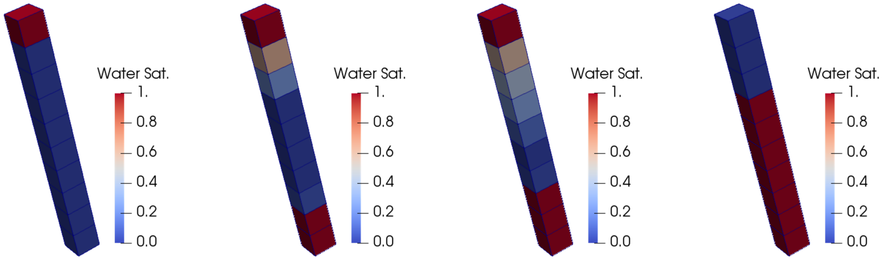

Initial saturation distribution After 100 days After 200 days After 500 days

Figure 3.11: Evolution of water saturation profile during equilibration.

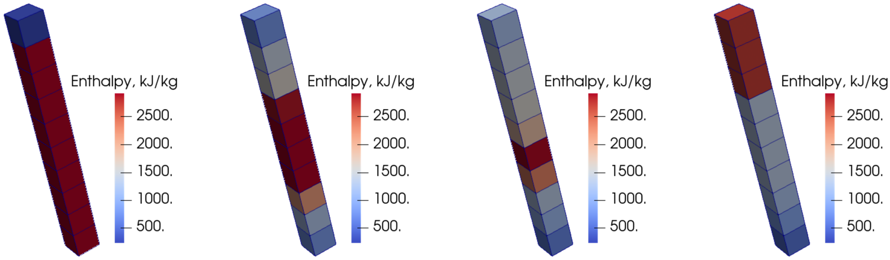

Initial enthalpy distribution After 100 days After 200 days After 500 days

Figure 3.12: Evolution of enthalpy profile during equilibration.

the co-existence of multi-phase flow, heat transfer and buoyancy.

The result comparisons for pressure, temperature and water saturation are shown in Fig. 3.14. The red line represents the solution with 512-points of OBL resolution and is considered the reference solution again. The solution obtained with the lowest 8-points OBL resolution is the farthest away from the reference one, which indicates this OBL resolution is too coarse to accurately delineate the highly nonlinear equilibrium process. With the increase of OBL resolution, the solution error starts to decrease and 256-points resolution provides an accurate solution. The OBL resolution required for accurate solution for this case is the same with the 1D horizontal case, which reflects that these two cases represent a similar nonlinearity.

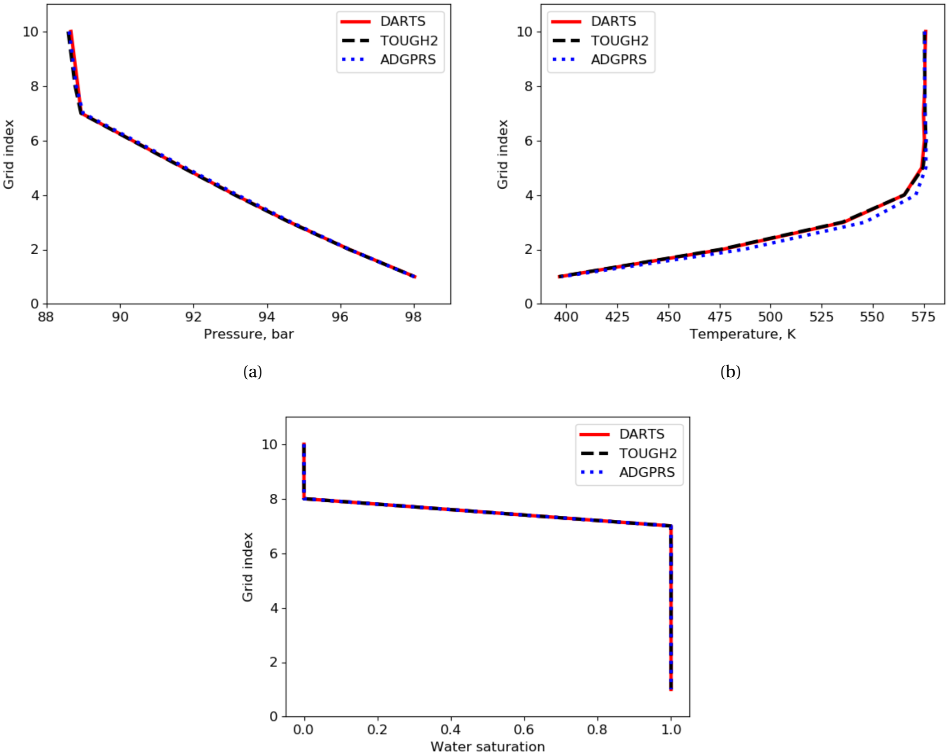

(a)

(b)

(c)

Figure 3.13: Comparison of pressure (a), temperature (b) and water saturation (c) solutions of three simulators for 1D vertical model after 500 days.

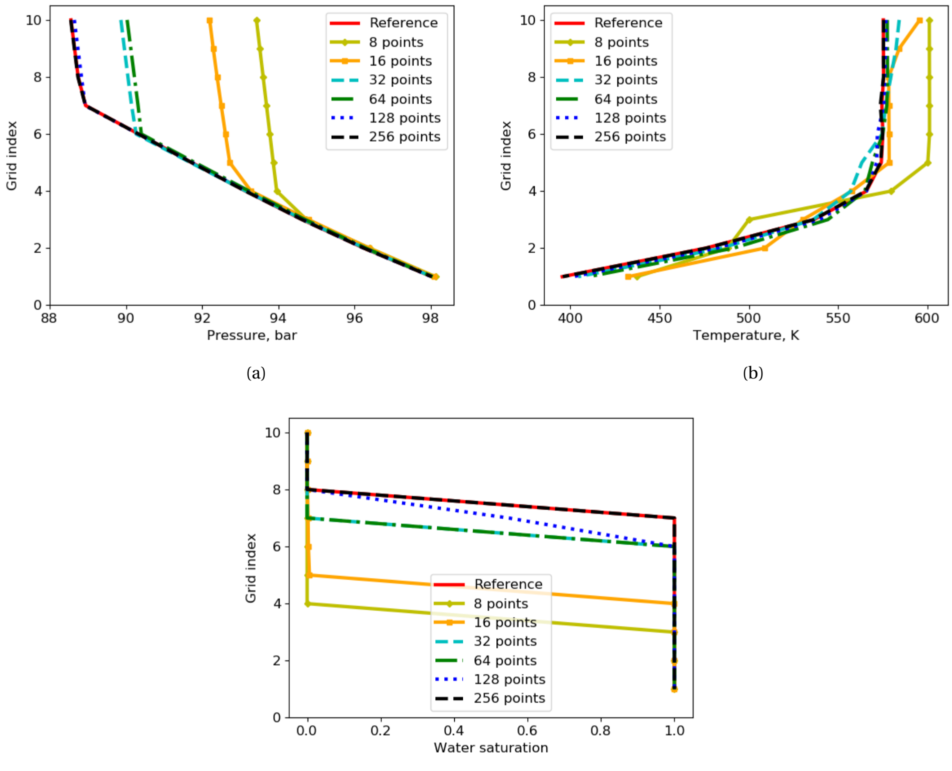

(a)

(b)

(c)

Figure 3.14: Pressure (a), temperature (b) and water saturation (c) curves under different OBL resolutions for 1D vertical model with gravity.

3.3. TWO-DIMENSIONAL CASE

Realistic geothermal reservoirs are usually heterogeneous. A large permeability contrast requires a robust numerical scheme. Besides, the initial condition of a geothermal reservoir can vary from low-enthalpy to high-enthalpy conditions, depending on the thermal gradient and depth of the reservoir, which may lead to significant variations in thermodynamic properties of the in-situ fluids. All of these uncertainties in the subsurface cause difficulties for reservoir simulations. Therefore, the capability of DARTS in dealing with realistic heterogeneous models under different initial conditions should be verified.

3.3.1. CASE 1

In this part, a one-layer model extracted from a synthetic geological model from the West Netherlands Basin - WNB [22], an inverted rift basin in the Netherlands, is chosen for the two-dimensional comparison. Fig. 3.15a displays the porosity distribution of the model, which ranges from 0.1 to 0.37.

Since the geological model represents a fluvial system, the porosity is in channelized

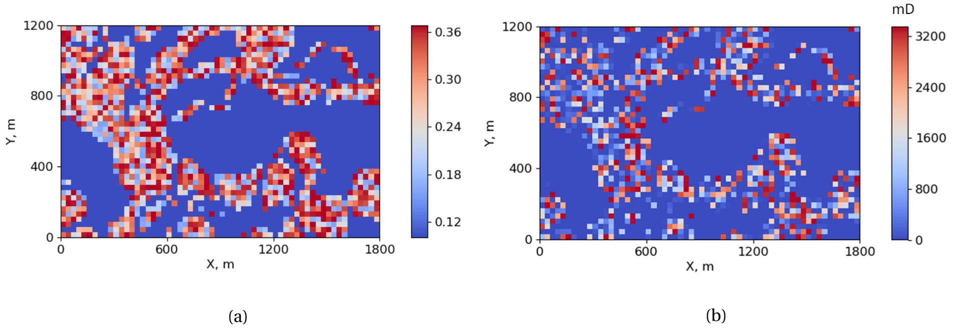

Figure 3.15: Porosity (a) and permeability (b) distribution of 2D model.

distribution. The dimension of the model is 60 × 40 × 1 with grid size of 30 m × 30 m × 2.5 m.

A closed boundary condition for both the heat and mass is used in the 2D comparison. Both low- and high-enthalpy initial conditions are selected for the comparison with TOUGH2 and AD-GPRS. In addition, different well controls for injection and production wells are employed to make the comparison more representative.

- Comparison of DARTS and TOUGH2

Table 3.4: Initial condition and well controls used for comparison between DARTS and TOUGH2.

	Low-enthalpy	**High-enthalpy**
Initial temperature, K	348.15	623.15
Initial pressure, bars	100	100
Injection enthalpy, kJ/kg	100	100
Injection rate, kg/day	36000	36000
Production pressure, bars	80	80
Simulation time, years	100	100

Table 3.4 shows the reservoir initial conditions and well controls used in validation with TOUGH2. The results are shown in Fig. 3.16a and Fig. 3.16b for low-enthalpy and high-enthalpy conditions respectively. The left column shows the TOUGH2 solution, which is taken as the reference one in the comparison. The right column displays the relative difference between DARTS and TOUGH2 solutions in pressure and temperature. A good match is observed in both pressure and temperature maps for both low-enthalpy and high-enthalpy conditions. The maximum relative temperature difference is around 1.6% for low-enthalpy conditions, while for the high-enthalpy scenario, the maximum temperature difference is around 3.5% in very few grid cells around the displacement front.

Since a no-flow condition is assigned at the boundary, the pressure gradient building up between injector and producer guides the direction of fluid flow. Besides, fluid tends

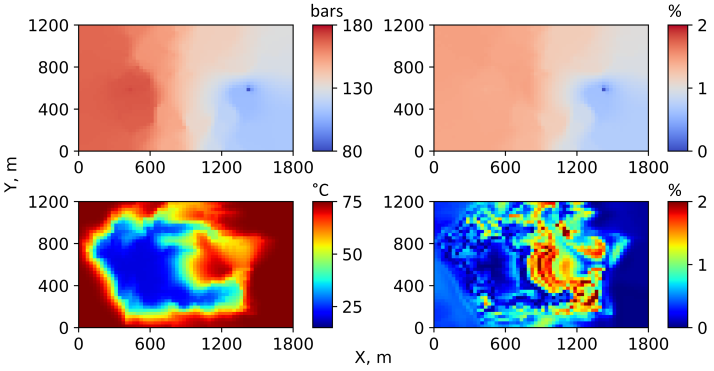

(a) Low-enthalpy condition

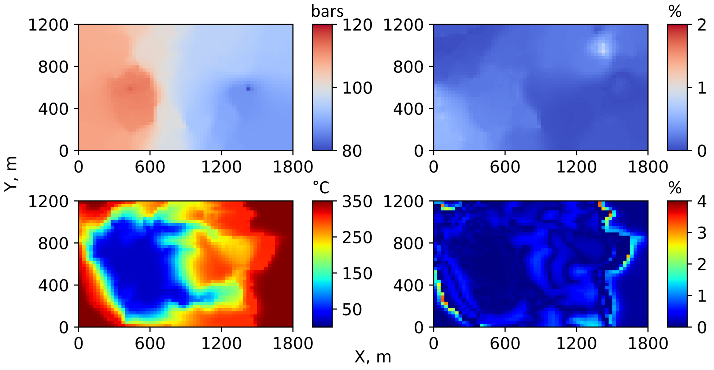

(b) High-enthalpy condition

Figure 3.16: Comparison of simulation results after 100 years: (a) low-enthalpy condition, (b) high-enthalpy condition. Left: pressure (top) and temperature (bottom) profiles of TOUGH2. Right: relative difference between TOUGH2 and DARTS for pressure (top) and temperature (bottom).

to flow within the high permeable channels, due to the channelized distribution of reservoir properties. In the high-enthalpy case, because of the higher mobility of steam, the water-swept area is larger than that of the low-enthalpy case, even with the same production scheme.

- Comparison of DARTS and AD-GPRS

Table 3.5 shows the reservoir initial conditions and well controls used in the validation with AD-GPRS. Fig. 3.17a and Fig. 3.17b show the solution and the difference between DARTS and AD-GPRS under low-enthalpy and high-enthalpy conditions respectively, where AD-GPRS solutions are considered as the reference. In Fig. 3.17, the left column shows the AD-GPRS solutions in pressure and temperature and the right column displays the relative difference between DARTS and AD-GPRS solutions. As it is shown, a good match is observed in both pressure and temperature map under both low-enthalpy and high-enthalpy conditions. The maximum relative temperature difference is around 3.0% for low-enthalpy conditions, while for the high-enthalpy case, the maximum difference is around 3.5% in a very few grid cells.

Table 3.5: Initial condition and well controls used for comparison between DARTS and AD-GPRS.

	Low-enthalpy	**High-enthalpy**
Initial temperature, K	348.15	623.15
Initial pressure, bars	100	100
Injection temperature, K	298.15	298.15
Injection rate, m^3/day	40	40
Production pressure, bars	80	80
Simulation time, years	100	100

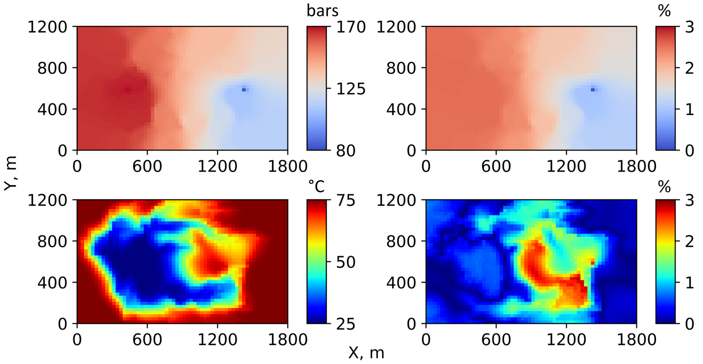

(a) Low-enthalpy condition

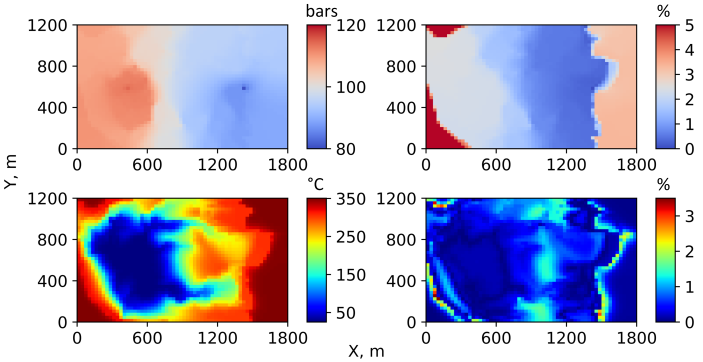

(b) High-enthalpy condition

Figure 3.17: Comparison of simulation results after 100 years: (a) low-enthalpy condition, (b) high-enthalpy condition. Left: pressure (top) and temperature (bottom) profiles of AD-GPRS. Right: relative difference between AD-GPRS and DARTS for pressure (top) and temperature (bottom).

3.3.2. CASE 2

Next, a fracture network extracted from an outcrop imaging of the Whitby Mudstone Formation [51] is taken to run and compare simulation results. Discrete Fracture Model (DFM) [52] is selected to characterize the fracture network with unstructured grid discretization; see more details on the DFM discretization in [53]. The model dimension is of 1200m × 1700m × 1m. The geometry and discretized grids of the fracture network are depicted in Fig. 3.18. The model consists of 6998 matrix cells and 1382 fracture cells. The basic parameter settings used in this model are listed in Table 3.6.

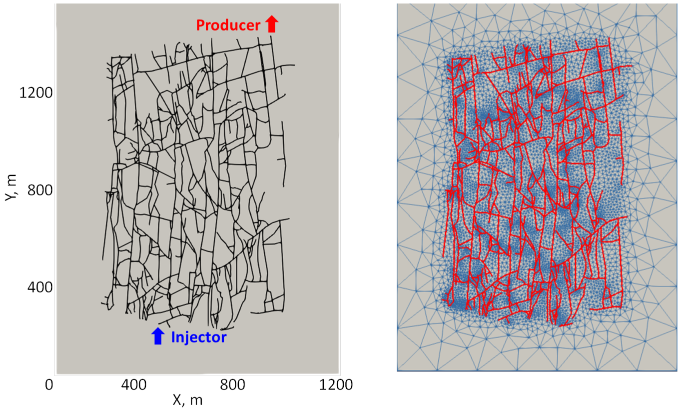

(a)

(b)

Figure 3.18: (a) 2D fracture model and (b) the grid discretization.

Table 3.6: Parameter settings used in 2D benchmark test with the fracture model.

Parameter	**Value**
Pressure, bars	100
Temperature, K	348.15
Porosity	0.02
Matrix permeability, mD	0.001
Fracture width, m	3×10^{-4}
Injection rate, m^3/day	100
Injection temperature, K	308.15
Production BHP, bars	70
Simulation time, years	10

The model is run in both AD-GPRS and DARTS with fixed injection rate and production BHP under low-enthalpy condition. Fig. 3.19 shows the results of AD-GPRS, which is taken as the reference, and the relative difference between AD-GPRS and DARTS. A reasonable match is achieved between the two simulators with a maximum relative pressure difference of 6% and maximum relative temperature difference of 1.6%.

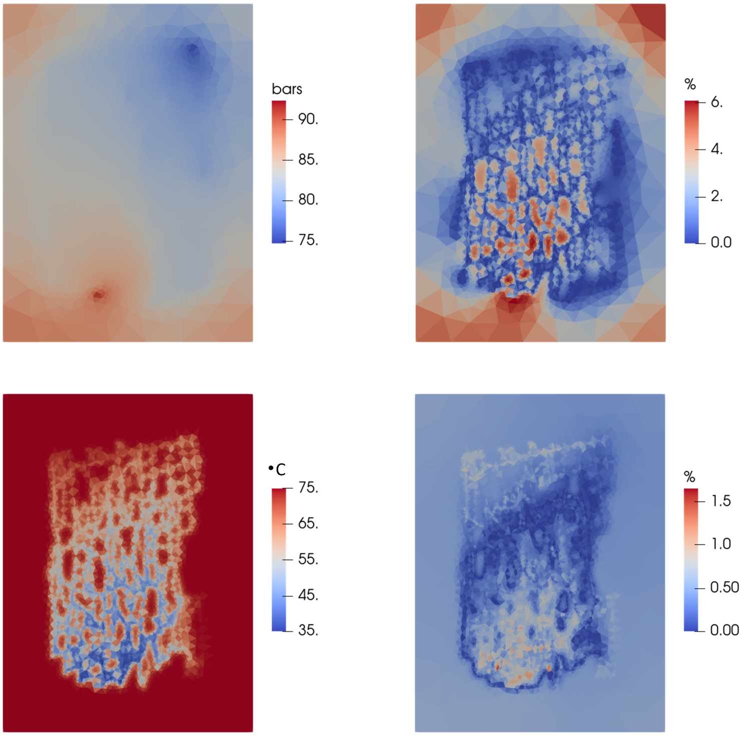

Figure 3.19: Comparison of simulation results after 10 years. Left: pressure (top) and temperature (bottom) profiles of AD-GPRS. Right: relative difference between AD-GPRS and DARTS for pressure (top) and temperature (bottom).

3.4. THREE-DIMENSIONAL CASE

3.4.1. THREE-DIMENSIONAL GEOTHERMAL MODEL

A synthetic geological model is constructed based on typical geology of the WNB [22]. All properties in the model are populated with the dataset from the fluvial Nieuwerkerk Formation of the WNB. The reservoir dimensions are 1.8 km × 1.2 km × 0.1 km as shown in Fig. 3.20. The discretized model contains 60 × 40 × 42 grid blocks. A geothermal well doublet is placed on the middle line parallel to the X-axis with 1 km spacing. The fluvial sandstone is also distributed parallel to the X-axis of the reservoir. Open flow boundary conditions are set along the Y-axis of the reservoir, and no-flow boundary conditions are defined along the X-axis of the reservoir. The top and bottom layers represent overburden and underburden. All of the remaining 40 layers are perforated by both injection and production wells. Two energy-transfer mechanisms - convective and conductive heat flow - are considered in this process.

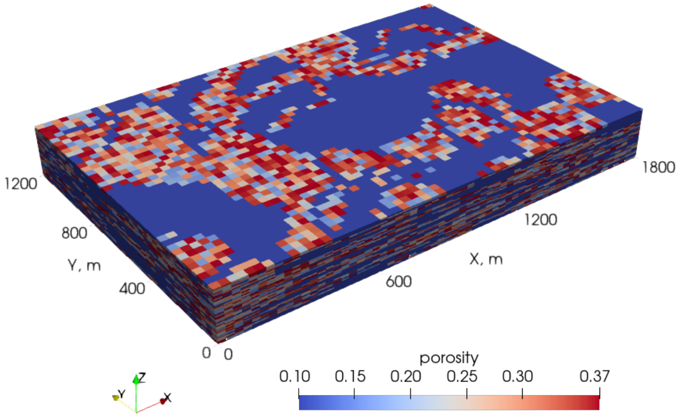

Figure 3.20: Porosity distribution of the synthetic geothermal model. z direction is scaled by a factor of 2.

Because of the complexity of heterogeneous data pre-processing in TOUGH2 and some convergence issues in AD-GPRS at high-enthalpy conditions, this model is only used to compare with AD-GPRS under low-enthalpy conditions. Table 3.7 shows the parameter settings used in the 3D comparison.

Table 3.7: Parameter settings used in 3D benchmark tests.

Parameter	**Value**
Depth, m	1000
Pressure, bars	100
Temperature, K	348.15
Porosity	0.10 ~ 0.37
Permeability, mD	5~ 3360
Sandstone volumetric heat capacity, kJ/m^3/K	2200
Sandstone thermal conductivity, kJ/m/day/K	180
Injection rate, m^3/day	2400
Production rate, m^3/day	2400
Simulation time, years	100

3.4.2. COMPARISON OF SINGLE LAYER SIMULATION

Fig. 3.21 shows the pressure and temperature comparison of the selected 20th layer between DARTS and AD-GPRS after 100 years of simulation. As is displayed, the thermal breakthrough has already been reached for the specified simulation time. A good match ($<2.0\%$) is achieved in the pressure solution and the maximum relative temperature difference is about 2.0%, which can be seen as a close match as well. The distribution of temperature error corresponds to permeability distribution. Higher permeability provides faster fluid flow and sharper temperature fronts causing larger differences.

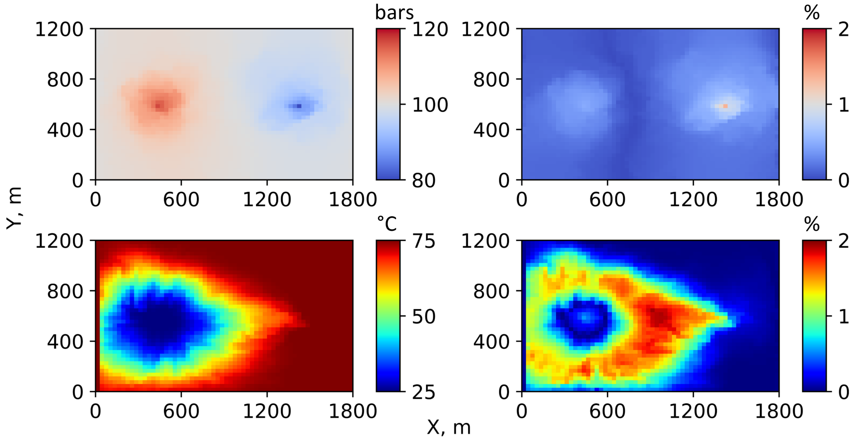

Figure 3.21: Pressure and temperature difference between DARTS and AD-GPRS at the 20^{th} layer. Left: pressure (top) and temperature (bottom) profiles of AD-GPRS. Right: pressure (top) and temperature (bottom) profiles of DARTS-ADGPRS relative difference.

To show the solution difference of each layer between DARTS and AD-GPRS, l_2 norm is taken to calculate the relative difference layer by layer. The normalized difference of k^{th} layer can be evaluated as follows,

$$e^k = \frac{\|\vec{\boldsymbol{x}}_{\boldsymbol{1}}{}^k - \vec{\boldsymbol{x}}_{\boldsymbol{2}}{}^k\|_2}{\|\vec{\boldsymbol{x}}_{\boldsymbol{2}}{}^k\|_2}. \tag{3.1}$$

The pressure and temperature differences are plotted in Fig. 3.22. As is shown, the solution difference of each layer is pretty small (below 1.0%), which indicates a good match is achieved between solutions.

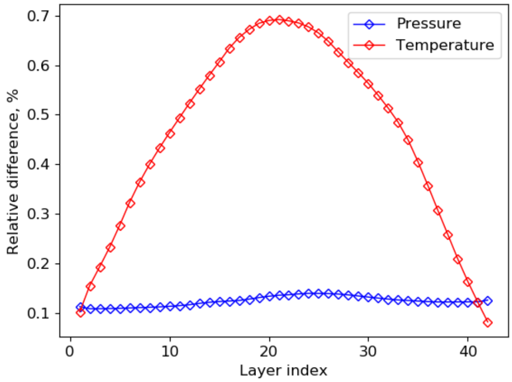

Figure 3.22: Pressure and temperature difference between DARTS and AD-GPRS in each layer of the 3D model.

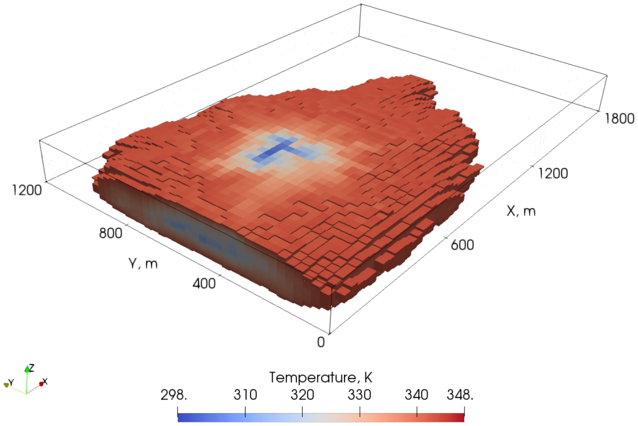

Figure 3.23: Temperature distribution of 3D model below 345 K after 100 years.

3.5. PERFORMANCE COMPARISON

Table 3.8 shows the performance of different simulators on the desktop Intel(R) Xeon(R) CPU 3.50GHz. All runs have been performed in a single thread regime. DARTS provides significantly better performance than TOUGH2 and AD-GPRS. A small timestep of 20 days is required for the high-enthalpy case for robust convergence. Since the timestep strategy in DARTS is different from TOUGH2, there is a slight difference in the total number of timesteps. The fast simulation in DARTS can be attributed to the OBL approach, which significantly simplifies the calculation of state-dependent properties and Jacobian assembly. A slightly higher number of nonlinear iterations in DARTS in comparison to AD-GPRS for low enthalpy cases is related to differences in convergence criteria.

Table 3.8: Comparison of simulation parameters for 100 years among different simulators.

Test case	Simulator	Timestep (day)	No. of Timesteps	Nonlinear iteration	Linear iteration	CPU time (s)
Low-enthalpy one layer model	DARTS	365	115	259	1950	2.9
	TOUGH2	365	115	–	–	24.1
High-enthalpy one layer model	DARTS	20	2020	6834	95032	97.9
	TOUGH2	20	2997	–	–	942.0
Low-enthalpy one layer model	DARTS	365	115	259	1950	2.9
	AD-GPRS	365	115	253	1616	5.5
High-enthalpy one layer model	DARTS	20	2173	10855	125160	126.6
	AD-GPRS	20	2075	9742	159929	475.6
Low-enthalpy fracture model	DARTS	365	38	80	1457	6.4
	AD-GPRS	365	38	87	1416	12.6
Low-enthalpy 3D model	DARTS	365	115	261	2841	159.3
	AD-GPRS	365	115	264	2437	446

3.6. CONCLUSION

The Delft Advanced Research Terra Simulator (DARTS) is used for the prediction of heat production in geothermal projects. A set of benchmark tests were devised and utilized to compare the solutions of DARTS with TOUGH2 and AD-GPRS. Comparison in the 1D horizontal model verifies the capability of DARTS to capture sharp temperature and saturation shocks resulting from the large mobility ratio between saturated steam and liquid water. The convergence analysis of Operator-Based Linearization (OBL) resolution validates the suitability of the OBL approach in simulating nonlinear thermal flow. Besides, it suggests a reasonable resolution in physical space for high-enthalpy simulation with strong non-linearity in physics. 1D vertical models with buoyancy validate DARTS' capability to model a buoyancy-dominated flow in high-enthalpy systems. The phase-potential-upwinding (PPU) strategy was adopted and a close match of the simulation results indicates the reliability of DARTS handling buoyancy-induced flow coupled with phase equilibrium. For the 2D model, the capability of DARTS to simulate planar fluid and heat transport in a heterogeneous fluvial system with different boundary and initial conditions is verified by the close match with both TOUGH2 and AD-GPRS. In addition, the multi-options in well controls (e.g. constant bottom hole pressure, constant rate with constant temperature or enthalpy) integrated in DARTS were checked in these comparisons. Finally, the 3D synthetic geological model comparison displays the ability of DARTS to simulate realistic heterogeneous geothermal fields. The performance comparison among the 3 simulators demonstrates that DARTS allows simulation with a noticeable reduction in CPU time owing to the OBL approach.

4

GEOTHERMAL SIMULATION OF NON-RESERVOIR SHALE FACIES

Summary

Non-reservoir shale facies are often ignored in isothermal simulations because of their low permeability. However, they should be included in geothermal simulations due to their heat recharging effect. In this chapter, efforts are made to find a reasonable upscaling strategy to reduce the additional computational cost related to including shale facies. Local and flow-based upscaling methods are investigated to upscale the shale facies from the fine to a coarser scale. Because of the transient behavior of thermal conduction and the interplay between conduction and convection, the accuracy of the results is found to significantly degrade with the upscaling ratio in either strategy. Therefore, reviewed upscaling methods are not sufficiently accurate for geothermal applications in general scenarios.

This chapter is related to the MSc Thesis "Reservoir Simulation for Play-based Development of Low Enthalpy Geothermal Resources" [54].

4.1. INTRODUCTION

When examining the energy conservation equation in geothermal simulations, heat transfer is governed by two different mechanisms, heat convection and conduction. Due to the high velocity of convective fluid flow compared to the velocity at which heat will travel via conduction, heat convection represents a more efficient way of heat transfer. However, convective flow can only occur where the reservoir rock is porous and permeable. This means in the low-permeability portion of the reservoir the heat conduction is the only heat transfer mechanism. Chapter 5 will show that the heat conduction of impermeable shale facies plays a vital role in delaying thermal breakthrough of a real field. This effect was underestimated before, especially for reservoirs with lower net-to-gross ratio (N/G). It was noted that the shale facies should be characterized in the reservoir model rather than ignored, though introducing the shale facies can result in a computation overhead. The reduction of computation costs when shale facies are included is the motivation for the work presented in this chapter.

One of the standard ways to reduce the number of cells in a model is by upscaling. In this process, multiple cells in the grid are agglomerated to form one larger cell by averaging their property values. Usually, this process is applied across the entire grid; however I just want to do this for the impermeable shale facies. This can be achieved by utilizing the multi-scale upscaling methods, where certain areas of the grid remain at a fine scale and other areas are upscaled. In the following content different multi-scale upscaling methods are examined to upscale shale facies such that the flow of heat is preserved while the number of cells for shale representations is reduced.

4.2. MODELS

A small synthetic fluvial model (the same as Shetty *et al.* [22]) was used for the local and flow-based upscaling. Fig. 4.1 depicts the model used for analysis along with the position of the injection and production wells. The reasons for using this setup rather than a realistic model with complex geological structure are as follows:

- The rectangular shape makes for simpler implementation of upscaling.
- It is favorable for the interpretation of results.
- The model has a low N/G (0.35), in other words, a large portion of shale facies is present. This makes the effect of shale recharge well pronounced.

In the following sections, the local and flow-base upscaling approaches are used to upscale the shale facies.

4.3. LOCAL UPSCALING

With local upscaling methods the properties of a given upscaled cell are calculated independently of the rest of the grid. The advantages of local upscaling are that it is simple and quick to calculate; however, it can be inaccurate. The purpose of utilizing simple methods at the beginning was to check if they were suitable (in which case no further investigation was necessary) and also to identify possible problems related to upscaling for heat flow.

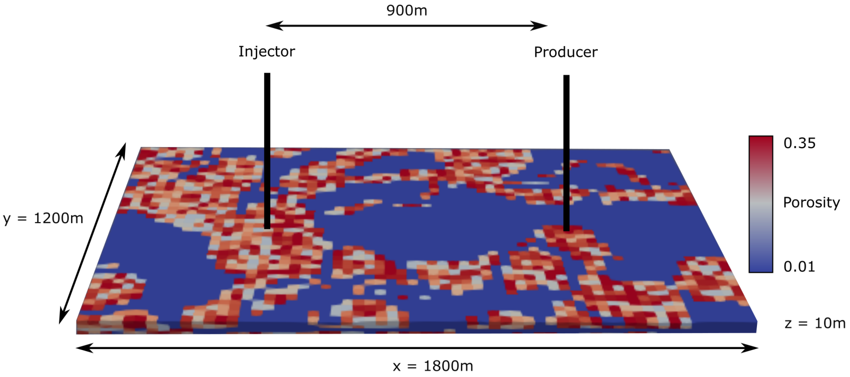

Figure 4.1: Porosity distribution of the synthetic model used for the local and flow-based upscaling experiments taken from Shetty *et al.* [22].

4.3.1. METHOD

The first stage for upscaling is the division of the model into predefined regions to be upscaled. For both local and flow-based upscaling, a coarse Cartesian grid is selected to divide the finer grids into cubic regions with a pre-determined size. Within these regions, the cells representing shale facies will be upscaled into a single cell. Fig. 4.2 shows how the division of the cells into regions has been implemented.

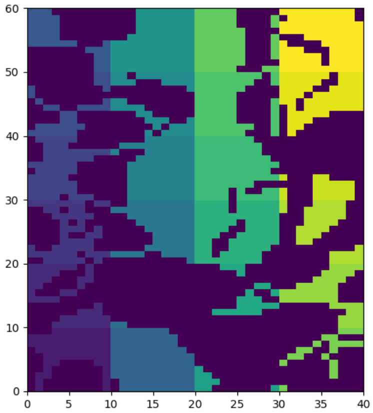

Figure 4.2: Division of one layer of the synthetic reservoir model into blocks of 10x10x2 cells. Reservoir cells (darkest blue) remain unaffected.

With the grid blocks divided into regions for upscaling, the fine-scale cells within this region require agglomeration. Agglomeration of cells for upscaling is done by manipulating connection lists followed by editing cell and connection properties. To demonstrate how connection lists are altered and the cells are re-indexed, a simple example is used. Fig. 4.3 shows a 3x3 grid with its associated connection list.

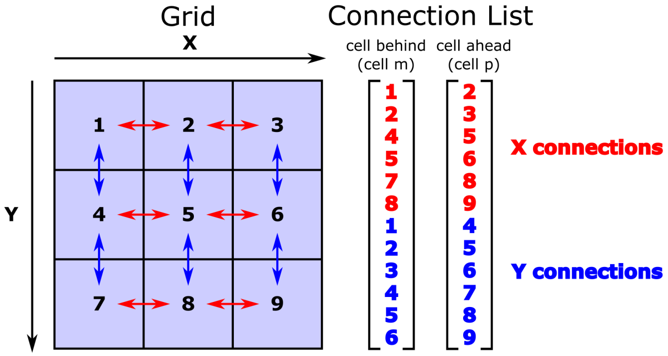

Figure 4.3: A simple 3x3 simulation grid and its connection list.

In this example, the process of upscaling the four cells at the bottom right corner into a single cell is displayed. For manipulation of the connection list, upscaling requires three steps. Firstly, the cells need to be re-indexed to account for the reduced number of cells. Then, connections between the upscaled cells need to be removed from the connection list. Finally, connections between the upscaled cells and the fine cells require updates to account for the change in cell indices. The implementation of these processes is demonstrated in Fig. 4.4.

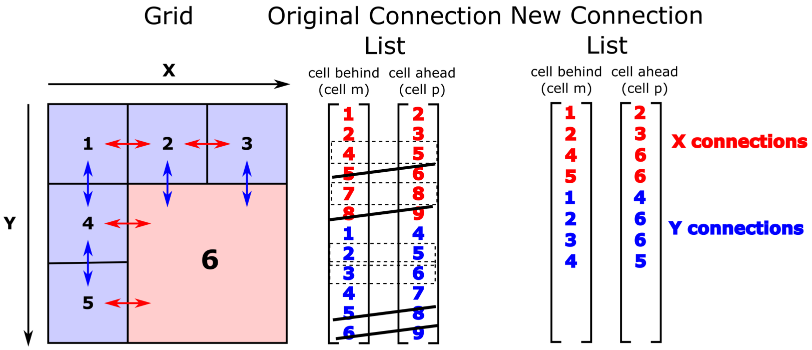

Figure 4.4: Upscaled and re-indexed 3x3 grid with the new connection list. Solid black lines highlight removed connections, dashed lines highlight edited connections.

The porosity, temperature and volume need to be adjusted in terms of upscaling cell properties. The volume upscaling is simple, with the volume of an upscaled cell (V_I) simply being the sum of the volumes of the constituent cells:

$$V_I = \sum_{i \in I} v_i. \tag{4.1}$$

In this case, upscaling is implemented on shale facies, whose porosity is assumed constant and low, and therefore treatment of porosity is not of great importance. Thus, the porosity of the upscaled shale facies has the same value. However, if porosity of shale facies varies and still plays an essential role in the simulation, then a volume averaged porosity (ϕ_I) will be necessary:

$$\phi_I = \frac{1}{V_I} \sum_{i \in I} v_i \phi_i. \tag{4.2}$$

Similarly, if initial temperature varies throughout the reservoir, then a volume averaged temperature (T_I) should be applied:

$$T_I = \frac{1}{V_I} \sum_{i \in I} v_i T_i. \tag{4.3}$$

Finally, the communication of fluid and heat between cells requires the evaluation of hydraulic transmissibility and thermal transmissibility. Upscaling hydraulic transmissibility is simple because the upscaled cells contain shale and are assumed not to contribute to flow. Therefore, the transmissibility of the upscaled cells could just be assigned with a low value.

However, more attention needs to be paid to upscaling the thermal transmissibility. Assuming thermal conductivity across the grid is constant, then thermal transmissibility (Γ_T) is given by:

$$\Gamma_T = \frac{A}{L}, \tag{4.4}$$

where A is the area of the connection between two cells and L is the distance between two cell centres. For the connection between upscaled cells and reservoir cells (with non-shale facies), the area remains unchanged. The distance does change, however, accurately evaluating the length of a connection is difficult as the true centre of the upscaled cell is unknown. For this reason, the thermal transmissibility of these connections is left as it was before upscaling. For the connections between upscaled cells, the area becomes much larger and therefore the value needs to be changed. To approximate the correct thermal transmissibility, the area of all the constituent connections was summed up and divided by the distance between the centres of the large cells (equation 4.5). As mentioned previously, the centre of the upscaled cells does not necessarily represent the centre of the actual shale bodies and therefore this method is only an approximation.

$$\Gamma_T^{IJ} = \frac{\sum_{ij \in IJ} (A_{ij})}{L_{IJ}}. \tag{4.5}$$

4.3.2. EXPERIMENT SUMMARY

Different levels of local upscaling are designed in the experiment and the results are compared to the solution from the fine-grid and ‘no shale facies’ cases. A summary of the experiment is given in Table 4.1. All simulation experiments are run for 150 years with the parameters listed in Table 4.2. The results are displayed in terms of production temperature vs time Fig. 4.5.

Table 4.1: Summary of simulation experiments run for local upscaling.

Simulation Name	**Description**
Full Grid	All cells are active in the fine scaled grid
No shale facies	Only reservoir cells are active
Upscaled - 10	Shale cells are upscaled into regions of 10x10x2 cells
Upscaled - 6	Shale cells are upscaled into regions of 6x6x2 cells
Upscaled - 2	Shale cells are upscaled into regions of 2x2x2 cells

Table 4.2: Simulation parameters for the synthetic reservoir model.

Parameter	**Value**
Grid Size (-)	nx = 60
	ny = 40
	nz = 4
Dimensions (m)	x = 1800
	y = 1200
	z = 10
Well Positions	Injector: i = 15 j = 20
	Producer: i = 45 j = 20
Porosity (-)	Shale: 0.01
	Sandstone: 0.15-0.37
Permeability (mD)	Shale: 0.001
	Sandstone: 6.3-3359.1
Thermal conductivity (kJ/m/day/K)	233.28
Initial reservoir pressure (bar)	200
Initial reservoir temperature (^{o}C)	75
Well control (bar, ^{o}C)	Injector: 220, 30
	Producer:180
Flow at boundary	closed
Simulation runtime (years)	150
Max time step (years)	1

4.3.3. RESULTS AND DISCUSSION

Fig. 4.5 shows that a later thermal breakthrough time for all of the upscaled solutions. Besides, the upscaled solution approaches the fine-scale solution with reducing the size of the upscaled blocks. This can be explained by examining enthalpy maps for the upscaled and non-upscaled cases (in Fig. 4.6). Fig. 4.6a shows that as flow moves past the

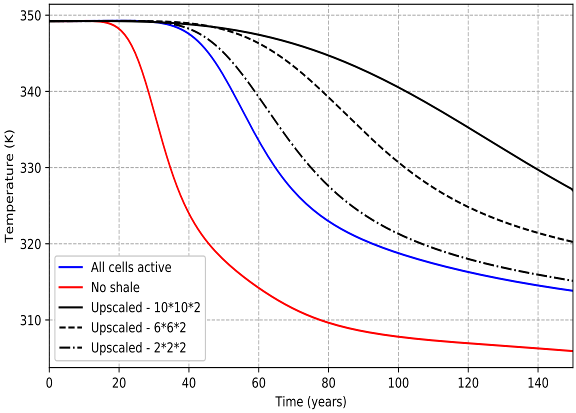

Figure 4.5: Temperature vs time for local upscaling of non-reservoir cells.

reservoir cells, it quickly depletes the adjacent shale cells of their thermal energy. Once these shale cells are depleted, heat conduction from these cells into the injected water will be much lower and heat recharge from further inner shales will not be fast enough to supplement the outer cells. Therefore, the contribution of inner shale in delaying cold front propagation will be very weak. In contrast, Fig. 4.6b displays that large portions of the reservoir have been depleted of thermal energy. The entire upscaled volume can be accessed by the injected cold water in terms of thermal energy. What this means practically is that the upscaled cells can provide far more heat to the reservoir cells given the same thermal transmissibility than the fine cells can in the same time. This observation also explains why the production temperature is closer to that in fine cells as the upscaled regions become smaller, because the grid cells become more similar at the fine scale as the size of the upscaled regions reduces.

The results of the local upscaling demonstrate that simply upscaling the shale cells and leaving thermal transmissibility relatively unchanged result in overly large heat fluxes into the injected water and therefore inaccurate thermal propagation.

4.4. FLOW-BASED UPSCALING

For flow-based upscaling, the thermal flow rate is evaluated by simple simulations run on fine grids to steady state, while the coarse grid thermal transmissibility can then be calculated. Compared to local methods, flow-based upscaling provides much more accurate calculation of the upscaled thermal transmissibility, since the flow rate on fine scale has been obtained. The flow-based upscaling of this study is based loosely on the one used by Karimi-Fard and Durlofsky [55], but adapted for use with temperature rather than pressure.

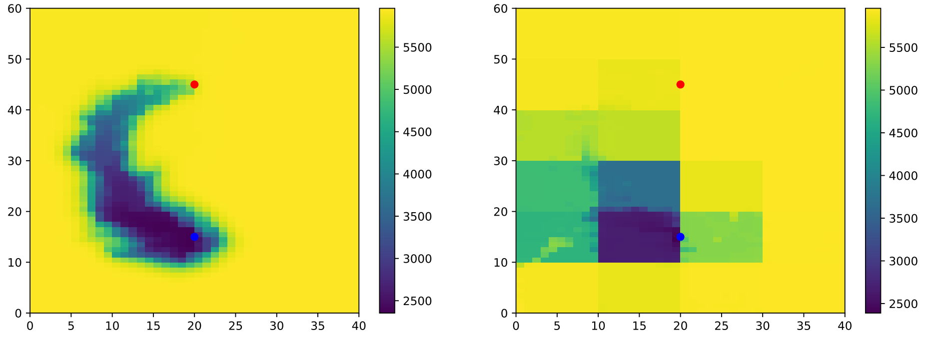

(a) All cells active

(b) Non-reservoir cells upscaled - 10x10x2

Figure 4.6: Enthalpy maps for simulation runs for local upscaling (Experiment 1) at time = 50 years. Injector well = blue, producer well = red

4.4.1. METHOD

At the beginning, a simulation was performed on the fine cells with very high permeability of the sandstone (1x10^6 mD), which leads to almost immediate thermal breakthrough. In this way, the flow path with cold water is surrounded by the shale cells. The conductive heat flow (Q) for all connections in the reservoir could be calculated as:

$$Q_{ij} = \Gamma_T (T_i - T_j). \tag{4.6}$$

With the heat flow Q on the fine grids, the thermal transmissibility of the upscaled cells is re-calculated by matching the Q value. For connections between reservoir and upscaled cells, the thermal transmissibility could be evaluated by Eq. (4.7), while for connections between upscaled cells, the thermal transmissibility could be evaluated by Eq. (4.8).

$$\Gamma_T^{iJ} = \frac{Q_{ij}}{(T_i - \overline{T_J})}, \tag{4.7}$$

where i denotes fine-scale reservoir cells, j denotes fine-scale shale cells, J denotes upscaled cells and $\overline{T_J}$ is the averaged temperature of all shale cells in upscaled cell J.

$$\Gamma_T^{IJ} = \frac{Q_{IJ}}{(\overline{T_I} - \overline{T_J})}, \tag{4.8}$$

where $Q_{IJ} = \sum\limits_{ij \in IJ} Q_{ij}$.

One of the challenges of applying flow-based upscaling to temperature as opposed to pressure is that unlike pressure, a truly steady state cannot be reached. Therefore the heat flux Q and thermal transmissibility are constantly changing with time. The goal is to approximately represent the heat transfer with upscaled effective thermal transmissibility. Fig. 4.7 shows a plot of the average thermal transmissibility for connections between upscaled shale cells and reservoir cells with time. Initially, the thermal transmissibility drops quickly. The thermal transmissibility plateaus towards the end, which indicates the arrival of a semi-steady state phase. The average of all the points on the curve is taken as a reasonable representation of the thermal transmissibility (the black line in Fig. 4.7). Thermal transmissibility curves for the other two upscaling sizes may be found in Fig. 4.10.

Apart from the changed thermal transmissibility, the rest of the upscaling method is very similar to that described in the local upscaling (Section 4.3.1).

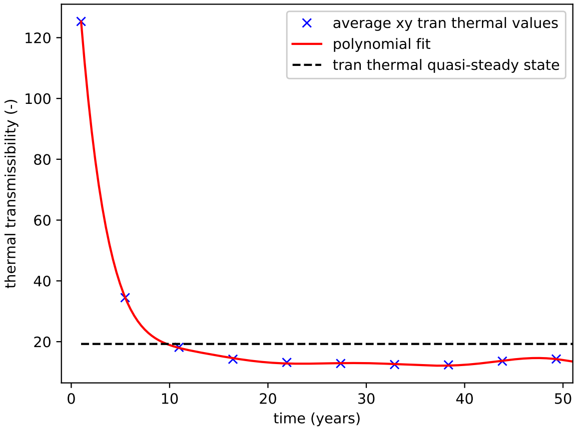

Figure 4.7: Mean thermal transmissibility of reservoir cell - upscaled cell connections vs time for the upscaling into cells of size 6x6x2. The black line represents the average of transmissibility of the red curve.

4.4.2. EXPERIMENT SUMMARY

The model parameters and settings used in flow-based upscaling are exactly the same as those in local upscaling (section 4.3.2), the only difference being the way of the upscaling implemented. Table 4.3 lists the details of the experiment.

Table 4.3: Summary of simulation experiments run for flow-based upscaling.

Simulation Name	**Description**
Full Grid	All cells are active in the fine scaled grid
No shale cells	Only reservoir cells are active
Upscaled - 10	Shale cells are upscaled into regions of 10x10x2 cells
Upscaled - 6	Shale cells are upscaled into regions of 6x6x2 cells
Upscaled - 2	Shale cells are upscaled into regions of 2x2x2 cells

4.4.3. RESULTS AND DISCUSSION

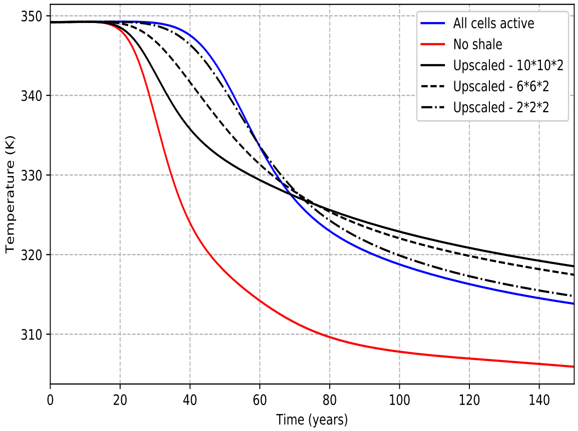

Figure 4.8: Temperature vs time for flow-based upscaling of non-reservoir cells.

The solution with flow-based upscaling (Fig. 4.8) has been significantly improved compared to the solution of local upscaling (Fig. 4.5). The calculated thermal transmissibility with flow-based upscaling characterizes the heat transfer process close to the real results obtained from fine scale. Fig. 4.8 also shows that the accuracy of the production temperature decreases as the upscaled cells become larger, which is due to the assumption of representing the entire thermal transmissibility curve with the averaged value.

The thermal breakthrough of the upscaled solution occurs earlier than that of the fine-scale solution (Fig. 4.9a). This is because the chosen thermal transmissibility values of upscaled cells are initially too low (Fig. 4.9b), this means that heat flux into the injected water is not high enough and therefore the breakthrough occurs more rapidly than in the fine grid solution. The problem is a lot less obvious for the 2x2x2 solution. This is demonstrated in Fig. 4.10, which shows a comparison between the average thermal transmissibility through time curves for both the 10x10x2 and the 2x2x2 upscaling. The average of thermal transmissibility curve for the small upscaled grid (2x2x2) is a much better approximation than that for the large upscaled grid (10x10x2). It would not be a trivial task to resolve the issue related to the coarser-scale resolution, because the error initiates from the assumption of approximate replacement of the fine-scaled values by an averaged one.

4.5. COMPARISON OF THE UPSCALING METHODS

In Sections 4.3 and 4.4, the implementation, results and the mechanism of the upscaling methods are discussed. However, comparison between the results of the two upscaling methods has mostly been qualitative. In this section a detailed quantitative comparison is conducted between the two upscaling solutions and draw conclusions regarding the applicability of the methods. For a quantitative measure of the solution accuracy relative to the fine grid, a normalised root mean square error is used (Eq. (4.9)). This is effectively

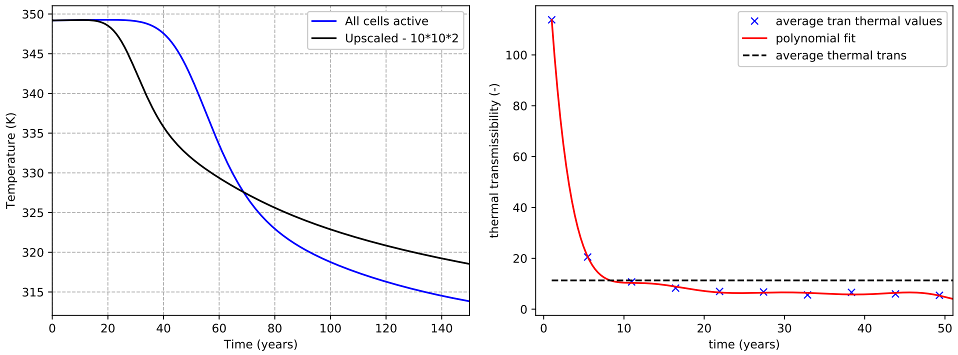

(a) (b)

Figure 4.9: (a) Production temperature vs time of the 10x10x2 upscaled grid and full grid models. (b) Mean thermal transmissibility of reservoir cell - upscaled cell connections vs time for the upscaling into cells of size 10x10x2.

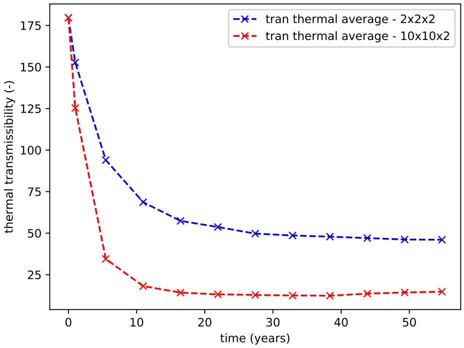

Figure 4.10: Average thermal transmissibility through time for the upscaled cell - reservoir cell connections for the 2x2x2 and the 10x10x2 upscaled grid.

a measure of how close the upscaled solution is to the real solution, with 0 being a perfect match.

$$NRMSE = \frac{\sqrt{\frac{\sum_{i=1}^{N}(y_i - y_i^f)^2}{N}}}{\max(y^f) - \min(y^f)}, \tag{4.9}$$

where: $NRMSE$ = normalised root mean square error, N is the number of data points, y_i is the ith data point of the upscaled solution and y^f is the fine grid solution.

Table 4.4 shows the NRMSE of the upscaled solutions for the major simulation runs. It also shows the approximate number of upscaled cells that are present for the upscaled solutions and the reduction in number of cells achieved via the upscaling. From Table 4.4, it is clear that the only solutions close to the fine-scale solution (low NRMSE), are those from the 2x2x2 flow-based upscaling. Other trends reflected in Table 4.4 are the large rise in error of solution for both flow based and local upscaling as the size of the upscaled cells is increased, and the generally higher errors of the local upscaling.

Table 4.4: Normalised root mean square error and upscaling efficiency for the different upscaling methods.

Simulation	**Normalised root mean squared error**	**Number of upscaled cells (approx)**	**Reduction in number of non-reservoir cells (original number of non-reservoir cells/number of upscaled cells)**
Local - 10x10x2	0.415	48	136.4
Local - 6x6x2	0.253	140	46.8
Local - 2x2x2	0.052	1200	5.5
Flow-based - 10x10x2	0.148	48	136.4
Flow-based - 6x6x2	0.091	140	46.8
Flow-based - 2x2x2	0.026	1200	5.5

Whilst local upscaling is easy to implement computationally and potentially very fast, it should not be used for modelling heat transfer from shale facies due to significant inaccuracies, which become exaggerated as the size of the upscaled body increases. Flow-based upscaling can be used to solve the problem of inaccurate heat transfer, however, very large numbers of upscaled cells are required to make the assumptions used in the flow-based upscaling method valid and the solution accurate.

4.6. CONCLUSION

The conventional approaches for upscaling the shale facies (local and flow-based upscaling) are not sufficient for geothermal applications with realistic heterogeneity. Due to the local transient behaviour of heat conduction, its contribution to heat transfer is closely correlated with the effect of convection. An accurate upscaling strategy should consider the interaction between convection and conduction, which can be characterized by the thermal Peclet number. The magnitude of the Peclet number directly determines the heat transfer dynamics inside the reservoir. In further work, the upscaled parameters (e.g., thermal transmissibility) are suggested to be adaptively adjusted and correlated with the Peclet number to accurately represent the heat transfer in geothermal applications.

5

MODELING LOW-ENTHALPY GEOTHERMAL DEVELOPMENT AT GEOLOGICAL SCALE

Summary

A realistic low-enthalpy geothermal reservoir based on real data with high detail and complicated sedimentary structure is utilized to perform a sensitivity analysis. The compelling numerical performance of DARTS makes it a suitable tool for a large ensemble of models including efficient sensitivity analysis. The major finding of this chapter is that shale facies, generally ignored in hydrocarbon reservoir simulations, can significantly extend the predicted lifetime of geothermal reservoirs. It is important to accurately account for the shale facies in the simulation though with an additional computation overhead. The overburden layers can improve doublet performance, but the impact depends on reservoir heterogeneity. In addition, heterogeneity will also divert the flow path even with only a minor shift in the well placement. The discharge rate, an essence of operation strategy, inversely corresponds to the doublet lifetime but positively correlates with the energy production for the studied ranges. Low sensitivity of doublet lifetime to the vertical-horizontal permeability ratio and porosity-permeability correlation is observed. All these systematic findings for a realistic geothermal field with uniquely detailed characterization can help to provide a general guideline for forward simulation and further improve the profitability of geothermal energy production through computer-assisted modeling and optimization.

The material presented in this chapter has been submitted to a journal.

5.1. INTRODUCTION

Although geothermal energy is an attractive technology, the uncertainty in size and properties of geothermal reservoirs will directly impact the technical and economic feasibility of geothermal projects. The doublet lifetime and heat recovery rate [56] often vary a lot with both reservoir parameters and operational management.

In general, the shale layers are taken as barriers for convective flow due to their low permeability. They are usually neglected in isothermal simulation to improve computational efficiency with the reduced model. However, in geothermal reservoirs, the heat transport occurs by both convection and conduction forces. Though negligible convective flow happens in shale, the shale facies stores a large amount of energy, which can behave as a heat buffer for the permeable sandstone through heat conduction. With process-based realizations, Crooijmans *et al.* [57] found the shale facies plays an important role for doublet performance when the net-to-gross ratio is less than 50%. However, the utilized process-based realization was not constrained to any measured data and based on purely conceptual estimation of reservoir parameters. For realistic reservoirs, the accurate characterization of facies distribution needs detailed geological information constrained to the measurements (e.g., log and core data). It is essential to investigate the charging effect of shale facies to high-permeable regions with enough geological accuracy to achieve optimal project management.

The overburden and underburden layers usually perform the role of sealing a reservoir and confine the leakage of fluids [58]. In addition, these layers can also provide thermal recharge through heat conduction in a geothermal reservoir [59]. Though the permeability confines the convective flow in burden layers, the energy they contain matters. However, contradictory conclusions on the impact of burden layers exist in the literature. Willems *et al.* [19] found the overburden and underburden layers have a positive impact on heat production through charging the target aquifer. However, this finding is based on a simplified homogeneous model. As shown in Shetty *et al.* [22], the overburden and underburden layers do not play a significant role to doublet performance in synthetic process-based heterogeneous models. In reality, reservoir heterogeneity is ubiquitous in subsurface systems [60–62]. It will determine the direction of convective flow, which can vary the influence of burden layers. A conclusive evaluation of the role of confined layers in realistic geothermal reservoirs constrained to measurements is necessary for optimal modeling.

The reasonable operational strategy is also essential for the success of a geothermal project. For example, the discharge rate will directly impact the thermal propagation and energy output [63]. Saeid *et al.* [64] found higher discharge rate will result in shorter doublet lifetime, sharper thermal front and less energy extraction. In addition, the well interference in a multi-well system can influence doublet lifetime by changing the development of the cold water plume. To maximize the doublet lifetime, the optimized doublet configuration and well spacing are generally needed [19, 65]. Furthermore, Shetty *et al.* [22] concluded a large variation (up to 50%) of lifetime can be achieved by a small variation (less than 50 m) in doublet location after a set of systematic study on the influence of doublet position to project lifetime. Again, these findings are based on either conceptual or synthetic models. There is special interest in the investigation of flow rate and well placement to doublet performance in the realistic reservoirs. A well-designed operational scheme will minimize harmful effects such as well interference or early thermal breakthrough, and maximize the economic benefits (e.g., higher NPV or faster energy production).

5.2. MODEL DESCRIPTION

The research area is located in WNB, where the sediments range in age from Jurassic to recent time and are overlying Triassic and older sediments. The Upper Jurassic and Lower Cretaceous start with the continental sediments of the Nieuwerkerk Formation. These sediments were deposited in subsiding half-grabens, while adjacent highs were subjected to erosion. In the Nieuwerkerk Formation, the Delft Sandstone has in general good reservoir properties [19, 56, 65].

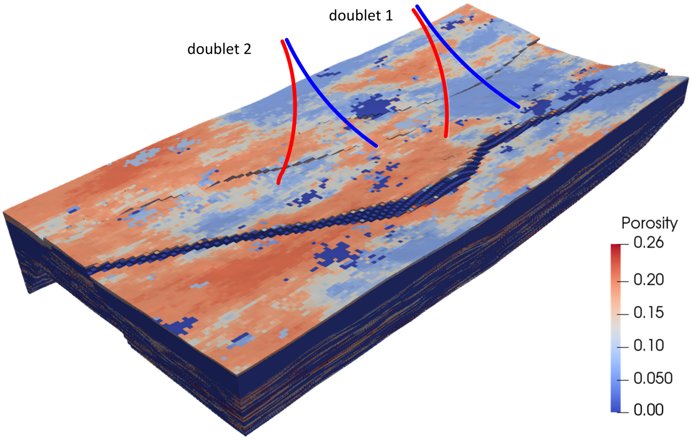

Figure 5.1: Porosity distribution of the target geothermal reservoir. In both doublets, the injection wells are shown by blue and the production wells by red. The well trajectories are connecting the following blocks in top and bottom layers respectively: I1 (51, 58) - (48, 50); P1 (76, 53) - (82, 49); I2 (94, 44) - (111, 37); P2 (124, 39) - (144, 30).

“The Delft Sandstone is interpreted to be deposited as stacked distributary-channel deposits in a lower coastal plain setting resulting in massive sandstone sequences."[66] The thickness of the Delft Sandstone is influenced by the syn-rift deposition of the sediments and therefore it is of variable width with a thickness up to 130 m. The sandstone consists of fine- to coarse-grained sand bodies, and their lateral continuity is difficult to predict. The Berkel Sandstone Member and Berkel Sands-Claystone Member have a shallow marine depositional setting. The facies range from upper shoreface to lower shoreface of a coastal-barrier system. Fig. 5.1 and Fig. 5.2 show the modelled porosity distribution of the target reservoir.

In favour of the detailed exploration and recordings of the geological statistics, higher-fidelity data interpretation and geological modeling are enabled for the target reservoir in comparison with the typical low-enthalpy geothermal reservoirs. Furthermore, based on completeness of the fundamental data sets, it will be much easier to implement different realizations for sensitivity analysis in DARTS, which can be observed in the following investigations.

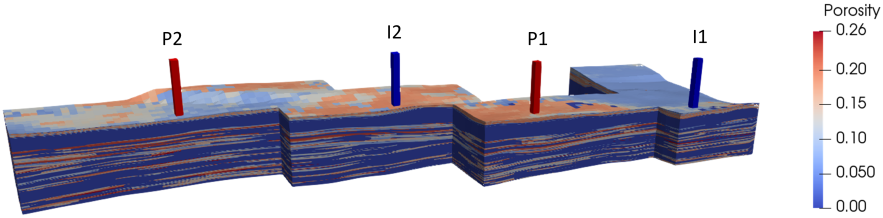

Figure 5.2: Porosity distribution in the target geothermal reservoir from a cross section view to show the connectivity and payzone between injection and production wells of the doublets.

The model extends horizontally by 9000 m × 4200 m. Two doublets placed in the reservoir are operated with a constant rate control. Since it is difficult to predict the lateral continuity, the reservoir boundary condition is defined as no-flow. Table 5.1 provides the parameter settings for the base case. As is shown, a permeability contrast five orders of magnitude is present in the reservoir. With the water cycling in the system, I try to observe the evolution of the thermal plume in the reservoir and production temperature of both doublets by varying reservoir parameters and operational schemes. The project lifetime in this study has been defined as a drop of the production temperature to 335 K.

Table 5.1: Parameter settings for base case.

Parameter	**Value**
Depth, m	1117 ~ 1965
Pressure, bar	200
Temperature, K	348.15
Porosity	10^{-5} ~ 0.256
Permeability, mD	0.004 ~ 1308
Shale volumetric heat capacity, kJ/m^3/K	2300
Sand volumetric heat capacity, kJ/m^3/K	2450
Shale thermal conductivity, kJ/m/day/K	190
Sand thermal conductivity, kJ/m/day/K	260
$\phi - k$ correlation	Model 1
Rate (doublet 1), m^3/day	7500
Rate (doublet 2), m^3/day	10000

5.3. THERMAL RECHARGE EFFECT OF IMPERMEABLE FACIES

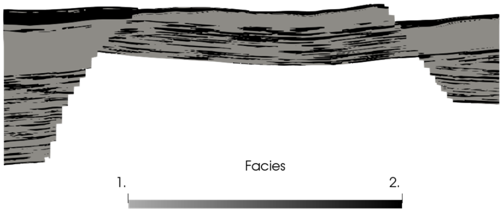

Figure 5.3: Facies distribution of the target geothermal reservoir from cross section view - (1: shale, 2: sandstone).

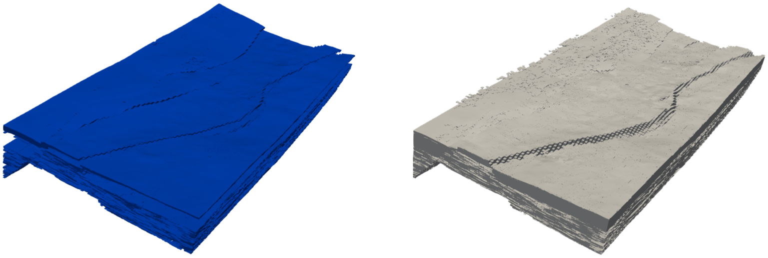

(a) sandstone

(b) shale

Figure 5.4: Overview of the facies distribution in the reservoir. The number of grid cells utilized to depict shale facies (b) is circa 3 times of that of sandstone facies (a), which reflects a higher volume of shale facies is contained in the reservoir than the sandstone facies.

The model includes intersecting sandstone and shale facies. The facies distribution (Fig. 5.3) corresponds to circa 0.8 million grid blocks for the sandstone (Fig. 5.4a) and 2.4 million blocks for shale facies (Fig. 5.4b). To evaluate the impact of the shales on thermal breakthrough, two scenarios are simulated: including and excluding the shale grid blocks. The production temperature of each doublet is depicted in Fig. 5.5.

The presence of the shale layers in the simulation allows the use of higher discharge rates that result in higher energy production for an equivalent system lifetime. The lifetime of both doublets is significantly extended when the shale layers are included in the model. As the injected cold water transports through the sandstone layers, it is reheated, extracting energy from the sandstone layers. As time evolves, a temperature gradient is built up between the sandstone bodies and the neighboring shale layers with the shales providing thermal recharge by heat conduction. The spatial intercalation of the sandstone and shale facies increases the contact area between them and amplifies the effect of the thermal recharge.

A considerable difference in the shape of the thermal plume is evident with and without shale layers (Fig. 5.6). The cold front propagation is more restricted due to the con-

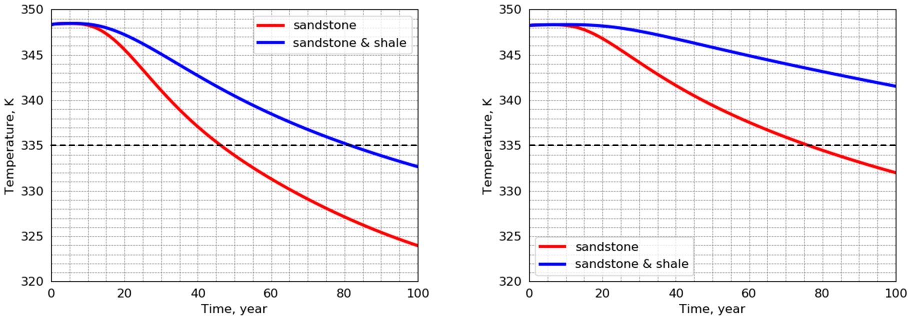

(a) P1 (b) P2

Figure 5.5: Production temperature of each doublet with and without shale layers. Here P1 is the production well of doublet 1, P2 is the production well of doublet 2.

ductive thermal recharge when the shales are included. The difference in the shape of the thermal plume becomes more pronounced with longer simulation time. This demonstrates the importance of geothermal modeling at sufficient geological resolution.

5.4. PARAMETER SENSITIVITY ANALYSIS

The overburden layer is originally not included in the geological model, therefore its impact is not contained in the base case. In addition, due to the subsurface uncertainty the permeability can be interpreted by different correlations with porosity. At the same time, the permeability ratio between vertical and horizontal directions is also a sensitive factor for fluid flow between layers. As for the operational sensitivities, the impact of well placement and discharge rate to heat production is worth examining.

5.4.1. OVERBURDEN

To investigate the impact of the overburden layer on the target reservoir, a ghost impermeable layer is placed on top of the reservoir to mimic the overburden layer. The underburden layer is contained in the geological model, therefore its influence is inherent and not considered as a factor here. No convective flow is assumed inside the overburden layer because of its low permeability. The overburden affects the thermal recharge in the reservoir only through heat conduction. The production temperature of each doublet in presence and absence of the overburden layer is shown in Fig. 5.7.

The lifetime of two doublets displays different sensitivity to inclusion of the overburden layer: the lifetime of doublet 1 is extended (Fig. 5.7a) while the lifetime of doublet 2 is not impacted at all (Fig. 5.7b). The reservoir heterogeneity plays an essential role to the extent that overburden layers can take effect. The high-permeability region around the production well of doublet 1 in the top layers (see Fig. 5.2) benefits the thermal recharge of overburden to the cold front. With cold front propagation, the temperature difference is built up between the overburden and permeable layers. Since heat conduction is pro-

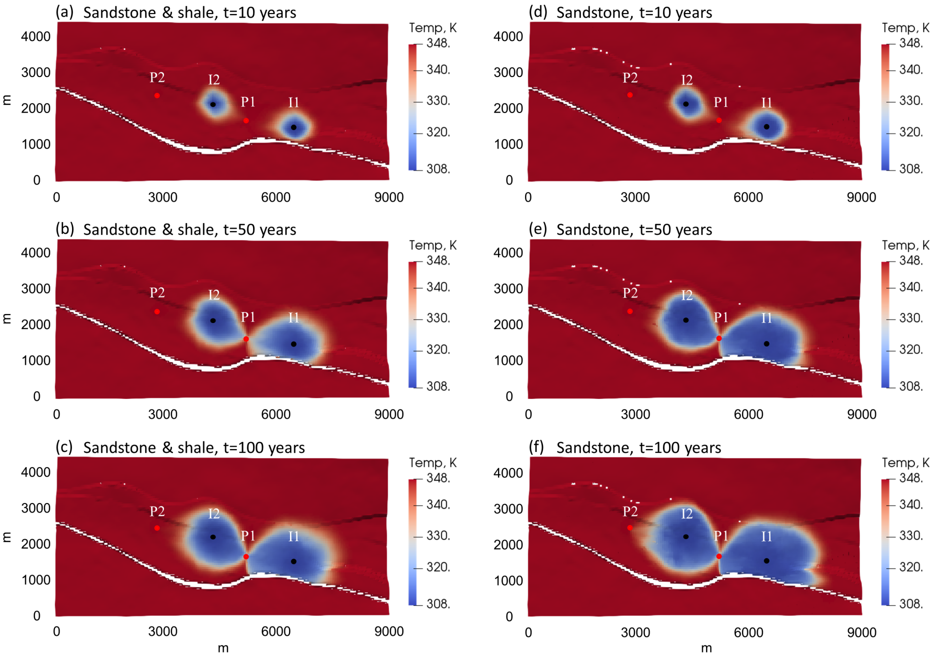

Figure 5.6: Thermal plume propagation inside the reservoir (a slice along horizontal direction) with (left column) and without (right column) shale layers at different development time: 10, 50 and 100 years. The production wells are marked by red dots while the injection wells by black dots.

portional to the temperature gradient and contact area, the impact of heat conduction to heat propagation increases during the development process. The heat conduction of the overburden layer recharges the cold water and delays the thermal breakthrough on the top layers. Therefore, compared to the case without overburden, the lifetime is extended.

Doublet 2 mainly targets the Delft Sandstone (bottom reservoir layers). The production well of doublet 2 does not pass highly permeable layers on top of the reservoir, as is displayed in Fig. 5.2. Therefore, the thermal recharge from the overburden layer does not affect thermal breakthrough of doublet 2. Notice that these conclusions can only be made based on detailed modeling of a geothermal field.

5.4.2. WELL PLACEMENT

The local changes in placement of the well can impact the flow path and sweep area of the doublet, consequently influencing doublet performance and lifetime. Shetty *et al.* [22] has already examined the impact of the well location on the production temperature of a doublet based on a synthetic geological model and found a large variation of lifetime with such changes. As shown in Shetty *et al.* [22], the fluid streamlines and flow path can

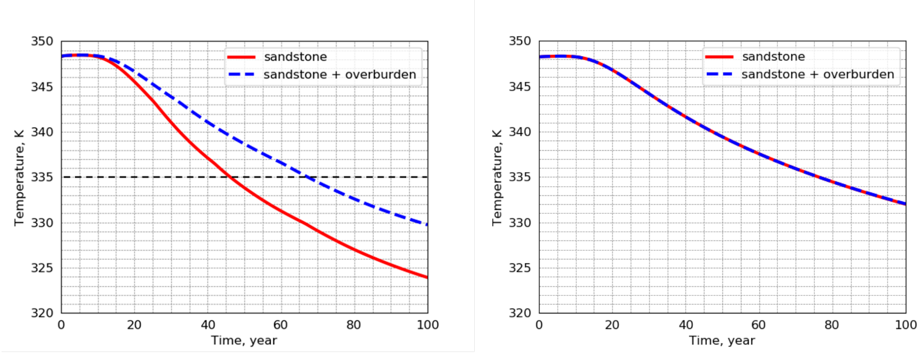

(a) P1

(b) P2

Figure 5.7: Production temperature of each doublet with and without overburden layer. Here P1 is the production well of doublet 1, P2 is the production well of doublet 2.

change significantly, although the doublet was only re-located locally (less than 50 m) around the reference position. In this section, I follow a similar workflow and investigate the influence of the well placement on lifetime of the realistic geothermal reservoir.

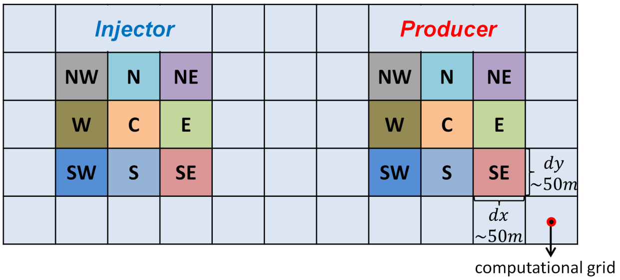

Figure 5.8: Schematic for the selected doublet positions in this section. The cells marker by 'C' denotes the reference position of the wells. These cells represent the computational grids used to describe the reservoir and run the simulations. The grid sizes along x and y directions are around 50 m.

The schematic for well placement is depicted in Fig. 5.8. Besides the reference locations, neighboring grid cells are also considered as the possible doublet locations, which corresponds to approximate 50 m variation in space. In each sensitivity study, both wells of one doublet are simultaneously moved in the lateral direction. For each simulation, only the position of one doublet is changed, while the other doublet remains at its initial location. The simulation results are displayed in Fig. 5.9 for each doublet.

As shown in Fig. 5.9, the well location can significantly influence the doublet lifetime of the geothermal reservoir. For doublet 1 (Fig. 5.9a), the lower and upper limits of doublet lifetime are reached at the South (S) and the North-East (NE) locations respectively. The well location selected at the North-East can extend the doublet lifetime for around 10 years compared to the South position which is around 20% variation of the lifetime.

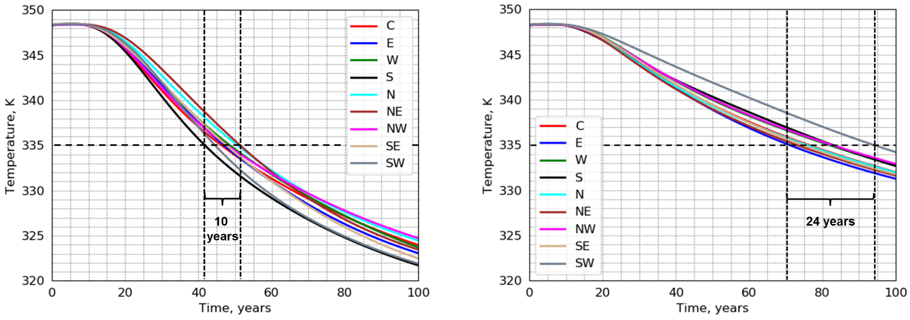

(a) P1

(b) P2

Figure 5.9: Production temperature of each doublet for different doublet positions. Here P1 is the production well of doublet 1, P2 is the production well of doublet 2.

For doublet 2 (Fig. 5.9b), the lower and upper limits of doublet lifetime are achieved at the East (E) and the South-West (SW) locations respectively. Approximately 24 years of lifetime of the doublet can be gained additionally when its location is changed from the worst to the best case (only by circa 50 m) which is more than 25% variation.

This confirms the conclusion of Shetty *et al.* [22], which was just based on a conceptual geological model. The finding demonstrates the necessity to perform uncertainty analysis based on the existing geological knowledge and therefore, reduce the risk of earlier thermal breakthrough and robustly optimize the heat recovery of geothermal fields.

5.4.3. DISCHARGE RATE

The development scheme directly impacts the lifetime and heat production of a geothermal reservoir. In addition, heat production can also be impacted by doublet interference. In this study, both doublets are operated with flow rate control, which is the operation scheme usually applied in practice. Here, only the injection and production rate of doublet 1 are tuned while the production temperature and energy production of both doublets are recorded to evaluate heat production from doublet 1 and its interference to doublet 2.

The production temperature of doublet 1 varies a lot with the rate changes (Fig. 5.10a). A shorter doublet lifetime is observed with the increase of discharge rate, which is because larger discharge rate accelerates the propagation of the cold front and yields an earlier thermal breakthrough. The lifetime of doublet 1 is extended by 43 years with a 3 times reduction in injection and production rate. It is obvious that the lower rate gives slower propagation of the cold front and elongates the lifetime. However, Fig. 5.10b shows that the total energy production decreases with the rate reduction, although the lifetime is extended which is happening due to a reduction in swept region of the reservoir.

Notice that the input energy needed to maintain a higher production rate is also expected to be larger. The required pressure differences for these 3 production schemes are 22.4, 44.7 and 67.2 bars separately for production rates varying from 2500 m^3/d to

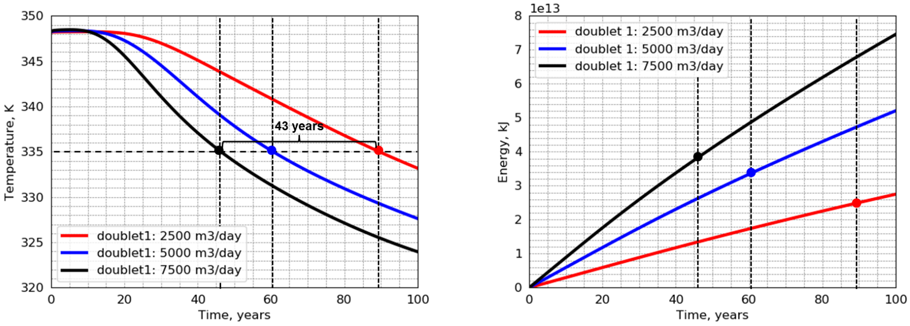

(a) (b)

Figure 5.10: Production temperature (a) and cumulative energy production (b) of doublet 1 under different discharge rates of doublet 1.

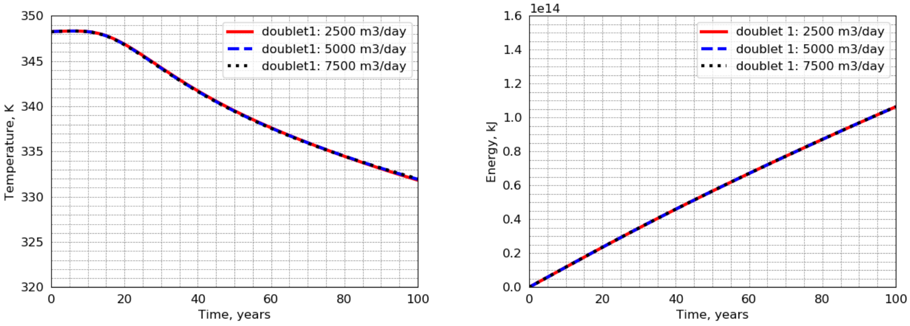

(a) (b)

Figure 5.11: Production temperature (a) and cumulative energy production (b) of doublet 2 for different discharge rates of doublet 1.

7500 m^3/d. A quick evaluation of the required pump energy can be expressed as the function of pressure difference (ΔP) and discharge rate (Q):

$$P_{pump} = \frac{\Delta P \cdot Q}{\eta} \tag{5.1}$$

where η denotes the pump efficiency. Detailed economical analysis (including factors related to NPV) is hence required before a final decision about the preferred discharge rate can be made [67–69].

The production temperature of doublet 2 (Fig. 5.11a) does not change with the variation in the rate of doublet 1, which demonstrates that doublet 2 is not interfered by doublet 1. The energy production in Fig. 5.11b also states that doublet 2 is not influenced by varying the rate of doublet 1. This is an important observation for a typical sedimentary environment of low-enthalpy geothermal systems.

5.4.4. VERTICAL-HORIZONTAL PERMEABILITY RATIO

The permeability ratio between vertical and horizontal directions varies with the geological and sedimentary process and can influence the direction of fluid flow among layers, which in turn influences the thermal propagation in the geothermal reservoir. In this section, the influence of vertical and horizontal permeability ratio to production temperature is investigated. Three permeability ratios are selected: $k_v/k_h = 0.01$, 0.1 and 1 which indicates changes in vertical permeability while horizontal permeability remain fixed. The production temperature of both doublets is depicted in Fig. 5.12.

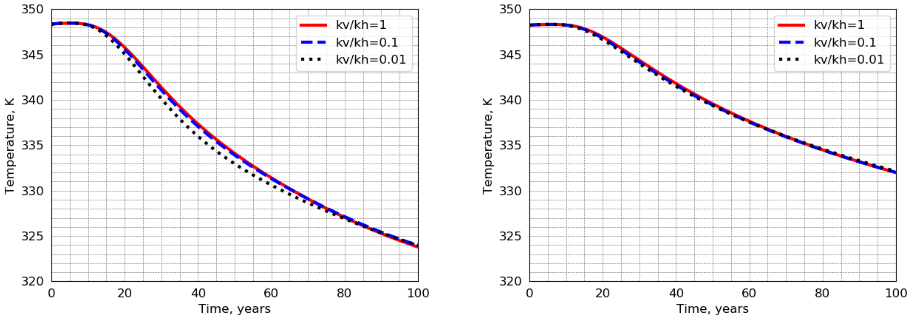

(a) P1

(b) P2

Figure 5.12: Production temperature of each doublet for different k_v/k_h values. Here P1 is the production well of doublet 1, P2 is the production well of doublet 2.

The lifetime of doublet 1 is slightly influenced by the permeability ratio (Fig. 5.12a). With the increase in permeability ratio, the lifetime is slightly extended, which means more heat is swept. On the other hand, the inter-layer communications are reduced and the diversion of flow between layers is restricted under lower permeability ratio. Therefore, a higher permeability ratio will lead to earlier thermal breakthrough and the total heat sweep efficiency of the reservoir decreases.

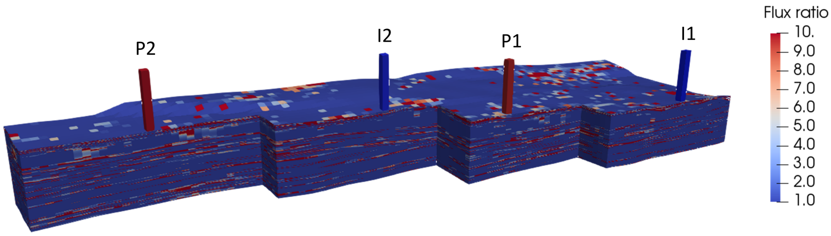

Figure 5.13: The flux ratio between x and z directions of each grid block under vertical-horizontal permeability ratio of 1 at 100 years.

In Fig. 5.12b, the lifetime of doublet 2 seems insensitive to the permeability ratio. Due to the complexity of geological formation in the reservoir, this doublet may be drilled through multiple impermeable layers, which already separate the fluid and heat flow in the vertical direction as barriers. Therefore, even if the permeability ratio is adjusted for different simulation runs, the influence of permeability ratio to flow does not take effect. In addition, the flow along the horizontal (x) direction is much larger than that along the vertical (z) direction for permeable sandstone layers (Fig. 5.13). When a smaller vertical-horizontal permeability ratio is selected, the connectivity in vertical direction will become worse, which will give rise to even weaker flow between inter-layers. Therefore, the variation of permeability ratio does not significantly impact the production temperature even when high-resolution geological realism is involved in the model.

5.4.5. POROSITY-PERMEABILITY CORRELATION

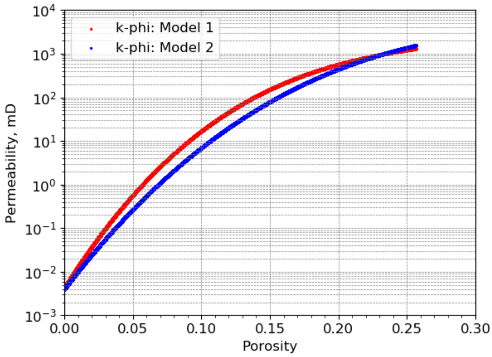

Figure 5.14: Porosity-permeability correlations generated from TNO-AGE [70].

The porosity-permeability correlation is another source of uncertainty in the geothermal reservoir. Here, two different porosity-permeability ($\phi - k$) relations (Fig. 5.14) are used based on the correlations from TNO-AGE [70] for the typical sandstones of WNB.

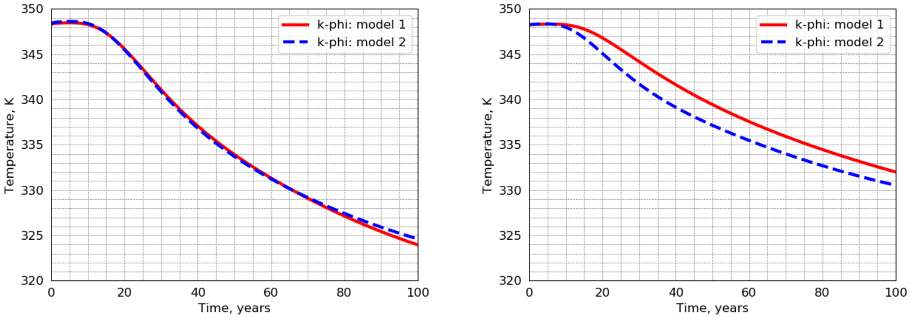

(a) P1

(b) P2

Figure 5.15: Production temperature of each doublet under different $\phi - k$ correlations. Here P1 is the production well of doublet 1, P2 is the production well of doublet 2.

As displayed in Fig. 5.15a, the production temperature of doublet 1 is only minimally affected by the change of correlation. As doublet 1 mainly targets at the top Berkel Sandstone, the preferential channels inside the control area of doublet 1 are associated with high porosity (Fig. 5.2). Two $\phi - k$ correlations generate similar permeability distribution in the high porosity values which is quite typical for sandstones. Therefore, the convective flow of doublet 1 only slightly varies between the two correlations.

However, a more pronounced difference is observed in the production temperature of doublet 2 (in Fig. 5.15b) where the lifetime is noticeably extended with correlation 1. This can be explained by the existence of an evenly distributed permeability field within the control area of doublet 2. With correlation 1, the number of flow paths in doublet 2 is increased with improved $\phi - k$ correlation (compared to correlation 2). In this scenario, the injected cold water sweeps a larger area of the reservoir and the thermal breakthrough is delayed. This difference can only be observed with modeling at high-resolution geological scale.

5.5. CONCLUSION

An extensive investigation is performed based on a realistic heterogeneous reservoir model at geological-scale resolution. Above all, shale facies play a strikingly important role to accurately evaluate the energy production. The thermal front propagation in the realistic reservoir is significantly delayed by the conductive recharge from the shale facies, which has not been studied and discussed in detail from the existing researches. The impact of overburden layers to doublet performance strongly depends on the local reservoir heterogeneity. A large extension in doublet lifetime (e.g., 20 years) is detected when overburden layers recharge their adjacent permeable region while almost no impact is observed in another location within the same reservoir. Without detailed reservoir characterization and accurate forward simulations investigation similar to this study, it is difficult to quantitatively estimate the impact of overburden layers. Besides, heterogeneity will also deviate the flow path in the system with a minor shift in well placement, consequently obvious variations are observed. Increasing the discharge rate will accelerate the thermal breakthrough, but the cumulative energy production is correspondingly enlarged within the realistic reservoir due to a better energy sweep efficiency. This demonstrates that solely pursuing a longer lifetime is not an optimal choice in realistic practice, which is different from the conclusions drawn from synthetic or conceptual models. Though the vertical-horizontal permeability ratio and porosity-permeability correlation display relatively weak influence on the lifetime of the project, these fundamental parameters are essential and worth to verify in reality. Detailed sensitivity analysis in this work provides insights towards full uncertainty quantification required for meaningful optimization of geothermal development.

6

UNCERTAINTY QUANTIFICATION OF LOW-ENTHALPY GEOTHERMAL DEVELOPMENTS

Summary

The efficient development of a geothermal field can be largely affected by the geological, physical, operational and economic uncertainties. Systematic uncertainty quantification involving these parameters helps to determine the probability of reaching the economic targets (e.g., energy production, Net Present Value (NPV), etc.). In this chapter, the geological model in Chapter 5 is utilized. Taking all uncertain parameters (e.g., porosity-permeability realization, salinity, heat price, etc.) into consideration, the input data set is sampled within predefined distributions or ranges using the Monte Carlo method. Ensembles of forward simulations are powered by the GPU version of DARTS, which has been proven to provide high computational performance with the studied model. The uncertainty of energy production and NPV with different parameters is comprehensively investigated. The observed uncertainty inside the complex subsurface system could never be unveiled without such a detailed quantification.

The material presented in this chapter has been published in the Proceedings of World Geothermal Congress, Reykjavik (Iceland), 2020 [71].

6.1. INTRODUCTION

The management of energy applications related to subsurface resources should consider the inherent geological and physical uncertain parameters at sufficient level. The developing strategies of subsurface systems can be adjusted after consideration of uncertainties, which have been shown in various industrial applications [72–75]. Without exceptions, the energy production from geothermal reservoirs can be easily perturbed by the uncertainties as well. As a consequence, the profitability of a project will be changed because of the uncertain operational and economic parameters.

Limited by geological measurements and samples, our knowledge about a target reservoir is generally based on data interpretation and empirical correlations. For example, the relationship between permeability and porosity is often based on empirical petrophysical correlations, while the porosity values are often interpreted from core analysis and log curves. However, the spatial distribution of permeability and porosity is highly uncertain. Besides, the physical and thermal properties of fluids (e.g., salinity, density) and rock (e.g, thermal capacity and conductivity) can vary with mineral dissolution and rock composition at geological time scales. These variations impact the amount of energy and heat transport processes in the reservoir. In addition, the operations of a geothermal reservoir should take the economic part into account, which directly determines the project success. However, the economic parameters (e.g., heat and electricity prices) will fluctuate with the markets, which introduce uncertainties in the comprehensive appraisal of a geothermal project.

Quantifying the influence of uncertain key parameters in advance will assist reservoir management and improve the developing schemes in time. One advantage of numerical simulations is that the reservoir response to the presence of various uncertainties during development can be inspected with ensembles of forward simulations. Monte Carlo Simulation (MCS) has been widely used to quantify the uncertainties in subsurface applications [73, 76–78]. MCS performs simulations with random input data in the parameter space. How representative MCS simulation results are depends on the dimension of the uncertain parameter space and the nonlinearity of the underlying model. To achieve converging results, MCS usually performs a large number of forward simulations, which requires a high-performance numerical simulation framework and abundant computation resources, especially for large models with detailed geological characterization.

A popular treatment to mitigate the computational challenges for larger models is property upscaling. Restricted by the computational resources, the simulation models are often compromised with coarse resolutions by efficient upscaling-based approaches [79, 80] in isothermal simulations. However, the heat transport in geothermal systems is governed by the interplay of thermal convection and conduction. The generally-ignored or coarsely-upscaled entities (e.g., shale facies) in isothermal simulation should be carefully dealt with in geothermal systems. To the best of our knowledge, it is still an open question how to effectively upscale the non-reservoir lithologies in geothermal simulations (as described in Chapter 4 and [54]). Consequently, the demanding computational workload of large models (e.g., with millions of grid blocks) remains a challenge for conventional reservoir simulators.

With the development of GPU computing architecture, high-performance computation reduces the time required for the laborious simulations to an affordable time. The recent implementation of GPU and multithread CPU versions of DARTS [44, 45] have largely improved the simulation performance. A benchmark study [45] demonstrates that the geothermal simulation with DARTS on GPU achieves an order of magnitude faster speed than a single thread CPU simulation.

In this chapter, systematic uncertainty quantification is performed for a real geothermal reservoir with detailed reservoir characterizations. MCS is selected to investigate the uncertainty of energy production and Net Present Value (NPV) with multiple concerned parameters. The large ensembles of forward simulations are executed on the GPU version of DARTS. In the following sections, the geological, numerical and economic models are first introduced, followed by a description of input parameters for investigated uncertain parameters. After a series of forward simulations, a convergence study is performed to examine the MCS convergence. Then, a detailed uncertainty analysis is presented based on the numerical results, followed by conclusions.

6.2. MODEL DESCRIPTION

6.2.1. GEOLOGICAL MODEL

The geological model in this chapter is the same as used in Chapter 5. The full model at geological scale (approx. 3.2 million grid cells) is used in the uncertainty quantification. Table 6.1 provides basic parameter settings for the model.

Table 6.1: Thermal and hydraulic properties of the geothermal reservoir.

Parameter	**Unit**	**Value**
Porosity	-	(10^{-5}, 0.256)
Permeability	mD	(0.004, 1308)
Shale heat capacity	kJ/m^3/K	2300
Sandstone heat capacity	kJ/m^3/K	2450
Initial temperature	K	348.15
Initial pressure	bars	200
Rate (doublet 1)	m^3/h	208
Rate (doublet 2)	m^3/h	208

6.2.2. NUMERICAL MODEL

Recalled from Chapter 2, the general mass and energy conservation equations are taken to model the dynamic flow and transport processes during the development. In low-enthalpy geothermal reservoirs, brackish to highly saline water is often encountered and used as working fluids with some chemical additives. Without loss of generality, the saline brine is chosen as the heat carrier here.

$$\frac{\partial}{\partial t}(\phi\rho_f) - div(\rho_f u_f) + \rho_f \tilde{q}_f = 0, \tag{6.1}$$

$$\frac{\partial}{\partial t}(\phi U_f + (1-\phi)U_r) - div(h_f \rho_f u_f) + div(\kappa \nabla T) + h_f \rho_f \tilde{q}_f = 0, \tag{6.2}$$

where Eq. (6.1) is the mass conservation equation and Eq. (6.2) is the energy conservation equation. Here ϕ is the porosity, ρ_f is the fluid density [kg/m^3], u_f is the fluid flow velocity [m/s], $\tilde{q}_f$ is the fluid source/sink term per volume [1/s], U_f is the fluid internal energy [kJ/m^3], U_r is the rock internal energy [kJ/m^3], h_f is the fluid enthalpy [kJ/kg], and κ is the thermal conductivity [kJ/m/day/K].

6.2.3. ECONOMIC MODEL

To perform the economic analysis, the model from Daniilidis *et al.* [68] is used. The power [W] produced from the well is computed according to

$$P_{well} = Q\rho_f h_f, \tag{6.3}$$

in which Q is the flow rate [m^3/s]. The required pump power [W] only considers the pressure drop in the reservoir,

$$P_{pump} = \frac{\Delta P Q}{\eta}, \tag{6.4}$$

where ΔP is the pressure difference between the injection and production wells [Pa] and η is the pump efficiency. The total system power is evaluated as

$$P_{system} = P_{prod} - P_{inj} - P_{pump}. \tag{6.5}$$

The cumulative energy produced from the system is computed using

$$E_{cum} = \sum_{t=0}^{n} P_{well_t}, \tag{6.6}$$

where n is the project time, t is the specific year. The cost of drilling the well is computed according to

$$C_{well} = 375000 + 1150Z + 0.3Z^2, \tag{6.7}$$

where Z is the measured depth along the wellbore. The NPV is calculated as [81]

$$NPV = \sum_{t=0}^{n} \frac{CF_t}{(1+r)^t}, \tag{6.8}$$

where *CF* is the cash flow on a yearly basis, r is the discount rate. Cash flow simply means the difference between income and cost during a certain period of time. The cumulative produced power generates income based on the heat price, while the pump power costs are computed based on the electricity price. In order to evaluate the combined system, the generated energy is first calculated on a doublet basis. The aggregated results are then used for the NPV calculations, over one year intervals.

6.3. UNCERTAIN PARAMETERS

6.3.1. POROSITY-PERMEABILITY REALIZATIONS

In our study, 100 realizations have been generated based on variation of the seed parameter in facies model of the base case [82]. It is assumed that 100 realizations are able to approximately represent the uncertainty existing in the porosity-permeability (shortly, poro-perm) distributions. The mean and standard deviation of parameters was kept as delivered and only the spatial distribution has been varied. Initially, the facies have been generated using sequential indicator simulation for the Berkel Sandstone and object modeling for the channelized Delft Sandstone. Porosities have been generated by using sequential Gaussian simulation, and permeabilities have been generated using co-kriging of porosity both in Petrel [82]. Fig. 6.1 displays the porosity-permeability distributions of three realizations.

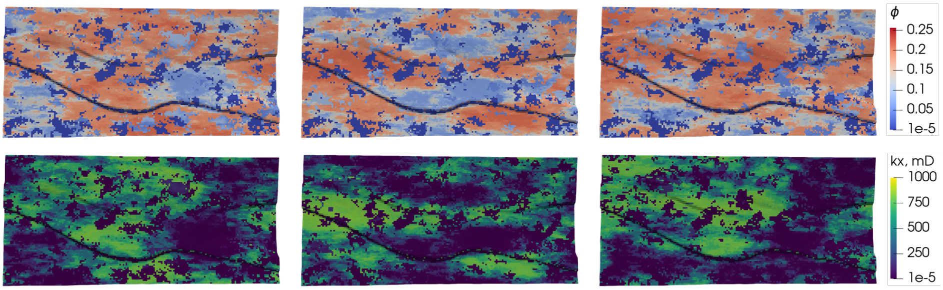

(a) (b) (c)

Figure 6.1: Top view of the porosity and permeability distribution of three realizations. The first row lists the porosity distributions, while the second row shows the corresponding permeability distributions.

6.3.2. SALINITY

According to Batzle and Wang [83], the brine density as a function of salinity, temperature and pressure is described as,

$$\rho_s = \rho_w + S\left[0.668 + 0.44S + 1e^{-6}\left(300P - 2400PS + T(80 + 3T - 3300S - 13P + 47PS)\right)\right]. \tag{6.9}$$

The brine viscosity as a function of salinity and temperature is described as,

$$\mu_s = 0.1 + 0.333S + (1.65 + 91.9S^3)\exp\left[-\left(0.42(S^{0.8} - 0.17)^2 + 0.045\right)T^{0.8}\right], \tag{6.10}$$

where ρ_s and ρ_w are saline and water density [kg/m^3], μ_s is viscosity [mPa$\cdot$s], S is the brine mass fraction [ppm/10^6], P is the pressure [MPa] and T is temperature [°C]

Determined by the dissolved minerals and solids, the reservoir fluid can be categorized from almost fresh water to highly saline brine [84, 85]. Salinity in a geothermal system has an impact on heat propagation and the production process. Based on Saeid *et al.* [86], the increase of salinity will result in a decrease in energy production and system lifetime for the investigated homogeneous reservoir. Since fluid samples are lacking, the specific salinity value is uncertain for the target reservoir. To account for the uncertainty of specific salinity, a wide distribution of salinity values is selected for our analysis, conforming to the approximate normal distribution (mean $\mu = 0.75$ ppm/1e6, standard deviation $\sigma = 0.40$ ppm/1e6 Fig. 6.2). The salinity value in each MCS sample is assumed as constant spatially.

6.3.3. ROCK THERMAL CONDUCTIVITY

The rock thermal conductivity determines the speed of heat exchange when a temperature gradient is present. The importance of the thermal conductivity of different rocks for heat production and propagation in geothermal systems has been studied and stressed [87]. It can be measured in the laboratory or at in-situ conditions. It varies with several factors, for example, mineral composition of the rock, the presence of fluids, pressure, etc. Prediction of the heat production should consider the introduced uncertainties in rock conductivity by these factors. The target reservoir in this study consists of two types of rocks, shale and sandstone, both of which are sedimentary rocks. The thermal conductivity of shale and sandstone is assumed to follow a normal distribution. Fig. 6.2 lists the distribution for shale conductivity as an example. Typical numbers are selected in the normal distribution [88, 89] for shale (mean $\mu = 190.1$ kJ/m/day/K, standard deviation $\sigma = 8.64$ kJ/m/day/K) and sandstone (mean $\mu = 259.2$ kJ/m/dayK, standard deviation $\sigma = 8.64$ kJ/m/day/K). A selected value will be assigned to certain facies by the MCS sampler.

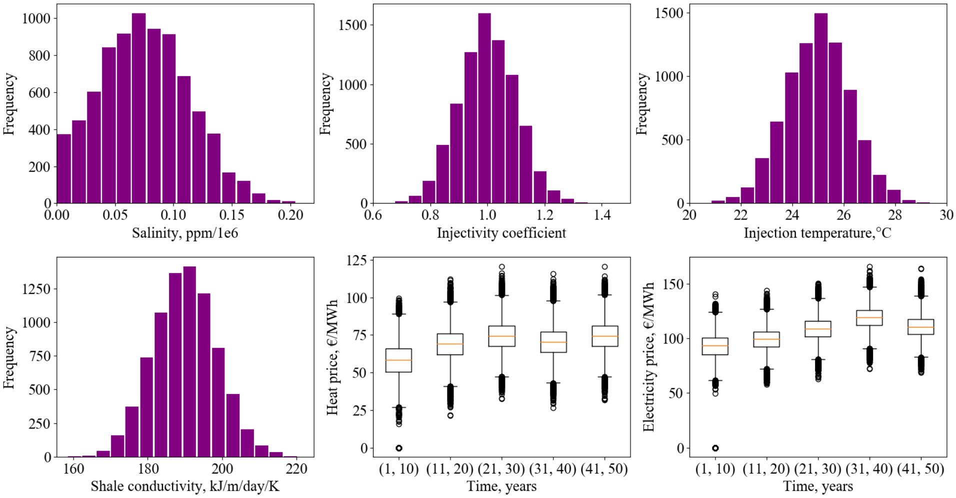

Figure 6.2: Distribution of the uncertain input parameters.

6.3.4. INJECTION TEMPERATURE

Energy production is subject to the injection temperature, which will influence the production temperature and lifetime of the geothermal reservoir [86, 90]. The magnitude of the injection temperature can vary with heat exchange and heat losses during energy utilization and transportation. Therefore, the injection temperature is expected to fluctuate a bit. A normal distribution (mean $\mu = 25$ °C, standard deviation $\sigma = 1.5$ °C Fig. 6.2) is assumed to describe the uncertainty existing in the injection temperature.

6.3.5. WELL INJECTIVITY

The re-injection of cold water into the reservoir can initiate mineral precipitation or thermal cracking [91] in the near-wellbore region. The injectivity of a geothermal doublet will be reduced or enhanced correspondingly. In numerical simulation, the well index (e.g., the Peaceman equation [92] $WI = \frac{2\pi\sqrt{k_x k_y}h}{\ln(r_w/r_o)}$) is used to characterize the well injectivity. Here, based on the default evaluation of well index, an injectivity coefficient is randomly sampled from a normal distribution (mean $\mu = 1$, standard deviation $\sigma = 0.1$ Fig. 6.2). During the simulation, the coefficient will be multiplied to the default well index to represent the uncertainty of well injectivity. In this study, since both doublets operate with constant rate, the well injectivity will influence the pressure difference within each doublet. Therefore, the required pumping energy will be different.

6.3.6. ECONOMICS

Varying with the energy source and providers, the heat and electricity prices will fluctuate within the studied period. To more accurately examine the uncertain impact of heat and electricity prices on NPV, the 50-years simulation time has been divided into sub-intervals. Within each sub-interval, it is assumed the prices will fluctuate around a mean value within a normal distribution. The prices of each year within this interval will be sampled from the normal distribution. The distribution of heat and electricity prices is shown in Fig. 6.2. The relevant parameters for NPV calculation are listed in Table 6.2.

Table 6.2: Parameters in NPV calculation.

Parameter	**Unit**	**Value**
Pump cost	k€	500
Pump lifetime	years	5
Pump efficiency	%	60
OpEx (% of CapEx)	%	5
Discount rate	%	10

6.4. CONVERGENCE ANALYSIS

Though it is difficult to set general criteria to calibrate the convergence of MCS, the results are expected to reach statistical convergence when the amount of samples is large enough [73]. The convergence rate may vary with the problem studied and variables. In this study, the energy production and NPV are two of the most concerned parameters. The MCS is considered as converged once these two parameters reach certain converged values.

Fig. 6.3 and Fig. 6.4 plot the P10, P50 and P90 of the energy production and NPV with increasing number of MC samples. Fig. 6.3a shows an example of MCS convergence for P10. Based on the daily energy production rate, total energy production of each MC sample can be evaluated at the end of the simulation. The energy production of all realizations is then collected as a data set. With the increasing counting of MC samples,

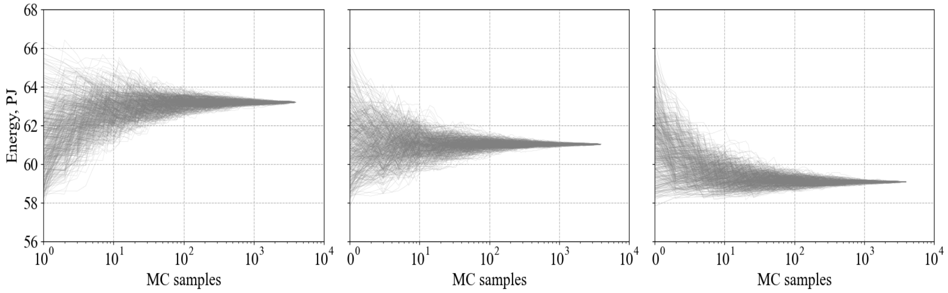

(a) P10 (b) P50 (c) P90

Figure 6.3: P10, P50 and P90 of the cumulative energy production of 50 years.

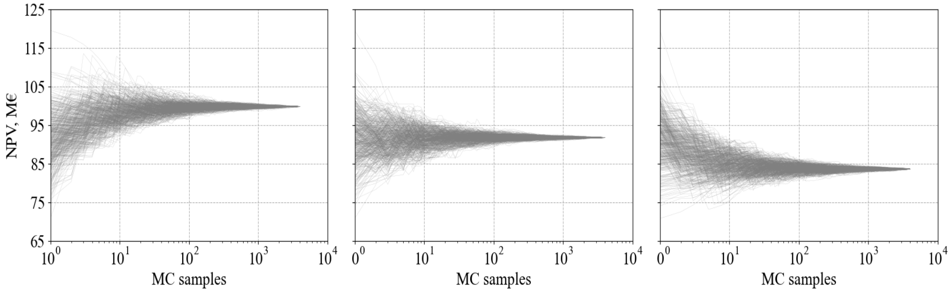

(a) P10 (b) P50 (c) P90

Figure 6.4: P10, P50 and P90 of the NPV of 50 years.

the 10% probability of the counted data are sequentially calculated, which in the end generates one curve in Fig. 6.3a. The data set is then randomly shuffled, and the 10% probability is re-evaluated correspondingly for multiple times. Fig. 6.3a is made up of all these evaluations with the similar procedures for other plots in Fig. 6.3 and Fig. 6.4. A wide spreading of produced energy and NPV is noticed while the number of realizations is limited. To get representative values of energy and NPV, a minimum of 2000 realizations are required in our study to converge MCS for a given quantile. The P10, P50 and P90 values of total produced energy in our study are 63.2, 61 and 59.1 PJ respectively, while the P10, P50 and P90 values of total NPV are 100, 92 and 84 M€ respectively.

In addition, it is essential to check the convergence of the values for the concerned parameters, as the other indication for MCS convergence. A convergence is assumed to be reached if the distribution stays stable with increasing the number of MC realizations. Fig. 6.5 shows L_2 norm of the difference between energy and NPV distributions in the MCS process. The L_2 norm is calculated by $||X_n - X_{n-1}||_2$, where X_n and X_{n-1} are the normalized distribution at current and previous computation steps. As expected, the distribution difference drops with the increase of MC sampling. With an approximate 2000 realizations, the distribution difference becomes smaller than 1%, which is regarded as converged.

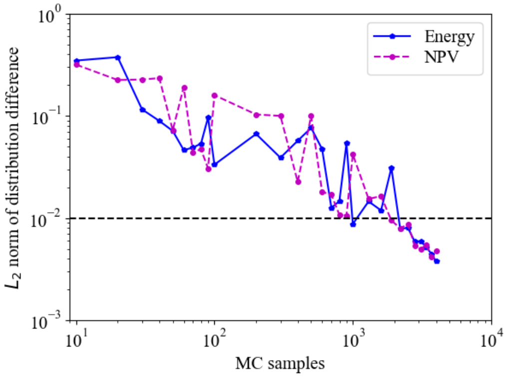

Figure 6.5: L_2 norm of the distribution difference with the increase of MC samples for produced energy and NPV.

6.5. NUMERICAL RESULTS AND DISCUSSION

6.5.1. PRODUCTION TEMPERATURE AND PRESSURE DROP

Fig. 6.6 displays the production temperature of all realizations for both doublets. A maximum temperature difference of 8 K at 50 years of operation for doublet 1 is observed. The production temperature of doublet 1 is largely impacted by the uncertain parameters. A temperature of 340.5 K (P50) has the highest probability at the end of the simulation. As a comparison, the spread in production temperature after 50 years for doublet 2 is only 4 degrees, demonstrating a relatively weak temperature response to the uncertainty of input parameters. In addition, the overall temperature drop for doublet 2 is less than for doublet 1, which is an indication of well interference. The well interference suggests that there is a diversion effect of doublet 1 to the injection well of doublet 2, which influences the thermal propagation of doublet 2. As is shown in Fig. 5.1, the injection well of doublet 2 is close to the producer of doublet 1, which promotes the water supply from doublet 2 to doublet 1. Therefore, the cold front propagation becomes slower in doublet 2.

Fig. 6.7 shows the drop of Bottom Hole Pressure (BHP) of all realizations for both doublets. The pressure drop of doublet 1 after 50 years ranges from 35 bars to 80 bars (Fig. 6.7a), where a 54-bars drop represents the P50 value. The pressure drop of doublet 2 varies from 45 bars to 145 bars, where 80-bars is the most probable pressure drop (P50). The uncertain parameters influencing the physical and geological properties give rise to the wide distribution in pressure drop. The distribution demonstrates that the uncertain parameters have a much stronger impact on the pressure calculations for doublet 2. In addition, the magnitude of pressure drop calculated for doublet 2 is, on average, larger than for doublet 1. This indicates that the average permeability is smaller within the controlled area of doublet 2, as the distance between the two wells in both doublets is similar.

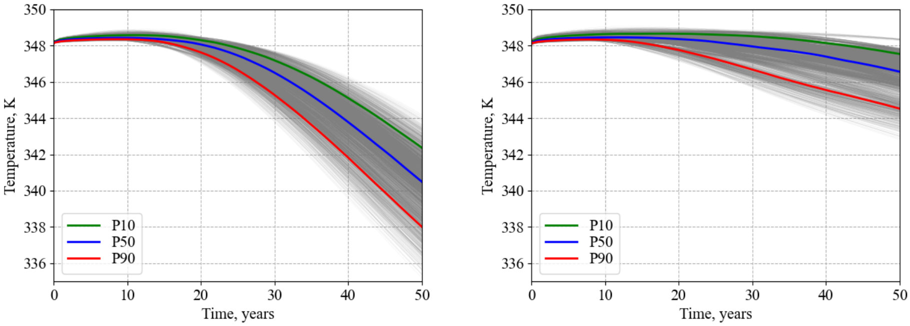

(a) doublet 1

(b) doublet 2

Figure 6.6: Production temperature of doublet 1 and 2, and the corresponding P10, P50, P90 production temperature curves.

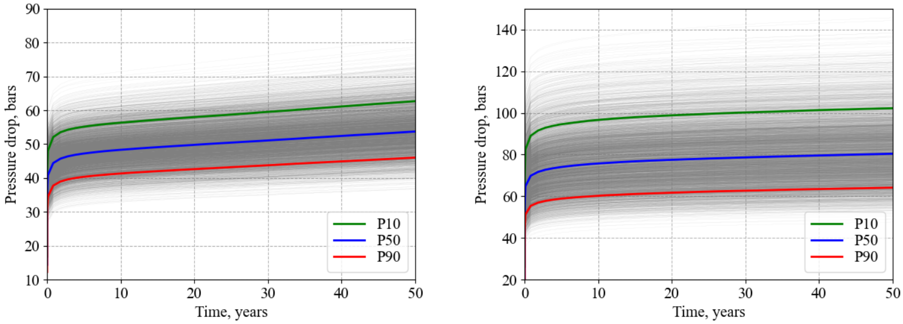

(a) doublet 1

(b) doublet 2

Figure 6.7: Pressure drop between BHP of doublet 1 and 2, and the corresponding P10, P50, P90 of pressure difference.

6.5.2. ENERGY, NPV AND BREAK-EVEN TIME

Fig. 6.8 displays the distribution of the total cumulative produced energy and NPV of both doublets for all realizations at the end of the simulations. While the NPV follows a classic Gaussian-type distribution, the energy follows a beta-like distribution. Since the input parameters are sampled with normal distributions (except the randomly sampled poro-perm realizations), the observed system response to the combined input seems predictable, although the individual impact of each input parameter can be different, as discussed below. However, for complex subsurface systems as in this study, the output from ensemble models will be highly case-dependent, which is difficult to predict without systematic forward simulations. Assumptions made in this study, such as fixed production rate of each doublet, reduce the variability of the final results and limit the uncertainty analysis.

After 50 years, the difference of energy production between P10 and P90 is 4.1 PJ, while the spread of NPV between P10 and P90 is 16 M€. To quantify the uncertainties, I define an uncertain factor (α) as the percentage of (P10, P90) difference and P50 value, $\alpha = \frac{(X_{P10} - X_{P90})}{(X_{P50})} \times 100\%$. With this definition, the uncertainty of NPV (17.39%) is much larger than that of produced energy (6.72%). On the one hand, it is because two additional uncertain input parameters (heat and electricity price) are considered in the NPV evaluation. On the other hand, the NPV calculation takes more factors into account (e.g., pressure drop within a doublet, injected energy, etc.), which will be discussed in the following section. As a comparison, the produced energy is more correlated with the heat transport and thermal exchange inside the reservoir.

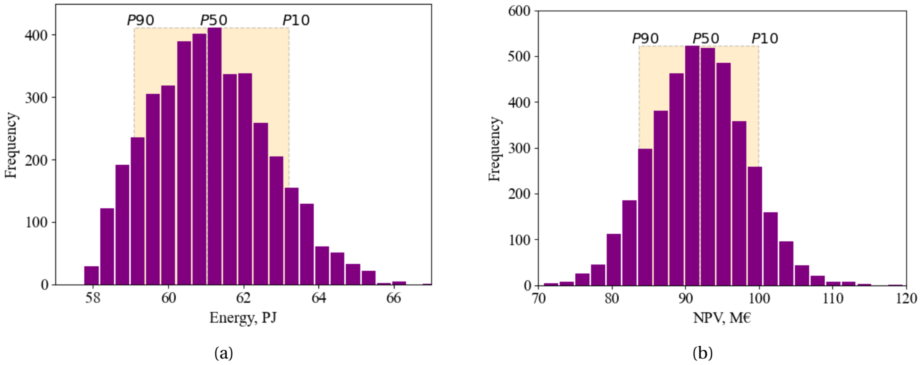

Figure 6.8: Energy and NPV distributions after 50 years. The samples falling between P10 and P90 of each distribution are marked in orange.

Fig. 6.9 displays the cumulative NPV of all realizations and the converged break-even time. As is shown in Fig. 6.9a, a large cash investment is required at the beginning of the project, including drilling and equipment costs. Based on a 10% discount rate, the NPV already experiences decelerated growth at the end of the 30th year and reaches a plateau within the last 20 years of production.

Break-even time refers to the amount of time required for the discounted cash flows generated by a project to match its initial cost. With the selected production strategy, a break-even time of less than 2 years is expected, which will be an attractive information for the investors. This project will become net profitable after 2 years and no risk factors are foreseeable with the uncertainty of the parameters considered in this study.

6.5.3. UNCERTAINTY OF SYSTEM OUTPUT TO INDIVIDUAL PARAMETERS

The output uncertainty to aggregated input parameters has been discussed in the previous parts. This section will show the influence of individual uncertain parameters to energy and NPV under the presence of other uncertain parameters.

In Fig. 6.10, the independent impact of six parameters (poro-perm realization, salinity, injectivity coefficient, injection temperature, shale and sandstone conductivity) to total energy production is listed. In each subplot, values of the investigated parameter are first divided into sub-intervals, which are used as filters for the MC samples. The energy distribution of the filtered MC samples is then plotted against each sub-interval correspondingly. The sensitivity of energy to different parameters can be observed within

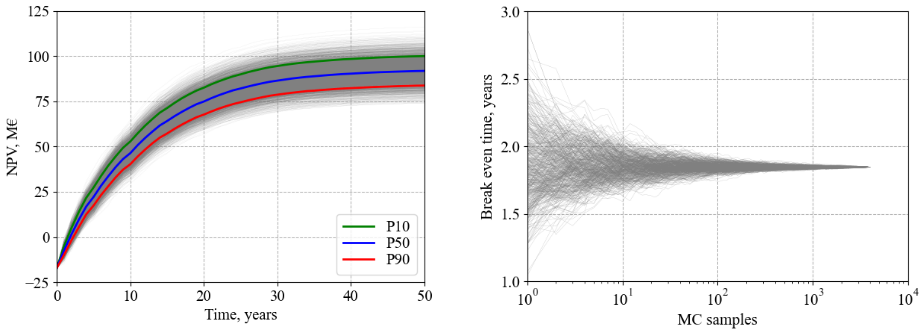

(a)

(b)

Figure 6.9: (a) Cumulative NPV of all realizations along the simulation and P10, P50, P90; (b) Break-even time.

these plots.

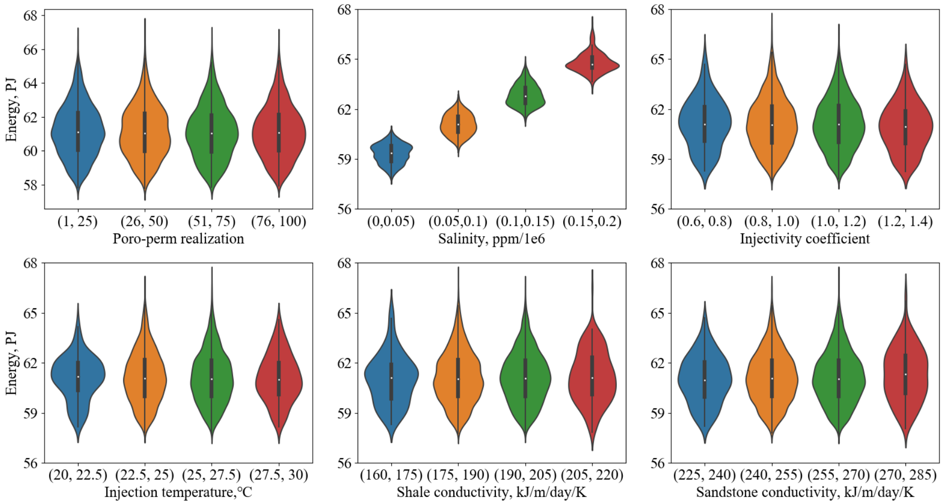

Figure 6.10: The uncertainty of energy production to single uncertain input parameter.

Influenced by other input parameters and by the number of filtered realizations, the distribution of produced energy varies significantly within each subplot. However, the mean values of energy are not sensitive to individual parameters, except to the salinity. The energy production is directly associated with the fluid density Eq. (6.3), which is the function of salinity Eq. (6.9). Therefore, the shift of mean energy value to salinity is straightforward. The injectivity coefficient mainly influences the operating pressure difference within each doublet and the energy production is not visibly affected under the constant rate operation. In fluvial systems, shale influences energy production via thermal conduction as an additional heat source. In our previous work with the same model [87], the significant influence of shale on the energy production is analyzed by including and excluding the shale facies. However, the sensitivity of energy production to the magnitude of shale conductivity was not studied before. In Fig. 6.10, the overall variation of produced energy with thermal conductivity is not obvious for typical conductivity ranges.

Similarly, Fig. 6.11 displays the uncertainty of NPV to six parameters (poro-perm realization, salinity, injectivity coefficient, injection temperature, mean heat and electricity price). Note that since the heat and electricity prices fluctuate with time, their mean value during the total 50-years period is collected for each MC realization, composing the data set of mean prices. I can see a large uncertainty of mean NPV with the variation of salinity, injection temperature and mean heat price. This also explains the observation of larger uncertainty in NPV than in energy from the previous section. Since NPV is positively correlated with generated energy, it increases with salinity and similarly with heat price as well. The injection temperature influences NPV via the system power (Eq. (6.5)) as higher injection temperature causes lower system power and therefore, lower NPV. The electricity cost only takes a small portion in the total NPV calculation, which is verified by the short break-even time (in Fig. 6.9b) of this project.

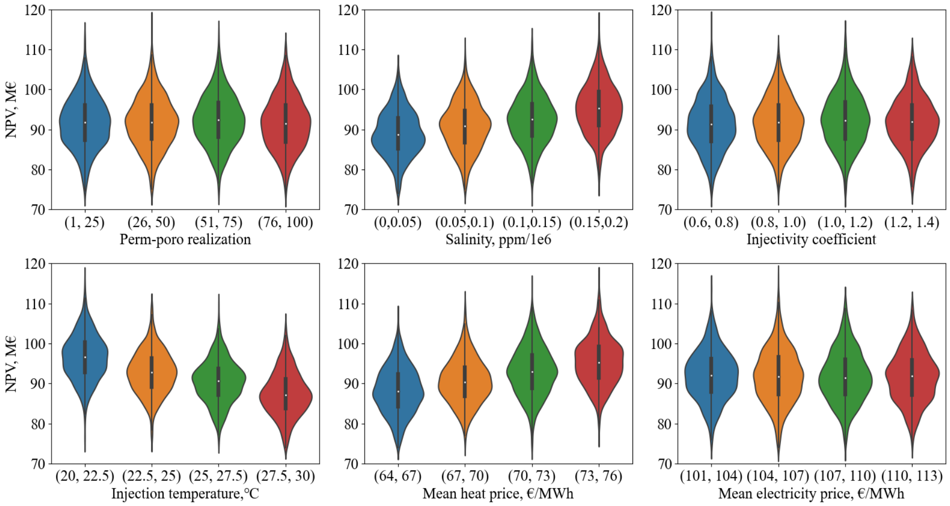

Figure 6.11: The uncertainty of NPV to single uncertain input parameters.

6.5.4. SIMULATION TIME

Owing to the high computing performance of the GPU version of DARTS, the mean simulation time for a 50-year simulation (with a maximum timestep of one year) stabilizes at 3.49 minutes on the Titan RTX GPU card. According to Khait *et al.* [45], the benchmarked simulation with the same model on single thread CPU of Intel Core i7-8086K requires about 80 mins to run for 100 years (or approximately 40 mins for a 50-years simulation). The performance has been improved by more than an order of magnitude.

Using the Monte Carlo method, it is convenient to run multiple simulations in parallel. This uncertainty quantification study was performed on 16 GPU cards simultaneously. The total 4000 simulations were finished within 15 hours.

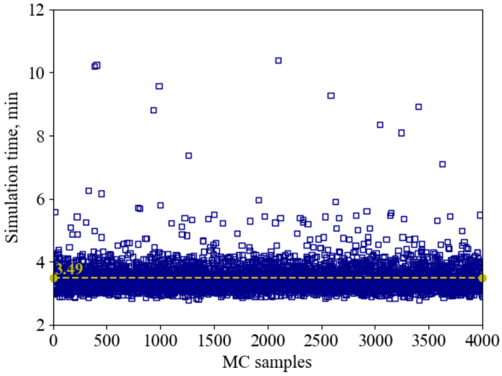

Figure 6.12: Simulation time of all realizations. The yellow dash line marks the mean value of the simulation time at 3.49 mins.

6.6. CONCLUSION

In this chapter, a systematic uncertainty quantification for a real geothermal reservoir from the West Netherlands Basin has been studied. The geological model entails detailed reservoir characterization with high-resolution meshes, which provides a unique model representation for the real application. The uncertain physical, geological and economic parameters are incorporated into the investigation, where the Monte Carlo method is used for parameter samplings. The high performance of the GPU version of DARTS and the parallelization of the Monte Carlo method guarantee the large ensembles of forward simulations finished in affordable time.

The two most concerned parameters (energy and NPV) are used as indicators for the convergence of the Monte Carlo Simulation. After examination of the MCS convergence, the uncertainties of energy and NPV are discussed according to the numerical results. A larger overall uncertainty is noticed for the NPV than for the energy, which is due to more factors included within the NPV evaluation. In real geothermal developments, the uncertain input parameters should be thoroughly considered to obtain valuable estimations of the concerned production characteristics. The uncertainty in the mean values of energy and NPV is less sensitive to some parameters, such as shale and sandstone conductivity, which indicates it is representative enough to just use typical values for these parameters.

With this study, I emphasize the importance of uncertainty quantification to geothermal field development by demonstrating how various uncertain parameters affect the predictions of produced energy and NPV. The aggregated impact of all these parameters cannot be recognized without systematic uncertainty quantification and ensembles of forward simulation.

7

HIGH-ENTHALPY GEOTHERMAL SIMULATION IN FRACTURED SYSTEMS

Summary

Multiphase flow in fractured geothermal reservoirs is numerically investigated. A discrete-fracture model is utilized to describe the fractured system. To characterize the thermal transport process accurately and efficiently, the resolution of discretization is necessarily optimized. A synthetic fracture model is firstly selected to run on different levels of discretization with different initial thermodynamic conditions. A set of comprehensive analyses are conducted to compare the convergence and computational efficiency of simulations. Based on the converged numerical solution, a thermal Peclet number is defined to characterize the interplay between thermal convection and conduction, which are the two governing mechanisms in geothermal development. Different heat transfer stages are recognized on the Peclet curve in conjunction with production regimes of the synthetic fractured reservoir. A fracture network, sketched and scaled up from a digital map of a realistic outcrop, is then utilized to perform a sensitivity analysis of the key parameters influencing the heat and mass transfer. Thermal propagation and Peclet number are found to be sensitive to flow rate and thermal parameters (e.g., rock heat conductivity and heat capacity). The proposed numerical simulation framework for fractured geothermal reservoirs provides the necessary procedures in practical investigations regarding geothermal developments with uncertainties.

The material presented in this chapter has been published in the Proceedings of World Geothermal Congress, Reykjavik (Iceland), 2020 [53] and submitted to a journal.

7.1. INTRODUCTION

Multiphase mass and heat transfer are ubiquitous in the subsurface within manifold applications. The presence of fractures over several scales and with complex geometry magnifies the uncertainty of the heat transfer process, which will significantly impact, or even dominate, the dynamic transport process. Capturing the details of fluid and heat transport within the fractured system is beneficial to the subsurface operations. However, accurate modeling methodologies for thermal high-enthalpy multiphase flow within fractured reservoirs are quite limited.

To precisely simulate mass and heat transport in fractured geothermal systems, a suitable fracture model is critical to capture the reservoir response. Two kinds of approaches are commonly used in the representation of fractured reservoir systems [93]. One is based on the continuum model, of which the typical examples are the dual-porosity model proposed by Warren and Root [94] and the dual-permeability model presented by Gerke and van Genuchten [95, 96]. The continuum model is an efficient simplification of the fracture system but is not accurate enough when dealing with discontinuous fractures and large-scale fractures dominating fluid flow [97].

Another approach is the discrete-fracture model (DFM), where the fracture networks are explicitly characterized by individual control volumes. Karimi-Fard *et al.* [52] proposed the discrete-fracture model (DFM), which is suitable for general-purpose reservoir simulators. DFM captures the pressure response generated by fractures accurately. However, it is computationally more expensive due to the introduction of additional degrees of freedom (for fractures) in the computational domain. Another approach proposed by Lee *et al.* [98] entails an effective representation of fractures in a computational domain and called embedded discrete-fracture model (EDFM). This approach has been greatly extended recently using multiscale technique by [99] and helps to control the computational performance and accuracy. However, the EDFM may not be as accurate as the DFM in some practical situations [100].

In this chapter, a computational framework is presented to numerically simulate mass and heat transport within fractured high-enthalpy geothermal systems. The DFM model is used to characterize the reservoir. In the following description, a comprehensive study on grid optimization and heat transfer dynamics is first conducted within a synthetic fracture model. Then, a realistic model based on practical outcrop measurements is utilized to perform numerical experiments with different parameters, and different scenarios are discussed.

7.2. MODEL DESCRIPTION

7.2.1. TRANSMISSIBILITY EVALUATION

The capability of discretizing complex fractured reservoirs in DARTS has been extended with the discrete-fracture model (DFM) [52]. This model represents the fracture geometry in the grid domain explicitly as a lower-dimensional feature, specifically a 3D model contains 2D fractures (planes) while a 2D model contains 1D fractures (lines). This is depicted in Fig. 7.1 for a 2D example. During the transmissibility calculations, each fracture is assigned a specific aperture, therefore, it will have a certain volume in the computational domain.

The transmissibility between neighboring grid blocks is expressed as:

$$T_{12} = \frac{\alpha_1 \alpha_2}{\alpha_1 + \alpha_2} \text{ with } \alpha_i = \frac{A_i k_i}{D_i} \mathbf{n_i} \cdot \mathbf{f_i}, \tag{7.1}$$

where A_i is the contact area between two neighboring blocks, k_i is the permeability of grid block i, D_i is the distance between the centroid of the interface and the centroid of the grid block i, $\mathbf{n_i}$ is the unit normal of the interface pointing inside block i, $\mathbf{f_i}$ is the unit vector along the direction of the line joining the grid block i to the centroid of the interface. This equation holds true for matrix-matrix, fracture-matrix, and fracture-fracture connections. When more than two fractures intersect in the same point (2D) or line (3D), a star-delta transformation is used to calculate the transmissibility between each of the intersecting fractures. See Karimi-Fard *et al.* [52] for more details.

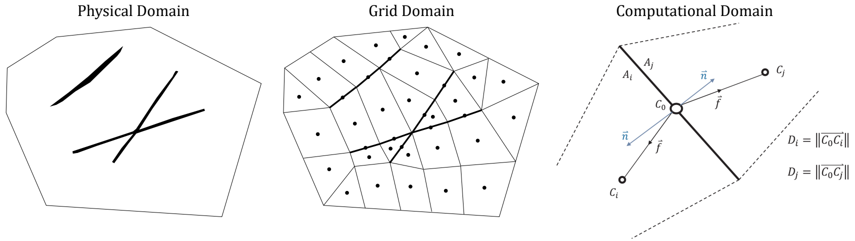

(a) (b) (c)

Figure 7.1: Schematic representation of the DFM model (modified from Awadalla and Voskov [101]).

Fracture networks usually contain complex fracture intersections that result in difficult meshing requirements. The generated mesh, therefore, often contains artifacts that negatively impact the performance of the reservoir simulation (i.e., convergence problems and numerical inaccuracies due to non-uniformity of the control volumes and large angles between $\mathbf{f_i}$ and $\mathbf{n_i}$). This is solved by using a pre-processing step in which each fracture is sequentially discretized, using the desired discretization scale (predefined size of the segment).

For fracture pre-processing, a procedure suggested by Karimi-Fard and Durlofsky [25] is adapted. During the sequential procedure, every iteration of the mesher is checked if the newly placed discretized fracture segment conflicts with any previously added segment. A conflict is defined here as two fracture nodes (end-points of each discretized fracture segment) that fall within a certain radius (half the discretization accuracy) of each other. This pre-processing step is computationally insignificant with respect to the main fluid-flow simulation time while still greatly improving the simulation results (accuracy and computational time). This method also allows for a fast and reliable way of creating the discretized fracture network at any desired resolution while maintaining the main characteristics of the original fracture characterization.

7.3. GRID OPTIMIZATION WITH SYNTHETIC MODEL

In general, high-resolution grids are necessary to capture details of fast convective flow in highly-permeable regions (such as fractures), while thermal conductive flow may require a lower level of grid discretization. Besides, the computational efficiency depends on the number of degrees of freedom of the model, correlating directly with the grid resolution. The first step in our study is to propose an optimal spatial discretization with enough accuracy and efficiency for modeling geothermal applications in naturally fractured reservoirs. This section describes the parameters of the selected fracture network, explains the model construction with predefined resolutions, shows the results of the numerical convergence study, and proposes the optimal grid resolution.

7.3.1. MODELS DESCRIPTION

A synthetic fracture configuration is selected to perform an analysis on grid discretization and heat transfer mechanisms. A doublet for injection and production is placed in the model, see Fig. 7.2 for details. For the simplicity of the analysis, I assume that the matrix is isotropic and homogeneous with a permeability of 0.001 mD. The aperture of the fracture is 3e−4 m and the cubic law [102] is taken to describe the hydraulic conductivity of the fracture. The fracture permeability with an aperture b is expressed as

$$k_f = \frac{b^2}{12}.$$

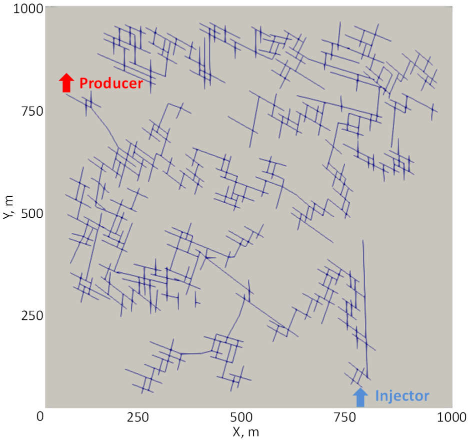

Figure 7.2: The size of the synthetic fracture network is 1000m × 1000m × 50m. The blue lines delineate the fracture network and the solid gray represents the matrix.

Two different initial conditions are selected. One is with vapor and liquid coexistence. The initial pressure is 100 bars, the initial enthalpy is 1500 kJ/kg which corresponds to the initial temperature of 588 K. At these conditions, the initial steam saturation is 0.47. The injection well condition is set with flow rate control of 350 m^3/day, the production well condition is set with bottom hole pressure (BHP) control of 80 bars. This reference conditions correspond to the typical case from a hot-spot area (e.g., The Geysers [17]).

Another type of conditions corresponds to an ultra-deep geothermal reservoir filled with critical water. The initial pressure is 450 bars, the initial enthalpy is 660 kJ/kg which corresponds to the temperature of 423 K. The injection well condition is set with flow rate control of 300 m^3/day, the production well condition is set with bottom hole pressure (BHP) control of 400 bars.

7.3.2. SPATIAL DISCRETIZATION AT DIFFERENT RESOLUTIONS

An optimal grid resolution is essential for both accurately presenting the fracture network and improving computational performance. Here, four levels of discretized models, increasing resolution from Grid 1 to 4 as shown in Fig. 7.3, are selected to characterize the fracture network. Table 7.1 lists the detailed grid numbers of different grid sets. The sensitivity of simulation results to the grid resolution will be identified with different models. To capture the fast convective flow in the fracture, the number of grid cells utilized to discretize the fractures has to stay dense across different levels of resolutions.

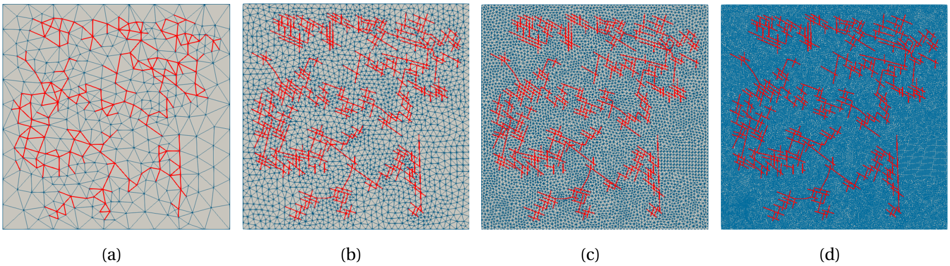

(a) (b) (c) (d)

Figure 7.3: Grid resolutions with four sets of discretization increase from left to right, Grid 1 to 4. The number of matrix cells varies in an order of magnitude from Grid 1 to 4. Compared to matrix cells, meshing for the fractures keeps dense among various resolutions to capture the fast convective flow taken place in the fractures.

Table 7.1: The number of grid cells for different grid sets.

Grid set	No. of fracture cells	No. of matrix cells
Grid 1	276	702
Grid 2	1088	4516
Grid 3	1628	11954
Grid 4	3211	46446

Comparing the numerical solutions of different discretization ratios will help to propose an optimal grid resolution for thermal flow in fractured reservoirs. The temporal variation of production temperature in conjunction with the parameter distribution (e.g., the temperature, saturation, and pressure) at the selected time is utilized to quantitatively compare the results between different models. The solutions for the grid with the highest resolution (Fig. 7.3d) are taken as the reference and compared with solutions generated from models at lower resolutions (Figs. 7.3a to 7.3c).

7.3.3. RESOLUTION STUDY

Direct comparison of production temperature gives evidence to the accuracy of different levels of discretization. Fig. 7.4 displays the temperature profile of the production well for the two test cases (two-phase and critical water conditions) under different grid resolutions. With the grid refinement, the temperature curve approaches the reference solution gradually. Grid 3 (solid green line) can closely capture the referenced temperature drop for both cases. The temperature decline (Fig. 7.4) can be simply divided into two consecutive parts along with time: the short rapid drop at the early period (i.e. < 7000 days Fig. 7.4a) and the following elongated mild drop. Figs. 7.5 to 7.7 display the distribution of the temperature, pressure and water saturation at certain selected simulation time for the two-phase system.

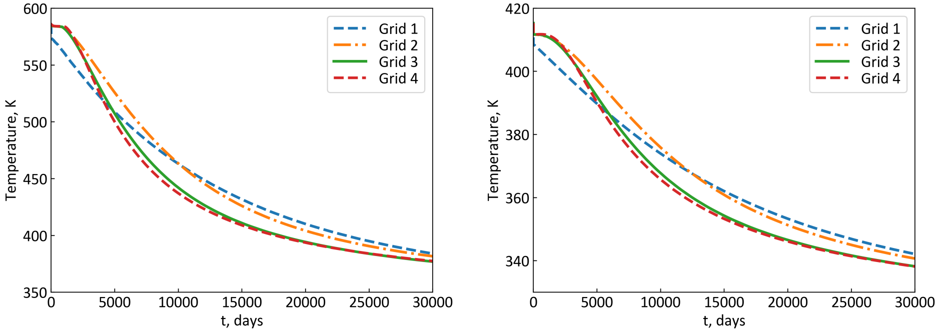

(a)

(b)

Figure 7.4: Production temperature for initial conditions with (a) two phases (b) critical water with different levels of grid discretization.

The temperature map for coarser resolutions (e.g., Fig. 7.5a) show more dispersed cold water distribution than the finer ones (e.g., Fig. 7.5c), which results from the assumption of instantaneous thermodynamic equilibrium within one control volume. For coarser resolutions, the averaged size of computational control volumes is larger than that under finer resolutions. For the same amount of matrix volume surrounded by several fractures, the energy depletion under a coarser grid representation will be faster than its counterpart under finer resolutions. A coarse grid block, represented by several control volumes under finer resolution, will deplete integrally when the temperature gradient exists, which enables faster energy depletion. The same amount of energy depletion under finer resolutions will, however, experience several transitional steps between control volumes, whereby the energy depletion will slow down and conform to the referenced process. Following a similar logic, the Multiple INteracting Continua (MINC) model ([103, 104]) was proposed for approximately modeling mass and heat transport in fractured systems.

Overall, the spreading of the cold water plume for different resolutions is similar and converges with refinement. The grid set 3 (Fig. 7.5c) can already accurately represent the solution of temperature in the computational domain. Since the initially distributed two-phase high-enthalpy geothermal system is the focus of this study, the solutions of pressure and saturation are also need to be checked while comparing different grid sets. It is obvious from Fig. 7.6 and Fig. 7.7 that the pressure and saturation distributions present higher sensitivity to grid resolutions than the temperature.

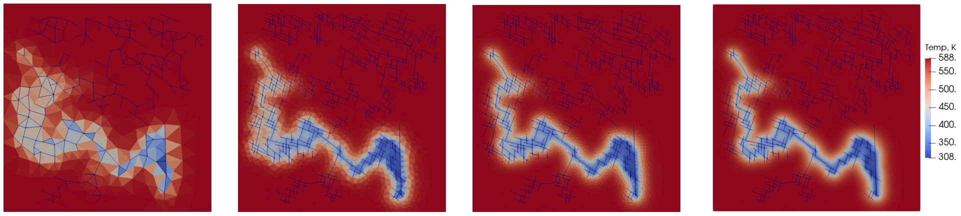

(a) (b) (c) (d)

Figure 7.5: The temperature maps with different levels of grid discretization at 10000 days. The maps from left to right refer to Grid 1 to 4.

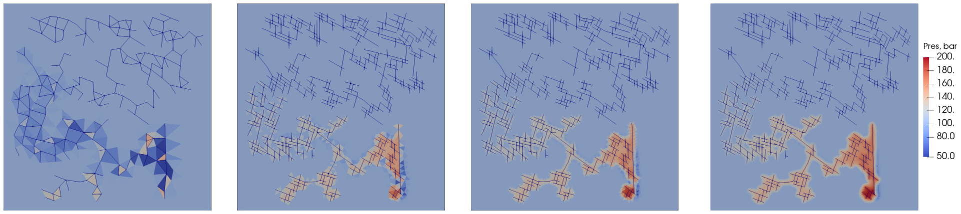

(a) (b) (c) (d)

Figure 7.6: Pressure distribution with different levels of grid discretization at 1000 days. The maps from left to right refer to Grid 1 to 4. Since the pressure propagates much faster than the temperature, an early simulation time (1000 days) is selected to show the pressure distribution of the entire domain among the resolutions.

At the thermal front, the pore pressure will decrease subject to the steam condensation triggered by the energy depletion [38], which is a highly nonlinear process and can impact the solution of pressure in the entire domain. In comparison with the referenced pressure distribution (Fig. 7.6d), the pressure gradient buildup looks slower for models with coarser discretization (Fig. 7.6a and Fig. 7.6b). This can be explained by the larger averaged volume of computational grids, as for the temperature difference mentioned above. Saturation, as a function of enthalpy and pressure, is also sensitive to the grid resolution (Fig. 7.7). Restricted by the solution of pressure, the propagation of water saturation with coarser resolutions (Fig. 7.7a and Fig. 7.7b) cannot precisely capture the phase distribution under the reference resolution. As it is observed in (Fig. 7.6c and Fig. 7.7c), the distributions of pressure and saturation for Grid 3 closely match with the finest resolution of Grid 4.

7.3.4. COMPUTATIONAL PERFORMANCE AND ACCURACY

The computation time of each run is measured during the simulation, as an indicator for numerical performance. Fig. 7.8a displays the simulation time of both two-phase and critical water systems under various grid resolutions. The performance is scalable with the grid resolution, as an almost linear relationship is observed between the logarithm

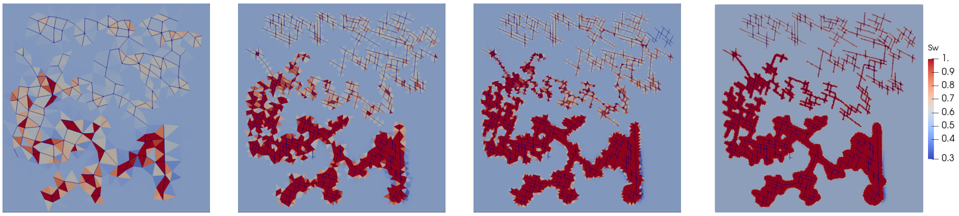

(a) (b) (c) (d)

Figure 7.7: The saturation distribution with different levels of grid discretization at 1000 days. The maps from left to right refer to Grid 1 to 4. Calculated from the solutions of pressure and enthalpy, the phase distribution at early simulation time (1000 days) is selected.

of CPU time and control volumes numbers in the serial runs. Grid 3 can run about 10 times faster than Grid 4 (the finest resolution) with reasonable accuracy as shown in Fig. 7.8b. It is worth noticing that the accuracy of solution depends on fractured network modification and the accuracy of nonlinear physics representation as can be seen in Fig. 7.8b as well. Here, the more linear critical water model converged to the reference solution faster than the two-phase model. Considering the fact that solutions at coarser resolutions (Grid 1 and 2) are not accurate, the resolution of Grid 3 is proposed for farther analysis. Besides, because of the heavier numerical nonlinearity associated with the two-phase system, more nonlinear iterations are needed than for the one with critical water, and therefore computation is more time-consuming for the two-phase system.

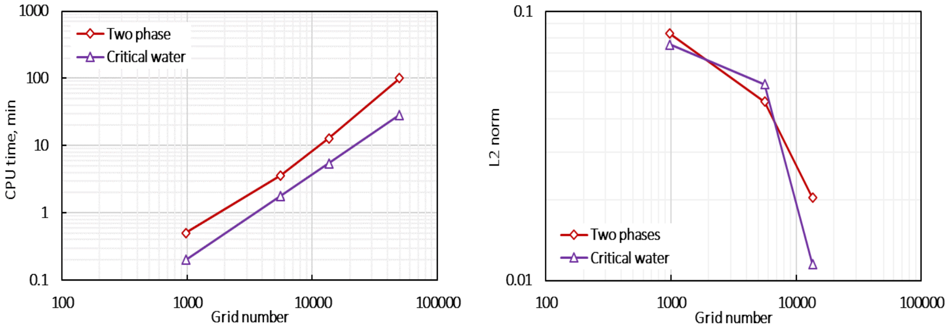

(a) (b)

Figure 7.8: (a) Computation time under different levels of grid resolutions for the two initial conditions. (b) L2 norm to the difference of production temperature between the three levels of resolutions (Grid 1 to 3) and referenced resolution (Grid 4).

7.4. DYNAMIC HEAT AND MASS TRANSFER

Thermal convection and conduction are the two main mechanisms governing heat transfer in the subsurface. A thermal Peclet number (Pe) is defined to quantify the interplay between thermal convection and conduction, whereby the heat transfer dynamics is studied and discussed. The optimal grid discretization (Grid 3) of the synthetic fractured reservoir is utilized in the following analysis.

7.4.1. THERMAL PECLET NUMBER

For mass transfer, the Peclet number characterizes the interplay between the convective and diffusive flow. As the energy analog of mass transport, the thermal Peclet number quantifies the relative strength of convection and conduction during heat transport. The dimensionless thermal Peclet number is defined as follows:

$$\mathrm{Pe} = \frac{\sum_{p=1}^{n_p} \int_t h_p \rho_p Q_p \, dt}{\sum_{i=1}^{n_f} \int_t \int_{\Omega_{\mathrm{fi}}} div(\kappa \nabla T) \, d\Omega dt}, \tag{7.2}$$

where Q_p refers to the flow rate of a specific phase ($p = w, s$ for water and steam phase) at the production well, Ω_{fi} denotes the control volume of the i^{th} fracture. This interpretation is only suitable for fractured systems with low-permeability matrix, as in this study, where the thermal convective flow can be considered as dominating in the fracture network while the fracture-matrix heat exchange is through thermal conduction.

7.4.2. DYNAMIC HEAT TRANSFER REGIMES

Fig. 7.9a displays the temporal evolution of the Peclet number. Four stages are detected on the Peclet curve, representing different heat and mass transfer dynamics. Correspondingly, the dynamic simulation statistics for different stages are recognized in Fig. 7.9b. Overall, the Peclet number increases as simulation proceeds, which demonstrates the relative strength of thermal convection grows during the simulation.

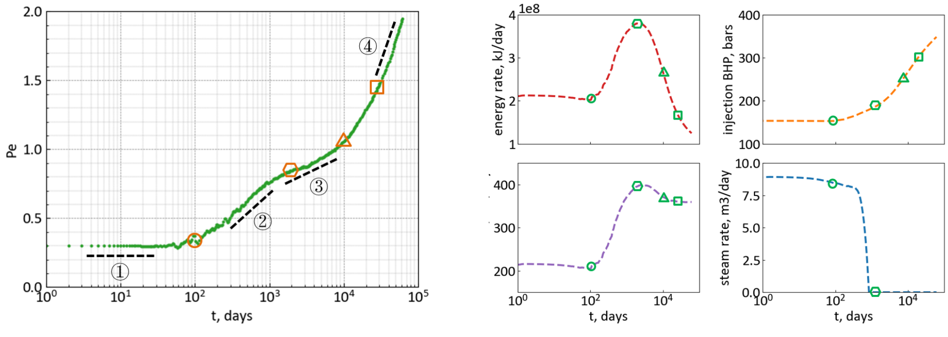

(a)

(b)

Figure 7.9: Temporal evolution of (a) Peclet number and (b) simulation statistics with the optimal grid discretization. In (b), the energy rate refers to the daily energy production, injection BHP refers to the bottom hole pressure of the injection well, water rate refers to the daily water production, steam rate refers to the daily steam production.

STABLE TWO-PHASE FLOW

A constant thermal Peclet number (stage ①) is observed (Fig. 7.9a) for the first 100 days, which indicates a stable interplay between convection and conduction. Since the energy production rate is almost constant during this period (Fig. 7.9b), the thermal conductive flow stays stable as well. Fig. 7.10 ◯ displays the temperature map of the model at 100 days. Only a small region of the matrix near the injection well shows a minor temperature change. As enthalpy and temperature are independent in the two-phase state, the matrix temperature stays unchanged while the enthalpy drops until the two phases transit to a single phase. The phase transition (Fig. 7.11◯) is a faster process than the temperature propagation, since phase transition is more sensitive to pressure variations. In this period, stabilized two-phase flow occurs in the fractures, which can be deduced from the stable water and steam flow rates observed at the production well. The injected cold water, heated up by the hot rock, vaporizes in the fractures. Because of the existence of highly compressible steam, the pressure buildup within the fracture network does not take place instantaneously, which is quite different for the quasi-incompressible fluid system. Correspondingly, the needed injection pressure to sustain the operation scheme is stable (Fig. 7.9b).

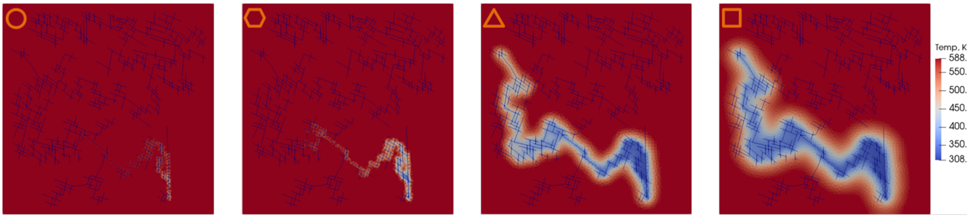

Figure 7.10: Temperature propagation at four simulation time nodes: 100 (◯), 2000 (⬡), 10000 (△) and 30000 (□) days at fine resolution.

TRANSIENT TWO-PHASE FLOW

As the simulation proceeds, the Peclet number increases quickly (stage ②), which mainly results from the condensed water breakthrough in fractures. As is shown in Fig. 7.9b, the energy and water rates increase drastically during this period. Due to heat exploitation, the produced energy cannot support water vaporization under the fixed production pressure. Therefore, the steam rate decreases to zero and the energy production curve reaches the maximum energy rate (Fig. 7.9b). The water production rate increases owing to the pressure buildup in the fractured system, which can also be observed in Fig. 7.9b. The cold water plume penetrates deeper towards the producer (Fig. 7.10⬡). A larger volume near the injection well depletes by thermal conduction.

The production temperature (Fig. 7.4a) remains unchanged at the end of this period (2000 days), which indicates the thermal front has not reached the production well yet. However, the fractures are fully saturated with condensed water (Fig. 7.9b). The saturation profile (Fig. 7.11⬡) shows the phase transition of the matrix cells along the fracture cells between injection and production wells at 2000 days.

TRANSIENT SINGLE-PHASE FLOW

From 2000 to 10000 days, the increment of the Peclet number becomes mild (stage ③). The heat transferred by both the thermal convection and conduction decreases as the time proceeds. The energy contained in unit-volume of fluid drastically decreases, since

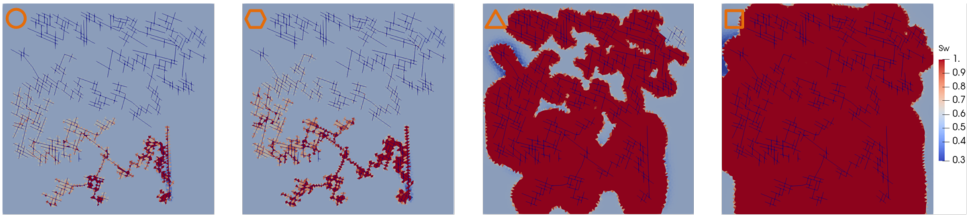

Figure 7.11: Snapshot of water saturation at four simulation time nodes: 100 (◯), 2000 (⬡), 10000 (△) and 30000 (□) days under fine resolution.

the energy rate reduces sharply with just a mild decrease in water flow rate (Fig. 7.9b). The heat transferred by thermal conduction is expected to reduce more than by convection as the Peclet number keeps increasing during this period. From Fig. 7.10△, the temperature of the matrix surrounding the fractures decreases a lot at 10000 days. Since thermal conduction is proportional to the temperature gradient and inversely proportional to grid distance, the thermal recharge of the fluids in the fractures by the matrix weakens along time. This can also be verified from the production temperature curve (Fig. 7.4a). The temperature decline in this period is sharp and steep due to the fast temperature drop in the matrix adjacent to the fractures.

As the average temperature of the fracture fluid drops, the fluid density and viscosity increase correspondingly, which leads to higher flow resistance within the fractures. The pressure needed to maintain the constant injection rate keeps increasing (Fig. 7.9b). Another interesting observation is the phase transition in the regions without direct contact with cold water. Owing to the pressure elevation within the model, the steam phase in the matrix condensates to water phase (Fig. 7.11△).

STABLE SINGLE-PHASE FLOW

After 10000 days, the Peclet number rapidly increases (stage ④). As is shown in Fig. 7.10□, the matrix energy has widely depleted at 30000 days. The thermal convective flow becomes dominant as the conduction turns less influential in heat transfer due to energy extraction. The water production stabilizes in this period with only a minor decrease in the energy production rate. In parallel, the increase of injection pressure slows down simply because the temperature change of the fluids slows down after 10000 days (Fig. 7.4a).

7.5. NUMERICAL EXPERIMENTS WITH REALISTIC MODEL

7.5.1. BACKGROUND

The fracture network used in this section is taken from an outcrop of the Whitby Mudstone Formation [51]. The horizontal network was first captured from birds-eye view imagery of the pavement with an extent of about 100m at sub-cm resolution. The imagery was interpreted in the aspect of fracture orientation, length and density. Individual fractures were manually traced from and assembled on the constructed digital map. 2148 fracture segments were recognized from the images. The fracture network is scaled up to the size of 1200m × 1600m × 50m for simulations. The geometry of the fracture network is depicted in Fig. 7.12a.

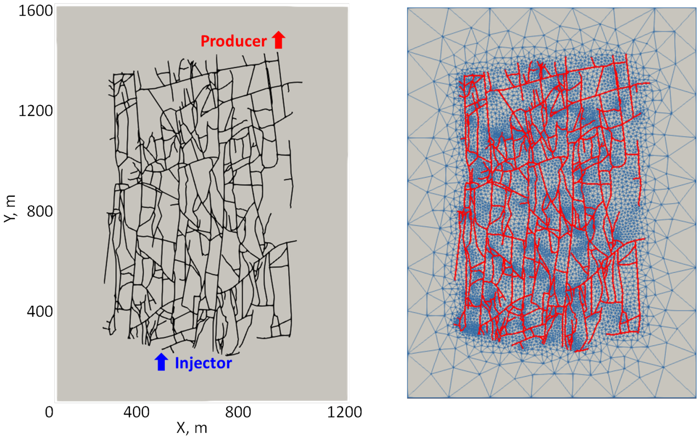

(a) (b)

Figure 7.12: The fracture network interpreted based on the bird's-eye view imagery of an outcrop at the Whitby Mudstone Formation. The black lines delineate the fracture network and the solid gray represents the matrix. Grid discretization with 2234 fracture segments and 14014 matrix cells.

7.5.2. GRID DISCRETIZATION

A reasonable grid resolution is essential for both accurately presenting the fracture network and enhancing the computational performance. Here, a grid discretization (Fig. 7.12b) with characteristic length of 7.5 m (the same as Fig. 7.3c) is selected to characterize the fracture network. Compared to Wang *et al.* [53], the mesh quality is improved by the optimized treatment at the model boundary. In addition, a benchmark study against state-of-the-art research simulator has been conducted in Chapter 3.

7.5.3. NUMERICAL EXPERIMENTS AND DISCUSSIONS

In this section, I compare the heat transfer dynamics inside the model with different parameter settings: fracture-matrix permeability ratio, flow rate, rock heat conductivity and heat capacity. The parameter settings of the base case are listed in Table 7.2.

FRACTURE-MATRIX PERMEABILITY RATIO

Permeability is one of the key factors strongly influencing thermal flow and transport. Depending on the geological formation, the matrix permeability can vary from high (porous sandstone) to low (almost impermeable basalt). The permeability contrast between fracture and matrix reflects their relative ability for fluid flow to percolate. It is important to analyze the cold front propagation under different realistic permeability ratios. A set of fracture-matrix permeability ratios is chosen and examined to observe the thermal response for different scenarios. The variation of permeability contrast is achieved by adjusting the matrix permeability, while the fracture aperture for simplicity of interpretation is fixed. Here I choose typical matrix permeability for different types of

Table 7.2: Base case parameter settings.

Parameter	**Value**
Matrix permeability, mD	0.001
Fracture aperture, m	3e−4
Fracture permeability, mD	7.5e6
Rock heat conduction, kJ/m/day/K	200
Rock heat capacity, kJ/m^3/K	2500
Initial pressure, bar	100
Initial enthalpy, kJ/kg	1500
Initial steam saturation	0.47
Injection well condition, m^3/day	1000
Production well condition, bar	80

rocks: sandstone (100mD), carbonate (1mD) and basalt (0.001mD), where the fracture-matrix permeability ratio will be 7.5e4, 7.5e6 and 7.5e9.

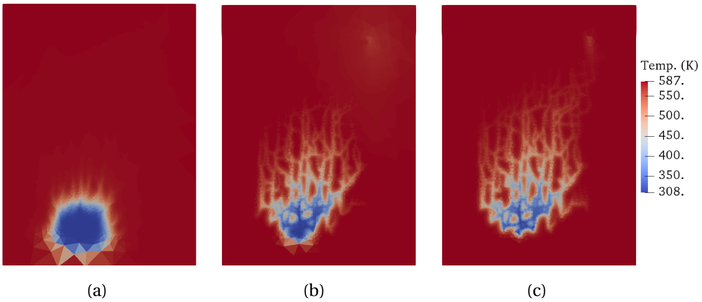

(a) (b) (c)

Figure 7.13: The temperature distribution with different fracture-matrix permeability ratio (a) 7.5e4 (b) 7.5e6 (c) 7.5e9.

Fig. 7.13 displays the temperature distribution for different permeability ratios, where large differences of the cold front propagation can be observed. For the lowest permeability contrast (Fig. 7.13a), the cold front propagates surrounding the injection well. Since the matrix permeability is higher in this case, the preferential heat transport along fractures is not prominent. With the increase of permeability ratio, the fluid flow in the fracture becomes much easier than in the matrix, therefore the cold front spreads following the branches of the fractures towards the production well.

Fig. 7.14 shows the impact of fracture-matrix permeability ratio on the production temperature. With a large permeability ratio, the injected water is pushed to flow through the fractures and the heat exchanges between fracture and matrix mainly through thermal conduction. Therefore, the amount of depleted energy is lower in fracture-dominated flow and the temperature declines faster than for lower permeability ratios. In addition, due to the diversion effect of the high-permeable matrix, fluid flow in the fractures is re-

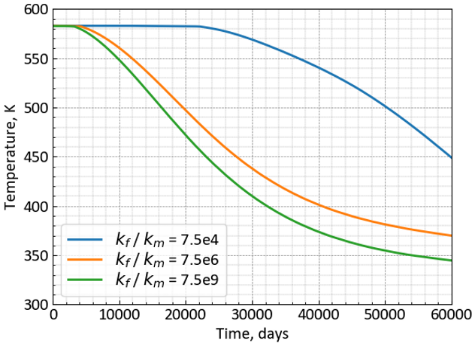

Figure 7.14: Temporal evolution of the production temperature under different fracture-matrix permeability ratios.

duced which facilitates heating the fluids within the fractures. Consequently, the shape of the temperature curve with the lowest permeability ratio (blue line in Fig. 7.14) becomes largely different from the rest.

FLOW RATE

The flow rate directly associates with mass and heat transport. For real field applications, the flow rate is a key focus that will determine the thermal breakthrough time [105]. Therefore, it is crucial to determine how the heat transfer dynamics change with the flow rate in fractured porous media. Five different injection flow rates are utilized to investigate their influence on thermal propagation. Fig. 7.15 displays the temperature distribution at different flow rates. Larger volumes deplete with the increase of flow rate. Fig. 7.16a shows the production temperature for different flow rates. The temperature drops earlier and faster with the elevated flow rates, resulting from the more powerful convective flow in the fractures. The cumulative energy production is displayed in Fig. 7.16b. Here, 500 K is selected as the checking point to compare the cumulative energy production with different flow rates. The amount of cumulative energy slightly increases with the reduction in flow rate, which is different from similar observations in fluvial systems [87]. The highly preferential convective flow in fractures makes the fracture-matrix heat exchange less sufficient under higher flow rates. In addition, no extra flow paths get involved in heat production with the increase of flow rate, as indicated in Fig. 7.15.

Fig. 7.16c shows the thermal Peclet number for different flow rates. The Peclet number is constant at the early stable two-phase flow regime, where the thermal conduction is stronger than the convection under any flow rate. As time proceeds, differences are observed in the Peclet curves as stronger convection is expected with higher flow rates. The inflection point (purple arrow in Fig. 7.16c) on the Pe curve corresponds to the point where the temperature starts decreasing in the production temperature curves Fig. 7.16a. The inflection point shows up earlier on the Peclet curve with increasing rates, consistent with the observation in Fig. 7.16a. Afterward, the convection dominates the heat transfer process with the rapid increase of the Peclet number.

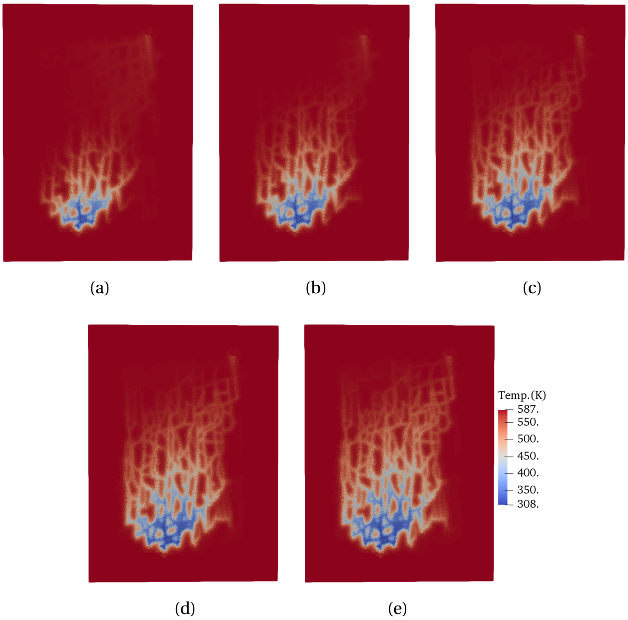

Figure 7.15: The temperature distribution with different rates (m^3/day) (a) 500 (b) 750 (c) 1000 (d) 1250 (e) 1500.

ROCK HEAT CONDUCTION

Conduction plays a vital role in heat extraction during geothermal development, especially in the case of low permeable rocks. Conductive heat flow happens when the temperature gradient builds up between control volumes. The strength of thermal conduction is proportional to the magnitude of temperature gradient and heat conductivity. In this section, various rock heat conductivity values are selected within a realistic range to study the sensitivity of thermal propagation to heat conductivity in fractured reservoirs.

Fig. 7.17 shows the temperature distribution with different heat conductivity. With the same amount of water injected, the cold front propagation is more confined with larger heat conductivity (Fig. 7.17e). Since stronger conductive heat exchange happens under larger conductivity values, the reservoir energy close to the injection well largely depletes. When conductivity decreases, it will need more contact with the matrix to heat the fracture fluids and therefore, the temperature front spreads deeper towards the production well. Correspondingly, the region near the injection well weakly depletes (e.g., Fig. 7.17a). The influence of rock conductivity to thermal propagation is clearly nonlinear since the variations shrink as the conductivity increases.

The production temperature for different heat conductivity is shown in Fig. 7.18a. Consistent with the temperature distribution, an earlier temperature drop is observed at the production well with lower heat conductivity. The temperature decline converges as conductivity increases, as is shown for $\kappa = 200, 300, 400$ kJ/m/day/K, which demonstrates the conduction effect approaches its upper bound. Further increase of conductivity is unable to heat the fluids even more because either the fluid has already been

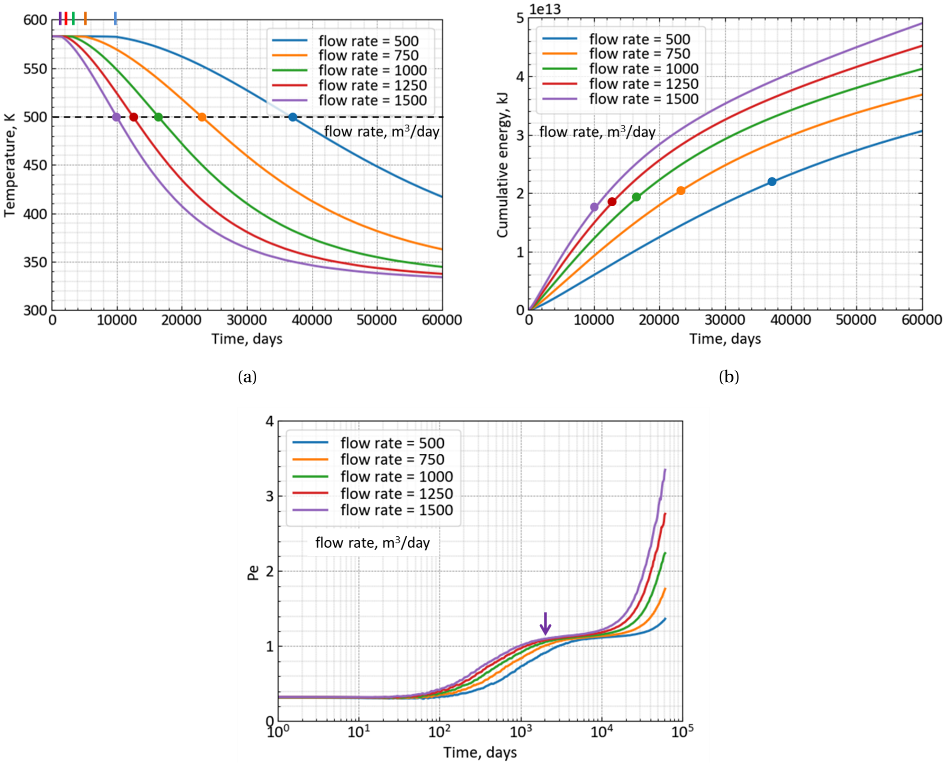

(a)

(b)

(c)

Figure 7.16: Temporal evolution of (a) production temperature (b) cumulative energy production and (c) thermal Peclet number under different flow rates. The short colored lines at the top in (a) specify the time when production temperature starts dropping. The arrow in purple in (c) marks the reflection point on the Peclet curve of rate 1500 m^3/day, correlating with the time when the production temperature starts decreasing. Similar inflection points can be specified for different rates.

heated up or the rock has been cooled down. Overall, the variation of production temperature with conductivity is not as significant as with permeability ratio or flow rate.

The Peclet curves are similar under different heat conductivity (Fig. 7.18b). As a multiplier in conduction calculation, smaller heat conductivity will limit the conductive rate. However, the broader spreading of the cold front along fractures with low conductivity enlarges the contact area for heat conduction. Consequently, quite similar Peclet profiles are observed for different cases.

ROCK HEAT CAPACITY

Volumetric heat capacity proportionally correlates with the amount of energy contained in the rock. Larger heat capacity simply means a larger amount of energy is contained in the reservoir. Here, five values of rock heat capacity within a realistic range are selected to investigate its influence on heat production.

As shown in Fig. 7.19, the thermal propagation is largely different from the variation

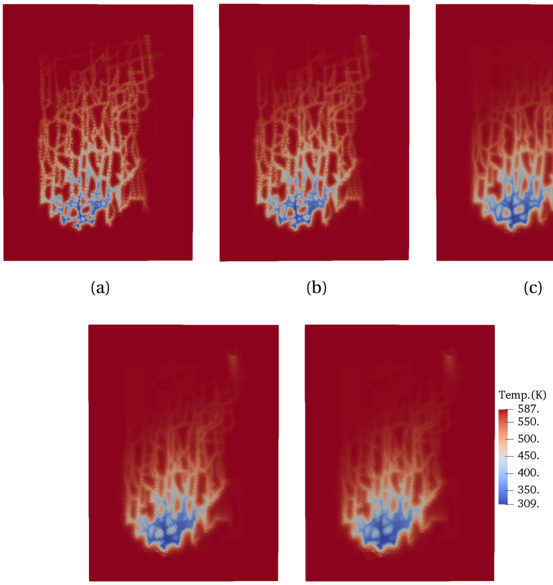

(a) (b) (c)

(d) (e)

Figure 7.17: Temperature distribution for realistic range of rock heat conductivity (kJ/m/day/K) (a) 50 (b) 100 (c) 200 (d) 300 (e) 400.

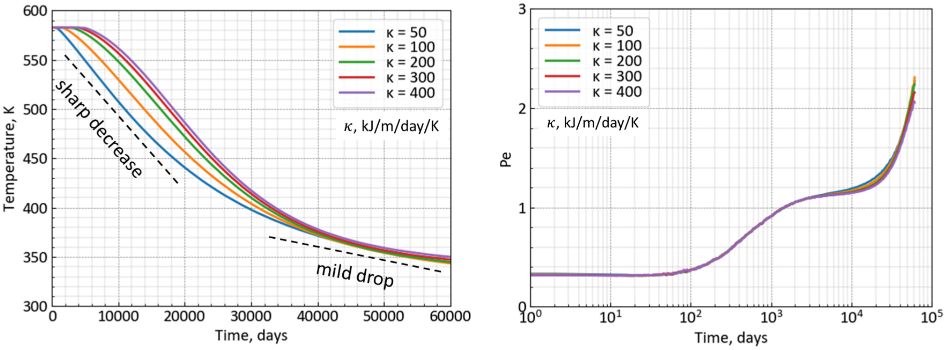

(a) (b)

Figure 7.18: Temporal evolution of (a) production temperature and (b) thermal Peclet number for realistic range of rock heat conductivity.

in rock heat capacity, reflecting the different capabilities of reservoir rock resisting energy depletion. With the same amount of cold water injection, a larger portion of the reservoir depletes with lower heat capacity (e.g., Fig. 7.19a). This is because the cold water quickly depletes its bypassed reservoir via conduction and therefore, a larger reservoir volume is involved in the energy depletion process at the selected time or for certain specific simulation time.

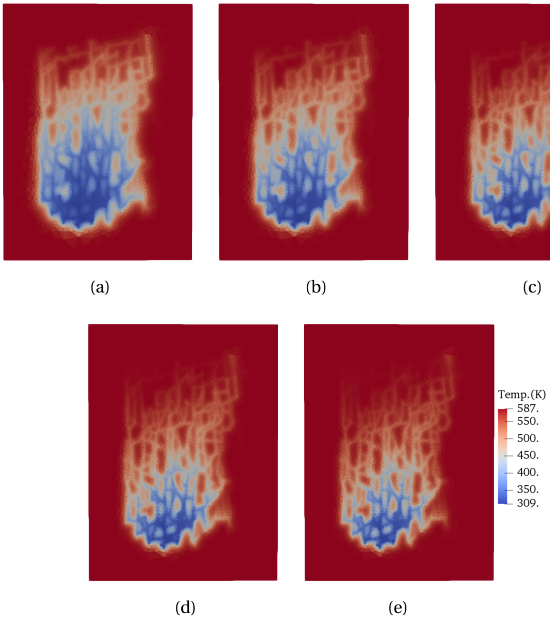

(a) (b) (c)

(d) (e)

Figure 7.19: Temperature distribution for realistic range of rock heat capacity (kJ/m^3/K) (a) 1500 (b) 2000 (c) 2500 (d) 3000 (e) 3500.

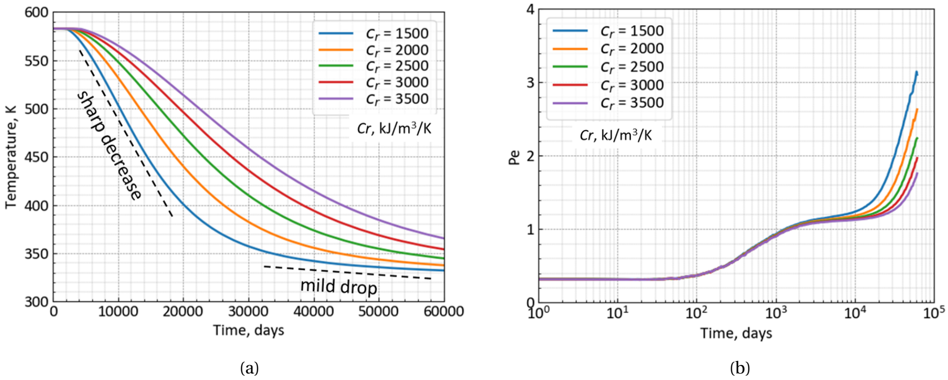

(a) (b)

Figure 7.20: Temporal evolution of (a) production temperature and (b) thermal Peclet number for realistic range of rock heat capacity.

Fig. 7.20a displays the changes in production temperature with heat capacity. The production temperature shows a similar two-stage decline for all considered cases: sharp decrease and mild drop. The faster temperature drop with lower heat capacity corresponds closely with the observation in Fig. 7.19. Overall, the heat capacity shows a roughly linear influence on production temperature, since the difference between curves keeps almost the same with the linear change of heat capacity. The difference in thermal

Peclet numbers (Fig. 7.20b) becomes noticeable as the temperature starts decreasing. Rock with larger heat capacity will supply stronger energy to the injected cold water via thermal conduction, while the convective flow can be taken as the same for different cases. Therefore, the Peclet number is smaller under larger heat capacity.

7.6. CONCLUSION

In this chapter, the multiphase mass and heat transport in fractured reservoirs is numerically investigated. Fractures are explicitly depicted with the discrete-fracture model (DFM) and the mesh quality of the DFM discretization is improved through a pre-processing procedure. Based on the numerically converged model, a sensitivity study of heat transfer in fractured reservoirs with different numerical and physical parameters is performed to guide the uncertainty quantification and optimization processes.

First, a simulation framework is presented to comprehensively investigate the sensitivity of simulation results to mesh resolution with a synthetic fractured model. The optimal mesh discretization is selected out of several resolutions. It is highly recommended to qualify the mesh discretization when modeling geothermal transport within fractured systems using accurate fractured models, which will both guarantee precise simulation results and greatly improve computational performance. Subsequently, a thermal Peclet number is defined for fractured systems with low permeable matrix. Four different flow stages and relative strength between thermal convection and conduction are recognized from the Peclet curves. A geothermal system becomes less efficient when heat transport is mostly convective dominated, as clearly indicated by the thermal Peclet number analysis.

Next, a fracture model sketched from a direct image interpretation of a realistic outcrop is discretized with the optimal characteristic length and utilized for parameter sensitivity analysis. Almost linear impact of flow rate and rock heat capacity to production temperature is observed, whereas rock heat conductivity displays a clearly nonlinear influence which is difficult to predict without the direct numerical simulation. Besides, the fracture-matrix permeability ratio can largely alter the shape of production temperature. These notable impacts of investigated parameters on thermal propagation and heat transfer dynamics provides insights for the future uncertainty analysis and practical development of fractured geothermal reservoirs.

The proposed investigation procedure on an optimal grid resolution is significantly important for improving the computation time without compromising the accuracy. Since there are not many publications on two-phase thermal transport in the fractured high-enthalpy geothermal system, this chapter fills a gap in the literature and highlights the basic influential factors for an optimal development of such a resource.

Please note that restricted timesteps are used to guarantee the nonlinear convergence of simulations with critical water and two phases. However, the case with critical water can be performed with much larger timestep, and only the two-phase simulation demonstrates a nonlinear divergence at larger timesteps. This happens due to the so-called 'negative comprehensibility' issue, which will be investigated in the next chapter.

8

NEGATIVE COMPRESSIBILITY ISSUE IN HIGH-ENTHALPY GEOTHERMAL SIMULATIONS

Summary

The so-called 'negative compressibility' numerical phenomenon appears when simulating the process of cold water invading steam-saturated control volumes. Because of the phase transition, the conventional Newton's approach may not guide the solution towards the correct direction. To tackle this problem, continuous localization of Newton's method is formulated based on the OBL technique. In the continuous localization approach, the coarse approximation of the governing physics is first selected in pressure-enthalpy parameter-space. Due to the more linear form of operators, only a few nonlinear iterations can reduce the residual below the predefined tolerance. Next, the OBL approximation is modified towards the reference nonlinear physics and a few more iterations bring the residual below the tolerance again. With the refinement in physics, the solution will gradually approach the final solution where the residual will satisfy the convergence criteria of the reference physics. This continuous localization in physics avoids the 'negative compressibility' phenomenon, since the problem at the coarser approximation has a unique gradient pointing towards the correct solution and helps to localize the solution for higher resolutions in the region of monotonous gradient behaviour. As a result, simulation can perform at larger timesteps in comparison to the traditional nonlinear solution.

Part of material in this chapter has been published in the Proceedings of the 44th Stanford Geothermal Workshop, Stanford University, California (USA), 2019 [106].

8.1. PROBLEM DESCRIPTION

During the operation of geothermal reservoirs, the re-injected cold water will be heated by in-situ fluid/rock and the heat is carried up to the surface through further water reinjection and cycling.

For high-enthalpy geothermal systems, either single phase (vapour or liquid) or a two-phase mixture can be present at reservoir conditions. When developing a high-enthalpy geothermal reservoir with cold water injection, hot steam condensation happens after its contact with cold water. Therefore, multiphase flow and transport with phase changes appear in high-enthalpy geothermal systems, which can be described with the mass and energy conservation equations. In geothermal simulation, the mass and energy formulations are often tightly coupled because of the fluid thermodynamic properties [107]. The fully-coupled fully-implicit approach is generally adopted to solve the formulation system.

In a high-enthalpy geothermal simulation, numerical simulators can experience great difficulties, one of which is commonly known as 'negative compressibility' [108]. This phenomenon was first described by Coats [108] for a single-cell setup, where cold water is injected at fixed pressure into a cell with saturated steam. Due to the invading cold water, hot steam will condense, and the cell pressure will drop with steam shrinkage during phase transition. The cell pressure will constantly decrease until the steam is condensed and cell pressure goes up to the injection pressure. To guarantee the convergence of nonlinear iterations, the timestep should be severely restricted, which is often addressed as 'stalling behaviour', see Pruess *et al.* [27] for example.

A similar issue was encountered in the previous chapter (Chapter 7) simulating the high-enthalpy system within fractured reservoirs at reasonable large timesteps. Pruess *et al.* [109] discussed the 'negative compressibility' problem. They connect the 'negative compressibility' effect to the idealization of complete thermodynamic equilibrium within the computational grids. Spurious pressure variation could happen in the cells that contain the two-phase front because of the instantaneous thermodynamic equilibrium assumption, which will enforce severe limitations to the nonlinear convergence. Wang [110] made an analysis of the 'negative compressibility' problem in the fully implicit formulations. In that analysis, to ensure convergence of the fully implicit solution, a stability criterion for the timestep was developed and unnecessary timestep cuts were avoided. However, the derived stability criterion still enforces a severe limitation to the allowable timestep size. Wong *et al.* [38] applied a nonlinear preconditioner to the fully coupled, fully implicit solution. The formulations were first solved with a sequential fully implicit approach (SFI) and then the solutions were taken as the initial guess for the fully implicit method (FIM) [111]. Using this approach, the severe timestep restriction was reduced for some practical scenarios. However, there is still no robust strategy for converging high-enthalpy nonlinear solutions at a target timestep in the presence of the 'negative compressibility' phenomenon.

The OBL approach provides an opportunity to control the nonlinearity in physics by changing the resolution of parameter space. In other words, if fewer supporting points are chosen in parameter space, the nonlinear physics will become more linear, which makes it easier for the nonlinear solver to converge [42]. In this chapter, I follow the hierarchy of physical approximation in parameter space using the OBL formalism and construct a continuous solution in physics to solve the 'negative compressibility' problem. I start with general formulations and numerical strategies used in thermal-compositional simulations and briefly introduce the OBL approach. Next, the 'negative compressibility' problem in the single-cell is described from the Newton path, residual distribution and operator surface. Afterwards, the continuous localization in physics is adopted to solve the 'negative compressibility'. In the end, a two-dimensional test case is used to verify the feasibility of the proposed method.

8.2. SINGLE-CELL ANALYSIS

8.2.1. FORMULATIONS

The 'negative compressibility' problem can be described using a single-cell model with a cold-water injection at fixed pressure [38, 108]. To facilitate the description, the following assumptions are made:

- Rock energy is neglected;
- Heat conduction is ignored;
- Rock is incompressible.

Therefore, the following mass and energy conservation equations for a single cell problem are obtained:

$$V\frac{\partial \rho_t}{\partial t} - \Upsilon(p_{\text{in}} - p) = 0, \tag{8.1}$$

$$V\frac{\partial \rho_t h}{\partial t} - H_{\text{in}}\Upsilon(p_{\text{in}} - p) = 0, \tag{8.2}$$

$$\rho_t = \rho_w s_w + \rho_s s_s, \tag{8.3}$$

where V is the cell volume, Υ is the flow transmissibility at the injection boundary, p_{in} is the fixed pressure of the injection boundary, p is the cell pressure, h is the cell enthalpy, ρ_t is the total fluid density, H_{in} is the injected enthalpy, ρ_w, ρ_s are the density of water and steam, s_w, s_s are the saturation of water and steam. Below, I take an example to illustrate this problem with $p = 50$ bar, $h = 2000$ kJ/kg, $s_s = 0.97$ and $p_{\text{in}} = 90$ bar, $H_{\text{in}} = 345$ kJ/kg.

8.2.2. NEWTON PATH

Wong *et al.* [38] derived and distinguished the timestep based on the pressure solution of Newton update. Here, I take the timestep that forces the Newton solution to diverge. Fig. 8.1 shows the Newton path with an initial guess chosen at the initial conditions. Because of the large variations in thermodynamic properties between water and steam phases, the residual equation becomes highly nonlinear.

In Fig. 8.1, two minima are recognized in the residual map: one (at the upper right part) is the local minimum, which does not correspond to the solution (here residual is not equal to zero); the other one (at the lower middle part) is the real solution of the problem. If the Newton update follows the gradient of the residual equation starting with the proposed initial guess, it will converge to the wrong local minimum. Please note that in conventional nonlinear solvers, the solution at previous timestep is taken as the initial

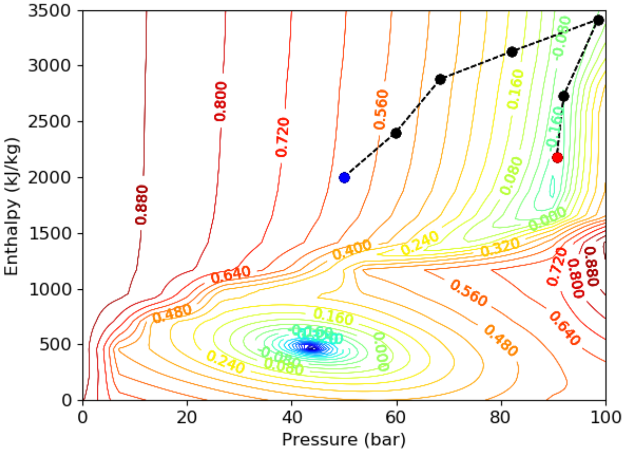

Figure 8.1: Newton path (dash line) starts from the initial condition; the contours (in l_2-norm) show the residuals, blue dot represents the initial condition of the cell, black dots are the Newton updates, red dot shows the solution for a current timestep.

guess for the Newton method, which can be any point in parameter space. To check how convergence for a given set of parameters depends on the initial guess, I choose uniformly distributed points within pressure-enthalpy space and check convergence for all of them respectively. The convergence map is shown in Fig. 8.2.

It is clear from Fig. 8.2 that the Newton path starting with points in the two-phase

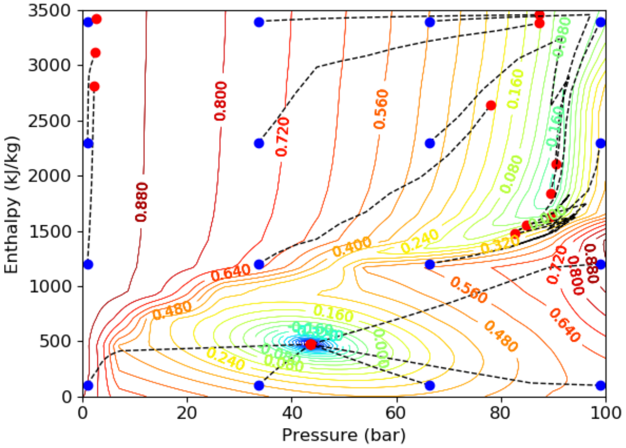

Figure 8.2: Newton paths (dash line) starts from various points in pressure-enthalpy space; the contours (in l_2-norm) show the residuals, blue dots represent the initial guess, red dots show the solution for a current timestep.

region (upper part of the residual map) will either diverge or converge to the local minimum; while for the points in the single-phase region, the Newton iterations will converge to the real solution. As result, if the initial guess is in the two-phase region, the simulation at this timestep will waste several nonlinear iterations and finally cut the current timestep (and, possibly, a few more after). This indicates that finding a suitable initial guess for Newton iterations is essential to guarantee the performance at a targeted timestep in a geothermal simulation with steam condensation.

8.2.3. OPERATORS

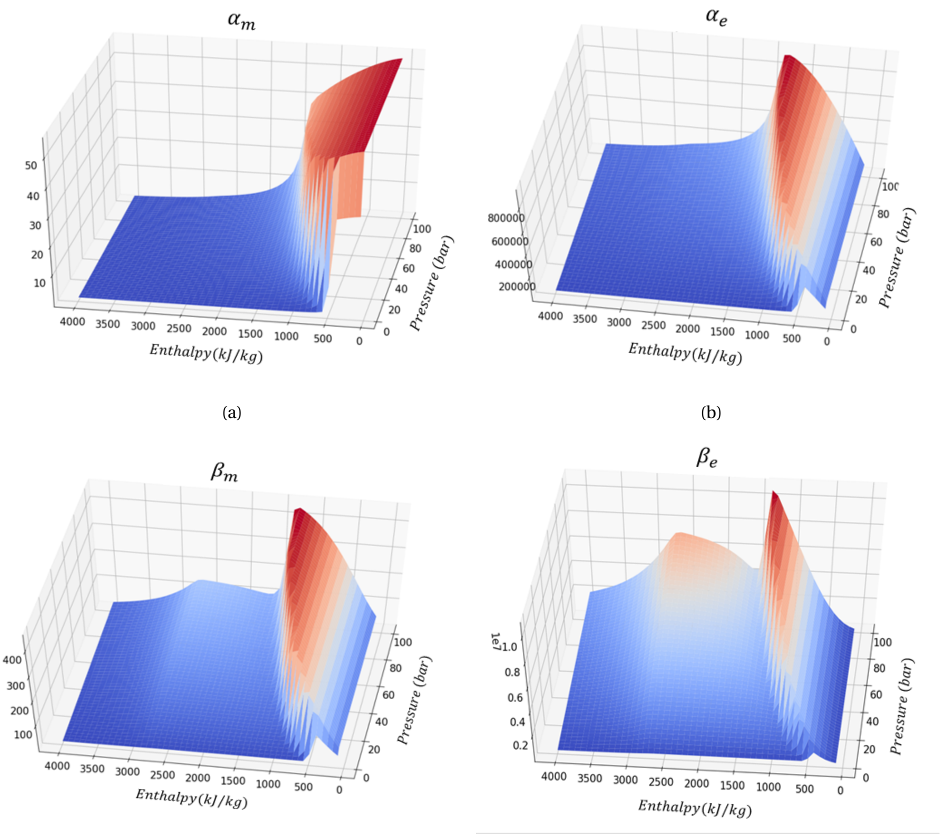

(a) (b)

(c) (d)

Figure 8.3: Operators in mass and energy conservation equations for the single cell problem. (a) mass accumulation, (b) energy accumulation, (c) mass flux, (d) energy flux.

In Fig. 8.3, the operators for mass and energy conservation equations are plotted with fine resolution tables. Here, α_m and β_m correspond to the accumulation and flux terms in the mass equation, α_e and β_e correspond to the accumulation and flux terms in the energy equation. All operators are highly nonlinear in pressure-enthalpy parameter space. If the initial guess is in the two-phase region, the Newton process cannot jump across the phase boundary and stays on the wrong side. This gives additional evidence to the fact that nonlinear solvers struggle in high-enthalpy geothermal simulations.

8.3. CONTINUOUS LOCALIZATION IN PHYSICS

Through the analysis above, I notice that the high nonlinearity in physics causes difficulties for the gradient-based nonlinear solver and forces it to update in the wrong direction. This inspired the approach with a multi-level physics parameterization.

8.3.1. PROCEDURES OF CONTINUOUS LOCALIZATION IN PHYSICS

1. Instead of solving the system with reference physics (fine parameterization), I start the simulation for a targeted timestep with the coarse OBL parameterization. Because of the coarse resolution of parameter space, the residual map will change and becomes almost linear with a monotonically behaving residual (see Fig. 8.4a as an illustration). This means that only a few iterations are needed to reach the solution at this coarse physics resolution. Note that even though the solution at this stage is different from the final solution, this solution is still close to the final solution.

2. The physical space is refined and the previous (coarse) solution is taken as an initial guess. The solution at this finer resolution will be located closer to the real (reference) solution. This will help to localize the Newton update and move in the right direction. Note in Fig. 8.4b that the full residual is already behaving non-monotonically and there is a region in parameter-space with a wrong gradient (in the upper-right part). However, the localization stage at a coarser level helps to safeguard the Newton update towards the true solution.

3. The physical space is refined to the reference resolution. Similar to the previous stage, the solution at previous OBL resolution is taken as an initial guess for the reference physical resolution. Even though the residual is non-monotonic at the reference resolution and a large region of the parameter-space has the wrong gradient (see Fig. 8.4c), the localization near the solution at previous OBL resolutions helps to safeguard the Newton update into the direction of a true solution.

8.3.2. CONVERGENCE ANALYSIS

To verify the feasibility of our approach for different initial guesses, I chose various points uniformly distributed in parameter space. The results of Newton convergence are shown in Fig. 8.5a. It is obvious that any initial guess in parameter-space will first converge to the unique solution for the coarsest representation, see Fig. 8.4a. In Fig. 8.5, the approach can converge to the true solutions for different lengths of the timestep. Note that the nonlinearity of the coarsest representation is low, and the convergence rate for this resolution is fast. With the refinement, the nonlinearity is growing, but localization helps to keep a high convergence rate. As the result, independent from the initial guess, the nonlinear solver based on continuous localization in physics remains fast and unconditionally stable.

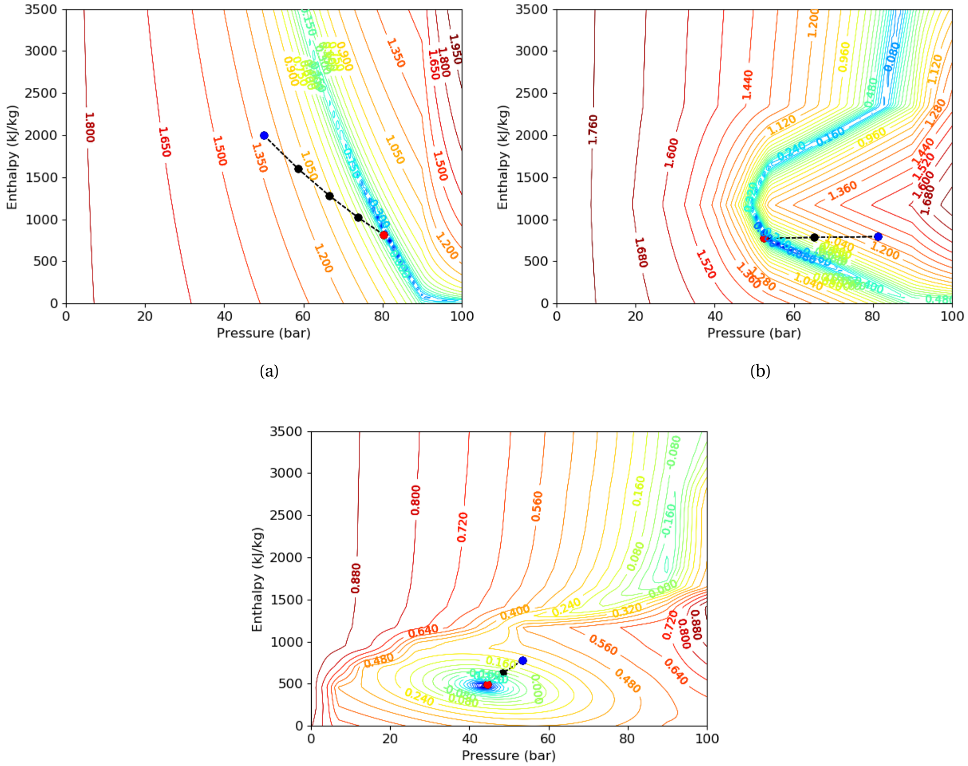

(a)

(b)

(c)

Figure 8.4: Newton path and residual contours (in l_2-norm) with continuation parameterization in physics: (a) Newton path for a coarse resolution; (b) Newton path for an intermediate resolution; (c) Newton path for fine (reference) resolution; the blue dot represents the initial guess, the black dot is the Newton update, the red dot shows the solution.

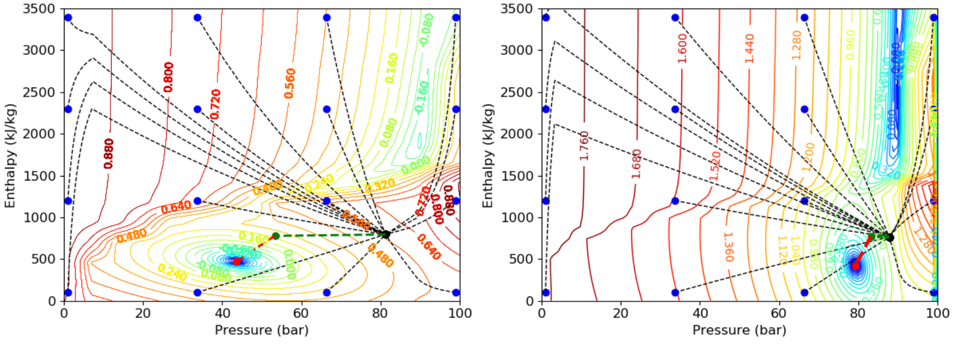

(a)

(b)

Figure 8.5: Newton path (dashed line) starting from various points in pressure-enthalpy space with (a) moderate and (b) large timestep; blue dots represent the initial guess, the black dot is the solution of coarsest resolution, the green dot is the intermediate solution and the red dot is the true solution; dashed lines in black, green and red represent the Newton path in the coarse, intermediate and fine (reference) physics resolution respectively; residual contours (in l_2-norm) are plotted for the reference physics.

8.3.3. TWO-DIMENSIONAL TEST

In this part, a one-layer model extracted from a synthetic geological model [22] is chosen for the two-dimensional test. Fig. 8.6 displays the porosity distribution of the model, which ranges from 0.1 to 0.37. The initial condition is p = 10 bars, h = 1000 kJ/kg and $s_w = 0.04$, while the injection condition is $p = 90$ bars, $h = 100$ kJ/kg and $s_w = 1.0$.

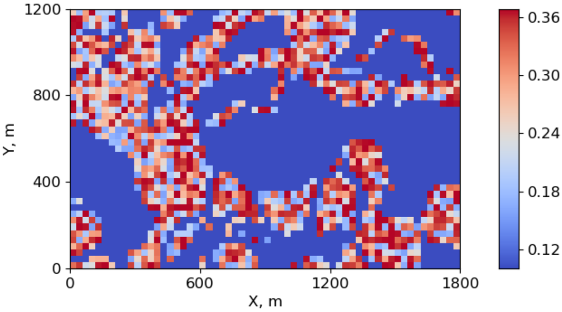

Figure 8.6: Porosity distribution of the 2D model

Fig. 8.7 displays the solutions with continuous localization in physics under a normal timestep. The maximum CFL is 15 in this case. The reference solutions with the conventional nonlinear strategy, though not shown here, are used to examine the accuracy of solutions in Fig. 8.7. The absolute differences between the two sets of solutions are displayed in Fig. 8.8, where close matches of different parameters are observed. The largest differences show up at either the heat or phase front, which can be explained by the small difference of nonlinear iterations for these two strategies.

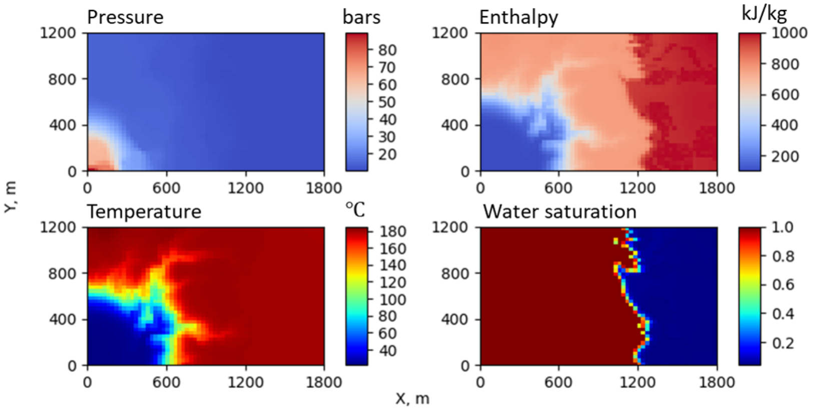

Figure 8.7: The simulation results with the strategy of continuous localization in physics under normal timestep.

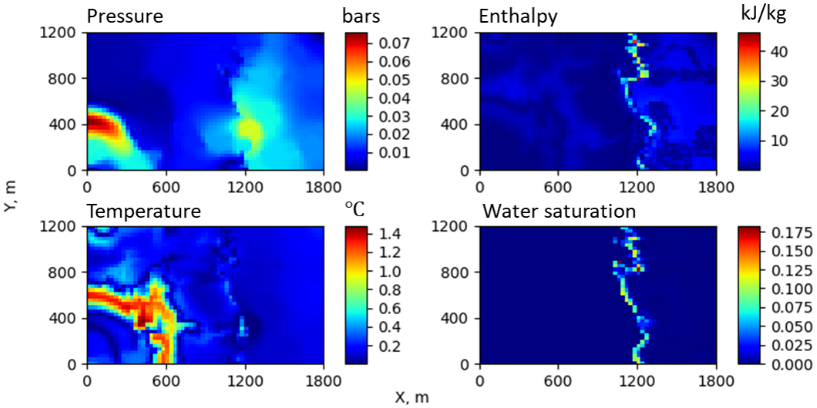

Figure 8.8: Absolute difference of solutions with conventional nonlinear strategy and continuous localization in physics for a normal timestep.

Fig. 8.9 shows the solutions of continuous localization in physics for a large timestep. The maximum CFL is 225 in this scenario. Though the conventional strategy cannot be used to simulate with a large timestep, its solutions are used to compare with Fig. 8.9. As shown in Fig. 8.10, relatively larger differences are recognized at the front of the enthalpy, temperature and saturation. Since larger numerical diffusion will be introduced with large timestep, the differences can be due to the inequality of timestep in the two compared cases.

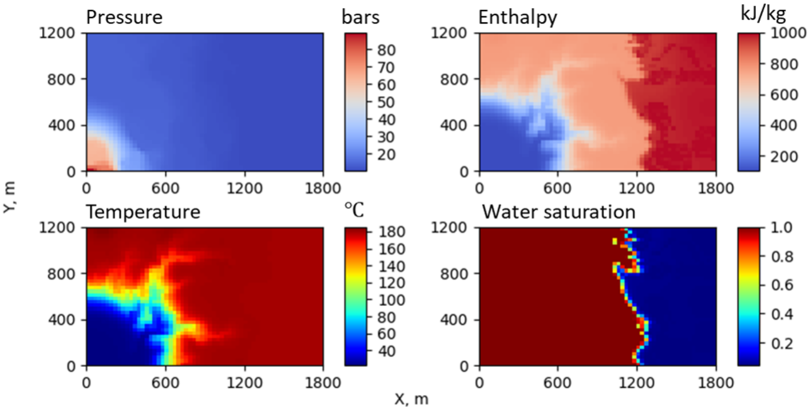

Figure 8.9: The simulation results with the strategy of continuous localization in physics for a large timestep.

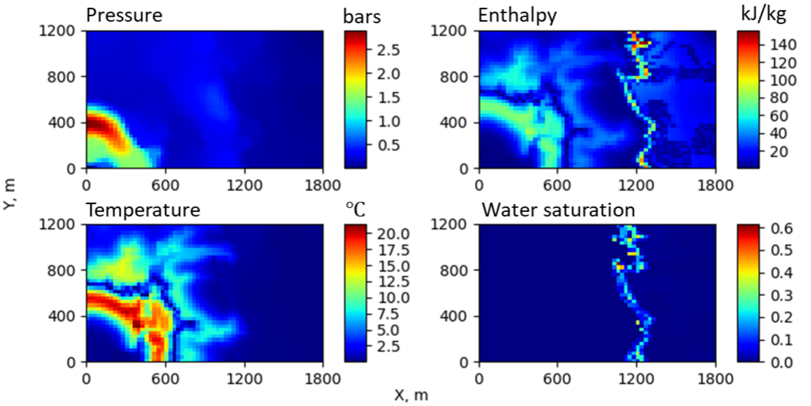

Figure 8.10: Absolute difference of solutions with conventional nonlinear strategy and continuous localization in physics for a large timestep.

8.4. CONCLUSION

Since mass and energy conservation equations are tightly coupled through the fluid thermodynamics in high-enthalpy geothermal processes, they are usually solved in a fully-implicit manner. The 'negative compressibility' phenomenon can significantly hamper the convergence of a nonlinear solver. This issue is also observed from the high-enthalpy simulation within fractured reservoirs in Chapter 7. Because of the large variation of thermodynamic properties between water and steam, the governing equations show high nonlinearity with phase transition. The problem in a single cell setup with cold water injection at fixed pressure is analyzed. The analysis of the residual map demonstrates that two different minima can be present in parameter space when the simulator is performing at sufficiently large timesteps, which brings challenges for a gradient-based nonlinear solver. A suitable initial guess is essential for the Newton-based nonlinear strategy. Applying the Operator-Based Linearization (OBL) approach,the continuous localization in physics is proposed to solve the governing equation system. With parameterization in physics changing from a coarse to fine resolution, the state-dependent operators and resulting residual are changing from almost linear and monotonic behaviour to a highly nonlinear and non-monotonic shape. In the proposed nonlinear strategy, the solution at a coarser parameterization in physics is taken as an initial guess for the solution at a finer physics resolution. This continuous localization approach makes the nonlinear convergence process more robust in the presence of ‘negative compressibility’. To verify the feasibility of this approach, I prepare a synthetic two-dimensional test case and make a comparison between the conventional and proposed approaches. The results demonstrate that the simulation of high-enthalpy geothermal applications can benefit from the continuous localization by running the model at large timesteps.

9

RECAPITULATION AND CONCLUDING REMARKS

9.1. GEOTHERMAL BENCHMARKS

Delft Advanced Research Terra Simulator (DARTS) is established within the Operator-base Linearization framework. The designed architecture of DARTS generalizes and modularizes the programming procedures, which enables efficient code development. In DARTS, a fully implicit, fully coupled numerical strategy combined with two-point flux approximation (TPFA) on general unstructured mesh is adopted for general purpose reservoir simulations. As part of this thesis, the geothermal module was newly developed within DARTS, including the implementation of a C++ kernel, a Python user interface and the integration of an external package (IAPWS-IF97) for property calculation. These developments have enabled the evaluation of heterogeneous geothermal reservoirs of unprecedented complexity with simple desktop computing equipment.

To validate both the code implementation and the suitability of the OBL approach for geothermal simulations, a set of systematic and comprehensive benchmarks have been designed and compared with state-of-the-art numerical simulators, TOUGH2 and AD-GPRS, frequently used in geothermal simulations.

Without loss of generality, single-component water is taken as the working fluid in geothermal benchmarks. Although the property of water seems simple, it will create great complexity and non-linearity for numerical simulations when liquid water and vaporized steam coexist in a system. Therefore, the accuracy of a newly developed code in dealing with highly nonlinear flow and transport should be verified.

In this thesis, several models were used and designed to do such a verification. First, the one-dimensional models are compared under high-enthalpy conditions with buoyancy. Sophisticated boundary conditions (e.g., with boiling mass and heat sources) are assigned to test the robustness of the simulators. Highly nonlinear thermal flow in the selected cases with the counterflow of cold and hot fluids usually challenges numerical reservoir simulation. DARTS achieved good matches with the other two simulators. The follow-up OBL resolution study demonstrates that a relatively coarse resolution in the physical interpolation space is able to deliver accurate results. The increase of nonlinearity with buoyancy requires more supporting points in the interpolation table, but it does not have a major effect on the computing efficiency of the OBL interpolation.

The two-dimensional benchmark tests involve a synthetic fluvial model. The capability of DARTS to simulate planar fluid and heat transport in a heterogeneous fluvial system with different boundary and initial conditions is verified by the close match with both TOUGH2 and AD-GPRS. In addition, the multi-options in well controls (e.g. constant bottom hole pressure, constant rate with constant temperature or enthalpy) integrated in DARTS were checked in these comparisons. Finally, the three-dimensional synthetic fluvial geological model comparison displays the ability of DARTS to simulate realistic geothermal fields. The performance comparison among the 3 simulators shows that DARTS allows simulation with a noticeable reduction in CPU time owing to the OBL approach. Through the investigation of Chapter 3, the accuracy and efficiency of DARTS performing geothermal simulations with the OBL approach has been verified.

9.2. GEOTHERMAL APPLICATIONS IN DARTS

For geothermal developments in reality, the uncertain and sensitive geological and operational parameters will influence the efficiency of the operations. Efficient numerical simulations are often utilized to predict the system output with specific measurements to minimize the uncertainty from a system.

In Chapter 5, a real heterogeneous geothermal reservoir within the West Netherlands Basin is used for investigation. Detailed geological measurements enable a thorough and highly resolved characterization of the reservoir. Approximately 3.2 million grid blocks are present in the model, 0.8 million for sandstone and 2.4 million for shale. The high-resolution model also guarantees the reliability and representativeness of the numerical findings. A set of comprehensive sensitivity analyses about the impact of parameters relevant for system lifetime and energy production have been performed. The striking contribution of the shale facies to heat production has been quantified and demonstrates that the shale facies must not be ignored in real geothermal applications. Heterogeneity, the ubiquitous feature of subsurface, plays a vital role not only for pressure-driven convection, but also influences temperature-driven conduction. This is proven by the large impact of well placement and overburden on system lifetime. For real geothermal projects, only pursuing longer lifetime is not the optimal choice. It is essential to also consider the energy production and economics. Through the detailed sensitivity analyses, the insights for uncertainty quantification required in geothermal development are obtained.

In Chapter 6, a full set of uncertainty quantification is performed with the same geological model. Studied parameters, covering geological, physical and economical aspects, are sampled with the Monte Carlo method. Though the model is huge for the ensembles of simulations in this part, the GPU version of DARTS greatly shortens the simulation time by its high computing performance. Finally, large uncertainties are recognized from the wide range of energy production and NPV values, which further proves the necessity to conduct uncertainty quantification before field operations.

In Chapter 7, multiphase flow in fractured high-enthalpy geothermal reservoirs is numerically investigated. A discrete-fracture model is utilized to describe the fractured system. To characterize the thermal transport processes accurately and efficiently, the resolution of discretization is optimized at the beginning. A set of comprehensive analyses is conducted to compare the convergence and computational efficiency of simulations based on a synthetic fracture model. On the basis of the converged numerical solution, a thermal Peclet number is defined to characterize the interplay between thermal convection and conduction, which are the two governing mechanisms of thermal transport in geothermal systems. Different heat transfer stages are recognized on the Peclet curve in conjunction with production regimes of the synthetic fractured reservoir. A fracture network, sketched and scaled up from a digital map of a realistic outcrop, is then utilized to perform a sensitivity analysis of the key parameters influencing the heat and mass transfer. Thermal propagation and Peclet number are found to be sensitive to flow rate and thermal parameters (e.g., rock heat conductivity and heat capacity). This chapter provides the necessary procedures for practical investigations regarding geothermal developments with uncertainties.

Chapter 8 describes the ‘negative compressibility’ issue in thermal transfer with the presence of saturated steam. Due to the large contrast in thermodynamic properties of water and steam, the convergence of nonlinear solutions is severely affected, which often restricts the simulation to small timesteps. The performance comparison of single- and two-phase simulations in fractured reservoirs (Chapter 7) provides an illustrative example of this issue. A novel strategy for the nonlinear solution is proposed within the OBL framework, which enables the hierarchical parameterization of physical space on different levels. The nonlinear iteration starts with a coarse representation of physics and localizes the updated nonlinear solution to the vicinity of the full-physics solution, which is then approached with the gradual refinement of physical space. The nonlinear convergence is improved with initially reduced nonlinearity in physics under coarse representation and therefore, a large timestep can be used in the simulation.

In this thesis, a geothermal module has been developed in DARTS. The capability and performance of the new codes support unprecedented simulation efficiency for complex heterogeneous reservoirs at geological scales. That way, the impact of reservoir heterogeneity on geothermal developments can be unveiled and quantified through systematic sensitivity analyses and uncertainty quantifications inside a real geothermal reservoir. With the implemented codes, researchers and engineers can use DARTS to simulate complex geothermal applications in great detail efficiently and accurately.

REFERENCES

[1] J. W. Lund and T. L. Boyd, *Direct utilization of geothermal energy 2015 worldwide review,* Geothermics **60**, 66 (2016).

[2] P. J. Vardon, D. F. Bruhn, A. Steiginga, B. Cox, H. Abels, A. Barnhoorn, G. Drijkoningen, E. Slob, and K. Wapenaar, *A geothermal well doublet for research and heat supply of the TU Delft campus,* arXiv preprint (2020).

[3] R. Bertani, *Geothermal power generation in the world 2010-2014 update report,* Geothermics **60**, 31 (2016).

[4] D. D. Blackwell, P. T. Negraru, and M. C. Richards, *Assessment of the enhanced geothermal system resource base of the United States,* Natural Resources Research **15**, 283 (2006).

[5] O. Ellabban, H. Abu-Rub, and F. Blaabjerg, *Renewable energy resources: Current status, future prospects and their enabling technology,* Renewable and Sustainable Energy Reviews **39**, 748 (2014).

[6] L. Kramers, J. D. Van Wees, M. P. D. Pluymaekers, A. Kronimus, and T. Boxem, *Direct heat resource assessment and subsurface information systems for geothermal aquifers; the Dutch perspective,* Netherlands Journal of Geosciences **91**, 637 (2012).

[7] J. Limberger, T. Boxem, M. Pluymaekers, D. Bruhn, A. Manzella, P. Calcagno, F. Beekman, S. Cloetingh, and J. D. van Wees, *Geothermal energy in deep aquifers: A global assessment of the resource base for direct heat utilization,* Renewable and Sustainable Energy Reviews **82**, 961 (2018).

[8] V. Stefansson, *World geothermal assessment,* in *World Geothermal Congress* (2005).

[9] W. L. Cheng, T. T. Li, Y. L. Nian, and K. Xie, *Evaluation of working fluids for geothermal power generation from abandoned oil wells,* Applied Energy **118**, 238 (2014).

[10] G. Cui, L. Zhang, B. Ren, C. Enechukwu, Y. Liu, and S. Ren, *Geothermal exploitation from depleted high temperature gas reservoirs via recycling supercritical CO_2: Heat mining rate and salt precipitation effects,* Applied Energy **183**, 837 (2016).

[11] A. P. Davis and E. E. Michaelides, *Geothermal power production from abandoned oil wells,* Energy **34**, 866 (2009).

[12] Z. Ziabakhsh-Ganji, H. M. Nick, M. E. Donselaar, and D. F. Bruhn, *Synergy potential for oil and geothermal energy exploitation,* Applied Energy **212**, 1433 (2018).

[13] F. Dalla Longa, L. P. Nogueira, J. Limberger, J. D. V. Wees, and B. van der Zwaan, *Scenarios for geothermal energy deployment in Europe,* Energy **206**, (2020).

[14] M. P. Simpson and G. Bignall, *Undeveloped high-enthalpy geothermal fields of the Taupo Volcanic Zone, New Zealand,* Geothermics **59**, 325 (2016).

[15] D. Aravena, M. Muñoz, D. Morata, A. Lahsen, M. T. Parada, and P. Dobson, *Assessment of high enthalpy geothermal resources and promising areas of Chile,* Geothermics **59**, 1 (2016).

[16] H. Kivanc Ates and U. Serpen, *Power plant selection for medium to high enthalpy geothermal resources of Turkey,* Energy **102**, 287 (2016).

[17] T. Geysers, *The Geysers.* (2019).

[18] J. B. Randolph and M. O. Saar, *Combining geothermal energy capture with geologic carbon dioxide sequestration,* Geophysical Research Letters **38**, (2018).

[19] C. J. L. Willems, H. M. Nick, G. J. Weltje, and D. F. Bruhn, *An evaluation of interferences in heat production from low enthalpy geothermal doublets systems,* Energy **135**, 500 (2017).

[20] P. Hein, O. Kolditz, U. J. Görke, A. Bucher, and H. Shao, *A numerical study on the sustainability and efficiency of borehole heat exchanger coupled ground source heat pump systems,* Applied Thermal Engineering **100**, 421 (2016).

[21] M. Brehme, S. Regenspurg, P. Leary, F. Bulut, H. Milsch, S. Petrauskas, R. Valickas, and G. Blocher, *Injection-triggered occlusion of flow pathways in geothermal operations,* Geofluids , (2018).

[22] S. Shetty, D. Voskov, and D. F. Bruhn, *Numerical strategy for uncertainty quantification in low enthalpy geothermal projects,* in *Workshop on Geothermal Reservoir Engineering* (2018).

[23] C. R. Faust and J. W. Mercer, *Geothermal reservoir simulation: 1. Mathematical models for liquid- and vapor-dominated hydrothermal systems,* Water Resources Research **15**, 23 (1979).

[24] M. J. O'Sullivan, *Geothermal reservoir simulation,* International Journal of Energy Research **9**, 319 (1985).

[25] M. Karimi-Fard and L. J. Durlofsky, *A general gridding, discretization, and coarsening methodology for modeling flow in porous formations with discrete geological features,* Advances in Water Resources **96**, 354 (2016).

[26] M. J. O'Sullivan, K. Pruess, and M. J. Lippmann, *State of the art geothermal reservoir simulation,* Geothermics **30**, 395 (2001).

[27] K. Pruess, C. M. Oldenburg, and G. J. Moridis, *TOUGH2 USER'S GUIDE,* Tech. Rep. (1999).

[28] J. O'Sullivan, D. Dempsey, A. Croucher, A. Yeh, and M. O'Sullivan, *Controlling complex geothermal simulations using PYTOUGH,* (2013).

[29] J. O'Sullivan, S. Arthur, and M. O'Sullivan, *A new reservoir model to support environmental monitoring of the Orakeikorako geothermal system,* Geothermics **59**, 90 (2016).

[30] A. Battistelli, C. Calore, and K. Pruess, *The simulator TOUGH2/EWASG for modelling geothermal reservoirs with brines and non-condensible gas,* Geothermics **26**, 437 (1997).

[31] A. E. Croucher and M. J. O'Sullivan, *Application of the computer code TOUGH2 to the simulation of supercritical conditions in geothermal systems,* Geothermics **37**, 622 (2008).

[32] K. Pruess, *Numerical simulation of multiphase tracer transport in fractured geothermal reservoirs,* Geothermics **31**, 475 (2002).

[33] H. J. Kretzschmar and W. Wagner, *International Steam Tables: Properties of Water and Steam based on the Industrial Formulation IAPWS-IF97* (Springer Science & Business Media, 2007).

[34] T. T. Garipov, P. Tomin, R. Rin, D. V. Voskov, and H. A. Tchelepi, *Unified thermo-compositional-mechanical framework for reservoir simulation,* Computational Geosciences **22**, 1039 (2018).

[35] D. Voskov and Y. Zhou, *AD-GPRS, Stanford University's Automatic Differentiation based General Purpose Research Simulator user's manual*, Tech. Rep. (2015).

[36] Z. Y. Wong, R. Horne, and D. Voskov, *A geothermal reservoir simulator in AD-GPRS,* in *World Geothermal Congress* (2015).

[37] C. R. Faust and J. W. Mercer, *Geothermal reservoir simulation: 2. Numerical solution techniques for liquid- and vapor-dominated hydrothermal systems,* Water Resources Research **15**, 31 (1979).

[38] Z. Y. Wong, R. N. Horne, and H. A. Tchelepi, *Sequential implicit nonlinear solver for geothermal simulation,* Journal of Computational Physics **368**, 236 (2018).

[39] DARTS, *Delft Advanced Research Terra Simulator.* (2019).

[40] M. Khait and D. V. Voskov, *Integrated framework for modelling of thermal-compositional multiphase flow in porous media,* in *SPE Reservoir Simulation Conference* (2019).

[41] M. Khait and D. V. Voskov, *Operator-based linearization for efficient modeling of geothermal processes,* Geothermics **74**, 7 (2018).

[42] D. V. Voskov, *Operator-based linearization approach for modeling of multiphase multi-component flow in porous media,* Journal of Computational Physics **337**, 275 (2017).

[43] M. Khait and D. V. Voskov, *Adaptive parameterization for solving of thermal/compositional nonlinear flow and transport with buoyancy,* SPE Journal **23**, 522 (2018).

[44] M. Khait and D. V. Voskov, *GPU-offloaded general purpose simulator for multiphase flow in porous media,* in *SPE Reservoir Simulation Conference* (2017).

[45] M. Khait, D. V. Voskov, and R. Zaydullin, *High performance framework for modelling of complex subsurface flow and transport applications,* in *17th European Conference on the Mathematics of Oil Recovery* (2020).

[46] Y. Wang, D. V. Voskov, M. Khait, and D. F. Bruhn, *An efficient numerical simulator for geothermal simulation: A benchmark study,* Applied Energy **264**, (2020).

[47] M. Khait, *Delft Advanced Research Terra Simulator: General Purpose Reservoir Simulator with Operator-Based Linearization*, Ph.D. thesis (2019).

[48] M. Khait and D. V. Voskov, *Operator-based linearization for general purpose reservoir simulation,* Journal of Petroleum Science and Engineering **157**, 990 (2017).

[49] M. Khait and D. Voskov, *Operator-based linearization for efficient modeling of geothermal processes,* Geothermics **74**, 7 (2018).

[50] K. Kala and D. V. Voskov, *Element balance formulation in reactive compositional flow and transport with parameterization technique,* Computational Geosciences **24**, 609 (2020).

[51] Q. Boersma, N. Hardebol, M. Houben, A. Barnhoorn, and M. Drury, *Fracture-fault network characterization of pavement imagery of the Whitby Mudstone, Yorkshire,* (2015).

[52] M. Karimi-Fard, L. J. Durlofsky, and K. Aziz, *An efficient discrete-fracture model applicable for general-purpose reservoir simulators,* SPE Journal **9**, 227 (2004).

[53] Y. Wang, S. de Hoop, D. v. Voskov, D. F. Bruhn, and G. Bertotti, *Modeling of high-enthalpy geothermal projects in fractured reservoirs,* in *World Geothermal Congress* (2020).

[54] D. Perkins, *Reservoir simulation for play-based development of low enthalpy geothermal resources.*, Master's thesis, TU Delft (2019).

[55] M. Karimi-Fard and L. J. Durlofsky, *Accurate resolution of near-well effects in upscaled models using flow-based unstructured local grid refinement,* SPE Journal **17**, 1084 (2012).

[56] C. J. L. Willems and H. M. Nick, *Towards optimisation of geothermal heat recovery: An example from the West Netherlands Basin,* Applied Energy **247**, 582 (2019).

[57] R. A. Crooijmans, C. J. L. Willems, H. M. Nick, and D. F. Bruhn, *The influence of facies heterogeneity on the doublet performance in low-enthalpy geothermal sedimentary reservoirs,* Geothermics **64**, 209 (2016).

[58] R. Shukla, P. Ranjith, A. Haque, and X. Choi, *A review of studies on CO_2 sequestration and caprock integrity,* Fuel **89**, 2651 (2010).

[59] S. E. Poulsen, N. Balling, and S. B. Nielsen, *A parametric study of the thermal recharge of low enthalpy geothermal reservoirs,* Geothermics **53**, 464 (2015).

[60] S. C. M. Krevor, R. Pini, B. Li, and S. M. Benson, *Capillary heterogeneity trapping of CO_2 in a sandstone rock at reservoir conditions,* Geophysical Research Letters **38**, (2011).

[61] C. T. Miller, G. Christakos, P. T. Imhoff, J. F. McBride, J. A. Pedit, and J. A. Trangenstein, *Multiphase flow and transport modeling in heterogeneous porous media: Challenges and approaches,* Advances in Water Resources **21**, 77 (1998).

[62] R. Pini, S. C. M. Krevor, and S. M. Benson, *Capillary pressure and heterogeneity for the CO_2/water system in sandstone rocks at reservoir conditions,* Advances in Water Resources **38**, 48 (2012).

[63] P. Asai, P. Panja, J. McLennan, and M. Deo, *Effect of different flow schemes on heat recovery from Enhanced Geothermal Systems (EGS),* Energy **175**, 667 (2019).

[64] S. Saeid, R. Al-Khoury, H. M. Nick, and M. A. Hicks, *A prototype design model for deep low-enthalpy hydrothermal systems,* Renewable Energy **77**, 408 (2015).

[65] C. J. L. Willems, T. Goense, H. M. Nick, and D. F. Bruhn, *The relation between well spacing and Net Present Value in fluvial hot sedimentary aquifer geothermal doublets; a West Netherlands Basin case study,* in *Workshop on Geothermal Reservoir Engineering* (2016).

[66] C. J. I. Wiggers, *The Delft Sandstone in the West Netherlands Basin.*, Master's thesis, TU Delft (2019).

[67] A. Daniilidis, B. Alpsoy, and R. Herber, *Impact of technical and economic uncertainties on the economic performance of a deep geothermal heat system,* Renewable Energy **114**, 805 (2017).

[68] A. Daniilidis, M. Khait, S. Saeid, D. F. Bruhn, and D. V. Voskov, *A high-performance framework for the optimization of geothermal systems, comparing energy production and economic output,* in *World Geothermal Congress* (2020).

[69] A. Daniilidis, H. M. Nick, and D. F. Bruhn, *Interdependencies between physical, design and operational parameters for direct use geothermal heat in faulted hydrothermal reservoirs,* Geothermics **86**, (2020).

[70] TNO, *Advies aanvraag Garantieregeling AARD04003 Geothermie Bergschenhoek (TNO project AGE 15-10.006),* Tech. Rep. (2015).

[71] Y. Wang, M. Khait, A. Daniilidis, D. V. Voskov, S. Saeid, and D. F. Bruhn, *Uncertainty quantification of realistic geothermal reservoir,* in *World Geothermal Congress* (2020).

[72] C. Scheidt and J. Caers, *Uncertainty quantification in reservoir performance using distances and kernel methods-application to a West Africa deepwater turbidite reservoir,* SPE Journal **14**, 680 (2009).

[73] F. Ballio and A. Guadagnini, *Convergence assessment of numerical Monte Carlo simulations in groundwater hydrology,* Water Resources Research **40**, W046031 (2004).

[74] Z. Dai, H. Viswanathan, J. Fessenden-Rahn, R. Middleton, F. Pan, W. Jia, S.-Y. Lee, B. Mcpherson, W. Ampomah, and R. Grigg, *Uncertainty quantification for CO_2 sequestration and enhanced oil recovery,* Energy Procedia **63**, 7685 (2014).

[75] A. James and C. Oldenburg, *Linear and Monte Carlo uncertainty analysis for subsurface contaminant transport simulation,* Water Resources Research **33**, 2495 (1997).

[76] M. Cremon, M. Christie, and M. Gerritsen, *Monte Carlo simulation for uncertainty quantification in reservoir simulation: A convergence study,* Journal of Petroleum Science and Engineering **190**, (2020).

[77] N. Athens and J. Caers, *A Monte Carlo-based framework for assessing the value of information and development risk in geothermal exploration,* Applied Energy **256**, (2019).

[78] S. Taverniers and D. Tartakovsky, *Estimation of distributions via multilevel Monte Carlo with stratified sampling,* Journal of Computational Physics **419**, (2020).

[79] Y. Chen, L. Durlofsky, M. Gerritsen, and X. Wen, *A coupled local-global upscaling approach for simulating flow in highly heterogeneous formations,* Advances in Water Resources **26**, 1041 (2003).

[80] B. Gong, M. Karimi-Fard, and L. Durlofsky, *Upscaling discrete fracture characterizations to dual-porosity, dual-permeability models for efficient simulations of flow with strong gravitational effects,* SPE Journal **13**, 58 (2008).

[81] A. Daniilidis, B. Alpsoy, and R. Herber, *Impact of technical and economic uncertainties on the economic performance of a deep geothermal heat system,* Renewable Energy **114**, 805 (2017).

[82] S. Saeid, Y. Wang, D. A., M. Khait, D. V. Voskov, and D. F. Bruhn, *Lifetime and energy prediction of geothermal systems: Uncertainty analysis in highly heterogeneous geothermal reservoirs (Netherlands),* in *World Geothermal Congress* (2020).

[83] M. Batzle and Z. Wang, *Seismic properties of pore fluids,* Geophysics **57**, 1396 (1992).

[84] M. Kang and R. Jackson, *Salinity of deep groundwater in California: Water quantity, quality, and protection,* Proceedings of the National Academy of Sciences of the United States of America **113**, 7768 (2016).

[85] A. Borgia, K. Pruess, T. Kneafsey, C. Oldenburg, and L. Pan, *Numerical simulation of salt precipitation in the fractures of a* CO_2*-enhanced geothermal system,* Geothermics **44**, 13 (2012).

[86] S. Saeid, R. Al-Khoury, H. Nick, and M. Hicks, *A prototype design model for deep low-enthalpy hydrothermal systems,* Renewable Energy **77**, 408 (2015).

[87] Y. Wang, D. V. Voskov, M. Khait, S. Saeid, and D. F. Bruhn, *Influential factors to the development of low-enthalpy geothermal energy: a sensitivity study of realistic field,* submitted (2020).

[88] K. Midttømme and E. Roaldset, *Thermal conductivity of sedimentary rocks: uncertainties in measurement and modelling,* Geological Society Special Publication **158**, 45 (1999).

[89] M. Labus and K. Labus, *Thermal conductivity and diffusivity of fine-grained sedimentary rocks,* Journal of Thermal Analysis and Calorimetry **132**, 1669 (2018).

[90] M. Aliyu and H.-P. Chen, *Sensitivity analysis of deep geothermal reservoir: Effect of reservoir parameters on production temperature,* Energy **129**, 101 (2017).

[91] S. M. Benson, J. S. Daggett, E. Iglesias, V. Arellano, and J. Ortiz-Ramirez, *Analysis of thermally induced permeability enhancement in geothermal injection wells,* in *Workshop on Geothermal Reservoir Engineering* (1987).

[92] D. W. Peaceman, *Interpretation of well-block pressures in numerical reservoir simulation with nonsquare grid blocks and anisotropic permeability.* SPE Journal **23**, 531 (1983).

[93] I. Berre, F. Doster, and E. Keilegavlen, *Flow in fractured porous media: A review of conceptual models and discretization approaches,* Transport in Porous Media **130**, 215 (2019).

[94] J. E. Warren and P. J. Root, *The behavior of naturally fractured reservoirs,* SPE Journal **3**, 245 (1963).

[95] H. H. Gerke and M. T. van Genuchten, *A dual-porosity model for simulating the preferential movement of water and solutes in structured porous media,* Water Resources Research **29**, 305 (1993).

[96] H. H. Gerke and M. T. van Genuchten, *Evaluation of a first-order water transfer term for variably saturated dual-porosity flow models,* Water Resources Research **29**, 1225 (1993).

[97] J. Jiang and R. M. Younis, *A multimechanistic multicontinuum model for simulating shale gas reservoir with complex fractured system,* Fuel **161**, 333 (2015).

[98] S. H. Lee, C. L. Jensen, and M. F. Lough, *Efficient finite-difference model for flow in a reservoir with multiple length-scale fractures,* SPE Journal **5**, 268 (2000).

[99] H. Hajibeygi, D. Karvounis, and P. Jenny, *A hierarchical fracture model for the iterative multiscale finite volume method,* Journal of Computational Physics **230**, 8729 (2011).

[100] L. Li and D. V. Voskov, *Multi-level discrete fracture model for carbonate reservoirs,* in *16th European Conference on the Mathematics of Oil Recovery, ECMOR 2018* (2018).

[101] T. Awadalla and D. V. Voskov, *Modeling of gas flow in confined formations at different scales,* Fuel **234**, 1354 (2018).

[102] B. Berkowitz, *Characterizing flow and transport in fractured geological media: A review,* Advances in Water Resources **25**, 861 (2002).

[103] K. Pruess and T. N. Narasimhan, *A practical method for modeling fluid and heat flow in fractured porous media,* SPE Journal **25**, 14 (1985).

[104] Y. S. Wu and K. Pruess, *A multiple-porosity method for simulation of naturally fractured petroleum reservoirs,* SPE Reservoir Eng **3**, 327 (1988).

[105] Y. Wang, M. Khait, D. V. Voskov, S. Saeid, and D. F. Bruhn, *Benchmark test and sensitivity analysis for geothermal applications in the Netherlands,* in *Workshop on Geothermal Reservoir Engineering* (2019).

[106] Y. Wang and D. Voskov, *High-enthalpy geothermal simulation with continuous localization in physics,* in *Workshop on Geothermal Reservoir Engineering* (2019).

[107] K. H. Coats, W. D. George, B. E. Marcum, and C. Chu, *Three-dimensional stimulation of steamflooding.* Soc Pet Eng AIME J **14**, 573 (1974).

[108] K. H. Coats, *Reservoir simulation: a general model formulation and associated physical/numerical sources of instability,* Boundary and Interior Layers-Computational and Asymptotic Methods (1980).

[109] K. Pruess, C. Calore, R. Celati, and Y. S. Wu, *An analytical solution for heat transfer at a boiling front moving through a porous medium,* International Journal of Heat and Mass Transfer **30**, 2595 (1987).

[110] Y. Wang, *A stability criterion for the negative compressibility problem in geothermal simulation and discrete modeling of failure in oil shale pyrolysis process.*, Master's thesis, Stanford University (2015).

[111] Z. Y. Wong, R. Rin, H. Tchelepi, and R. Horne, *Comparison of fully implicit and sequential implicit formulation for geothermal reservoir simulations,* in *Workshop on Geothermal Reservoir Engineering* (2017).

CURRICULUM VITÆ

Yang WANG

24-07-1990	Born in Shandong, China.

EDUCATION

2009–2013	Bachelor Degree, Petroleum Engineering China University of Petroleum (East China)
2013–2016	Master Degree, Petroleum Engineering China University of Petroleum (Beijing)
2016–2020	Doctor of Philosophy, Geothermal Engineering Delft University of Technology

Thesis:	The Impact of Heterogeneity on Geothermal Production: Simulation Benchmarks and Applications
Promotors:	dr. D. V. Voskov Prof. dr. D. F. Bruhn

LIST OF PUBLICATIONS

Journal Articles

4. **Y. Wang, D.V. Voskov, A. Daniilidis, M. Khait, S. Saeid, D. Bruhn**, *Uncertainty Quantification in a Realistic Low-enthalpy Geothermal Reservoir,* in preparation.
3. **Y. Wang, S. de Hoop, D.V. Voskov, D. Bruhn, G. Bertonni**, *Multiphase Mass and Heat Transfer in Fractured High-enthalpy Geothermal Systems,* submitted to a journal.
2. **Y. Wang, D.V. Voskov, M. Khait, S. Saeid, D. Bruhn**, *Influential Factors to the Development of Low-enthlapy Geothermal Energy: A Sensitivity Study of Realistic Field,* submitted to a journal.
1. **Y. Wang, D.V. Voskov, M. Khait, D. Bruhn**, *An Efficient Numerical Simulator for Geothermal Simulation: A Benchmark Study,* Applied Energy **264**, (2020).

Conference Proceedings

5. **Y. Wang, D.V. Voskov, A. Daniilidis, M. Khait, S. Saeid, D. Bruhn**, *Uncertainty Quantification in a Realistic Low-enthalpy Geothermal Reservoir,* 1st Geoscience & Engineering in Energy Transition Conference, (2020).
4. **Y. Wang, S. de Hoop, D.V. Voskov, D. Bruhn, G. Bertotti**, *Modeling of High-Enthalpy Geothermal Projects in Fractured Reservoirs,* World Geothermal Congress, (2020).
3. **S. Saeid, Y. Wang, A. Daniilidis, M. Khait, D.V. Voskov, D. Bruhn**, *Lifetime and Energy Prediction of Geothermal Systems: Uncertainty Analysis in Highly Heterogeneous Geothermal Reservoirs (Netherlands),* World Geothermal Congress, (2020).
2. **Y. Wang, D.V. Voskov**, *High-Enthalpy Geothermal Simulation with Continuous Localization in Physics,* Workshop on Geothermal Reservoir Engineering, (2019).
1. **Y. Wang, M. Khait, D.V. Voskov, S. Saeid, D. Bruhn**, *Benchmark Test and Sensitivity Analysis for Geothermal Applications in the Netherlands,* Workshop on Geothermal Reservoir Engineering, (2019).

ACKNOWLEDGEMENTS

Here I would like to say thank you to all who made my PhD study memorable and rich. I will never complete my PhD without all of your help.

First and foremost, I would like to thank my promotor and daily supervisor, Dr. Denis Voskov. Dear Denis, it is my honor to work under your guidance. No words can express my deepest gratitude for your endless help. Though busy with the daily work, you always managed to stop by our PhD office and listened to my progresses carefully. You were always patient to answer my questions and helped me out of the difficulties. Your comments and suggestions saved me a lot of time and sped up my research greatly. I could not imagine more from a supervisor to be so patient and devoted into my research. Thank you for encouraging me to attend the conferences. I will always remember our trip to Stanford and you showed me around the amazing campus. Thank you and Kate for warmly hosting the wonderful group parties. I enjoyed the moment when you played the guitar. In the past years, what I learnt is not only the knowledge about the major, but also the way of getting along with people and necessities about future life. Thank you, Denis.

I would like to express special gratitude to my promotor, Prof. David Bruhn. Dear David, thank you for offering me the chance doing my PhD. I feel very lucky and happy to work with you. You could patiently answer my questions and provide kind suggestions for my shortcomings. You always proposed critical and constructive comments for my papers, which were definitely improved pretty much. Thank you for encouraging and supporting me to attend the conferences and the field trip. I am grateful for your efforts and encouragement.

I would like to thank Dr. Phil Vardon, Dr. John O'Sullivan, Dr. Maren Brehme, Prof. Inga Berre, Prof. Pacelli Zitha and Prof. Bill Rossen for being my committee members and providing valuable comments for this dissertation. Phil, thank you for organizing the weekly geothermal meeting, which gave me the chance to know updated news and interesting research topics related to geothermal. Thank you also for providing me a short-term postdoc position. John, thank you for helping me set up the benchmark cases in TOUGH2 and provided valuable advice for the high-enthalpy simulations.

Mark, my dear friend behaving also as my 'supervisor', thank you for your essential contributions to my work. You always patiently and logically answered my puzzles and questions about C++ programming and DARTS. This really means a lot for me. I was often surprised and overwhelmed by your rigorousness and proficiency in programming, which redefined professionalism in my mind.

Jiakun, thank you for the so many enlightening chats and kind suggestions during these 4 years. You, as a big brother, always listened to my words and shared your thoughts. You could always provide the honest and practical advice when I met obstacles and difficulties. I really appreciate them. Thank you and Xiaoyan for organizing the delicious meals. The academic achievements of you both built good examples for me to follow.

I would like to thank my geothermal fellows, Alex, Baptiste, Sanaz and Anne. Alex, thank you for the many constructive talks and helps for my work. Thank you also for the interest in using DARTS for geothermal simulations. Baptiste, thank you for the suggestions on online courses and about writing. I admire your awesome research which integrates field work, experiments and numerical simulations together. I cherished the memory of our field trip with you both and Anne to Italy. After one day's field work, we always managed to get a relax and enjoy the sunset near the beach with a beer. Sanaz, thank you for preparing the geological model for this work and I appreciate your constructive comments and corrections about my writing.

Special thanks goes to the DARTS group members, Xiaocong, Stephan, Kiarash, Xiaoming and Aleks. Thank you for providing the many technical helps and suggestions in these few years. All of your spirits and efforts in achieving higher research goals inspire me moving forward.

Longlong, thank you for the many enlightening conversations, which really stimulated my interests in reservoir simulations at the very beginning of my PhD and sharpened my understandings later. Thanks goes to my PhD fellows, Jinyu, Durgesh, Matei, Nikita, Martijn, Swej, Kai, Guanqun, Martha, Fanxiang, Siamak and Moshen. Thank you for helping me make it through.

I would like to express my gratitude to the wonderful support staffs of Geoscience Engineering. Thank you, Marlijn, Lydia, Ralf, Margot, Marja and Nancy, for your continuous help and support with my requests.

I would like to thank my aunt for your constant support, especially during my PhD application. Last but not the least, I would like to express my deepest gratitude to my beloved parents. No words can really describe my appreciation for your unconditional love. You sacrificed a lot to support my PhD journey, during which we experienced joys and sorrows. Love you, mom and dad!